

THESIS FOR THE DEGREE OF LICENTIATE OF ENGINEERING

**Steady state analysis of HVDC grid in the North Sea with
offshore wind power plants**

Kalid Yunus



Department of Energy and Environment
Division of Electric Power Engineering
CHALMERS UNIVERSITY OF TECHNOLOGY
Göteborg, Sweden 2014

Steady state analysis of HVDC grid in the North Sea with offshore wind power plants

KALID YUNUS

©KALID YUNUS, 2014

Licentiate Thesis at the Chalmers University of Technology

Department of Energy and Environment
Division of Electric Power Engineering
SE-412 96 Göteborg
Sweden
Telephone +46(0)31-772 1000

Chalmers Bibliotek, Reproservice
Göteborg, Sweden 2014

Alhamdulillah!

Steady state analysis of HVDC grid in the North Sea with offshore wind power plants
KALID YUNUS
Department of Energy and Environment
Chalmers University of Technology

Abstract

In this thesis, some of economical and technical aspects of expanding the HVDC (High Voltage Direct Current) transmission systems in the North Sea are studied at steady state. In the thesis, it is assumed that the expansion of the system is made by connecting WPPs (Wind Power Plants) to the system which is built for power exchange. From the economical point view, it is observed that the system operator can gain from the expansion of the system. The gain can vary depending upon the total capacity of the WPPs, the transmission tariff paid by the WPP (Wind Power Plant) operators and the cost of altering the scheduled exchange powers due to the added WPPs. It is also observed that, in most of the studied cases, significant economic gains can be achieved by reinforcing the systems when the total WPP capacities are higher than 60 % of the total possible WPP capacities from a control point of view.

Furthermore, in order to simulate the power from the WPPs in the system, which is a function of wind speed, a standard ARIMA (Auto Regressive Integrated Moving Average) based modelling procedure is used. Due to a limitation in the standard modelling procedure to model a time series wind speed data, a modified modelling procedure is proposed which is based on decomposing the data into HF (High Frequency) and LF (Low Frequency) components. In addition, for a 10 minute average wind speed data, a six order AR (Auto Regressive) model structure can be used to model the HF component of the data and a six order MA (Moving Average) model structure can be used to model the LF component of the data. In order to split the 10 minute average wind speed data into HF and LF components, a cut off period of $T_{cutoff} = 4day$ was found to be sufficient. Moreover, proposed model structures and the corresponding model parameters that can be used to simulate 10 minute average wind speed data in the Baltic Sea areas, where there are no measured wind speed data, are also presented in the thesis.

In addition, a control strategy which is based on local primary controllers followed by a central secondary controller is proposed in the thesis. The proposed control strategy can be used to enable the integration of WPPs into a system designed for power exchange.

Index Terms: meshed HVDC transmission grid, VSC HVDC, external AC grid/connection, WPP, scheduled exchange power, transmission fee/tariff, primary controller, secondary/supervisory controller, ARIMA, NPV.

Acknowledgements

This work was carried out at Chalmers University of Technology, Department of Energy and Environment, Electric Power Engineering Division. The financial support, provided by the Swedish Energy Agency (Energimyndigheten), is gratefully appreciated. Furthermore, my special thanks go to my main supervisor Prof. Torbjörn Thiringer for his support, critical comments regarding this study and revising the thesis manuscript extensively to give it a better shape. I would also like to thank my examiner Prof. Ola Carlson and Dr. Tarik Abdulahovic for their constructive ideas and support during the follow up meetings and for revising the thesis manuscript. In addition, I would like to greatly appreciate the support from Dr. Peiyuan Chen during wind speed modelling of the thesis work.

I would also like thank my friends and colleagues at Elteknik for their support and for making a comfortable working environment. My special thanks go to my room mates Gustavo Pinares and Yasir Arafat and the 'Lunch Team' for the nice times and discussion we had and I hope that will continue.

Finally, I would like to express my at most gratitude for my wife Destu Abdulkadir and my baby boy Omar Yunus for their patience and for the love and support you gave me during this time. I love you both!

*Kalid Yunus,
Göteborg,
November, 2014*

List of Abbreviations

ACC	Auto Correlation Coefficient
AR	Auto Regressive
ARIMA	Auto Regressive Integrated Moving Average
ARIMA(p,d,q)	ARIMA model of order p, d and q
CCC	Cross Correlation Coefficient
CCU	Central Control Unit
CDF	Cumulative Distribution Function
CIGRE	International Council on Large Electric Systems
CSC	Current Source Converter
DE	Germany (Used as a bus index located in a area in Germany)
DK	Denmark (Used as a bus index located in a area in Denmark)
ENTSO-E	European Network of Transmission System Operators for Electricity
EWEA	European Wind Energy Association
GHG	Green House Gas
HVDC	High Voltage Direct Current
HF	High Frequency
LARIMA	Limited Auto Regressive Integrated Moving Average
LCU	Local Control Unit
LF	Low Frequency
MA	Moving Average
MTHVDC	Multi-Terminal High Voltage Direct Current
M€	Million Euro
NL	Netherlands (Used as a bus index located in a area in the Netherlands)
NO	Norway (Used as a bus index located in a area in Norway)
NPV	Net Present Value
NR	Newton-Raphson
NSCOGI	North Seas Countries Offshore Grid Initiative
PAC	Partial Auto Correlation Coefficient
PCC	Point of Common Coupling
PDF	Probability Density Function
PSD	Power Spectral Density
Q-Q	Quantile-Quantile

List of Abbreviations

TSO	Transmission System Operator
UK	United Kingdom (Used as a bus index located in a area in United Kingdom)
VARIMA	Vector Auto Regressive Integrated Moving Average
VSC	Voltage Source Converter
WF x	Wind Farm x, an index used represent a WPP
WPPs	Wind Power Plants
WPP	Wind Power Plant

Contents

List of Abbreviations	ix
1 Introduction	1
1.1 Problem Description	1
1.2 Objective of the thesis	3
1.3 Contributions of the thesis	3
1.4 List of publications	3
2 HVDC grid and the North Sea	5
2.1 HVDC transmission system	5
2.1.1 Point-to-point and meshed HVDC transmission system	6
2.1.2 Power flow model and NR method	8
2.1.3 Control of HVDC transmission system	9
2.1.4 Cost of VSC HVDC transmission system	11
2.2 HVDC grid in the North Sea	14
2.2.1 Existing power exchange in the North Sea	16
2.2.2 Energy cost, transmission tariff and NPV calculation	16
2.2.3 Wind power potential in the North Sea	17
2.3 ARIMA based time series modelling procedure	18
2.3.1 Standard Univariate ARIMA model	19
2.3.2 Standard Multivariate ARIMA model	22
3 Building HVDC grid in the North Sea	25
3.1 Case 1: Two bus system, base case	26
3.2 Case 2: Three bus system, with one WPP	27
3.3 Case 3: Six bus system, with three WPPs	28
3.4 Case 4: Nine bus system, with four WPPs	29
4 Time and space correlated wind speed modelling for wind power simulation	31
4.1 ARIMA based time correlated wind speed model	32
4.1.1 Measured wind speed time series data	32
4.1.2 Transformation of wind speed data	33
4.1.3 Model identification and diagnostic checking	34
4.1.4 Verification and final diagnostic checking	35
4.2 Modified ARIMA based modelling procedure	37
4.2.1 Limiting the range of modelled wind speed	37

4.2.2	Frequency decomposition	39
4.2.3	Shifting the wind speed data (Adding a constant offset value to the signal)	44
4.2.4	Flow chart of the modified ARIMA based wind speed modelling procedure	44
4.3	Application of the proposed modelling procedure	45
4.3.1	ARIMA(6,0,0) for HF and LARIMA(0,1,6) for LF component of wind speed	45
4.3.2	A model to simulate wind speed in the Baltic sea area	47
4.4	Time and space correlated wind power model	51
4.4.1	Geographically distributed wind speed data in the North Sea	51
4.4.2	Time and space correlated wind speed model between two sites	52
4.4.3	Time and space correlated wind speed model among six sites	59
4.4.4	General recommendation on VARIMA model	62
5	Supervisory control in HVDC grids	63
5.1	Droop control strategy	64
5.2	Supervisory controller models	66
5.2.1	Architecture of primary and secondary control in an HVDC grid	68
5.2.2	Supervisory controller model for the system in Case 2	69
5.2.3	Supervisory controller model for the system in Case 3	71
5.2.4	Supervisory controller model for the system in Case 4	74
5.3	Limit of controllability in the HVDC grids	77
5.4	Voltage control in an HVDC grid	78
6	Economic analysis of HVDC grid in the North Sea	79
6.1	Case 1	80
6.1.1	Investment cost	80
6.1.2	Transmitted power and power loss	81
6.2	Case 2	81
6.2.1	Investment cost, base case	81
6.2.2	Effect of the WPP on the scheduled exchange power	82
6.2.3	Effect of the WPP on power loss	83
6.2.4	Effect of the WPP on added cost	84
6.2.5	Analysis of system reinforcement	85
6.3	Case 3	87
6.3.1	Investment cost of the base system	88
6.3.2	Effect of the WPPs on the scheduled exchange power	88
6.3.3	Effect of the WPPs on power loss	90
6.3.4	Effect of the WPPs added cost	91
6.3.5	Analysis of system reinforcement	91
6.4	Case 4	93
6.4.1	Investment cost of the system	93
6.4.2	Effect of the WPPs the scheduled exchange power	94
6.4.3	Effect of the WPPs power loss	95
6.4.4	Effect of the WPPs added cost	96

7	Conclusions and Future Work	97
7.1	Conclusions	97
7.2	Future Work	98
A	DC power flow equation	iii
B	Newton-Raphson method	vii
C	Stochastic time series model	ix
D	The Per Unit System	xi

Contents

Chapter 1

Introduction

1.1 Problem Description

In 2009, the EU and the G8 Heads of governments committed their countries to an 80% reduction in GHG (Green House Gas) emissions by 2050. A good example of an initiative designed to achieve part of the commitment is the EU 20-20-20 where one of its target is to increase the share of renewable energy by 20% by 2020 [1]. Wind is an important part of the renewable energy and offshore wind constitutes a significant percentage of the renewable energy in Europe [2]. The current (2013) offshore wind capacity in Europe is 6,562 MW and it is expected to reach 150,000 MW in 2030 [3], [4]. However, the benefits from wind power come with challenges where integrating an increased wind power is creating bottle necks in the existing power systems [5], [6], [7]. In order to reduce the impacts of wind power integration on the system, it is believed that interconnecting WPPs, which are distributed over large geographical areas, can play positive roles due to time and space correlation of wind power over the areas which result in smoothing effect [8], [9], [10], [11].

Moreover, there is a growing trend of offshore wind farm installations due to environmental concerns, public acceptance and availability of wind energy resources [12]. In addition, the majority of the sites considered for offshore wind energy projects are situated close to the coasts (up to few hundred kilometres). However, exploiting the vast wind energy resources in the offshore areas means moving much further out to the sea. Hence, it is expected that WPPs in the GW scale will be installed hundreds of kilometres from the shore and over large areas where good wind conditions are available [12], [13]. Due to the wide geographical area and the distance in question, a MTHVDC (Multi-Terminal High Voltage Direct Current) or a meshed HVDC grid could be used to transport the energy from the WPPs to the external AC connection points. The choice of an HVDC over an HVAC technology for this application is mainly due to techno-economic reasons [13], [14], [15].

In addition to the transportation of energy from the WPPs, the meshed HVDC grid can enhance the reliability of the transnational grid interconnections [16]. An example of such an area, where large scale WPP integration and a meshed HVDC grid are expected, is the North Sea region. An offshore meshed HVDC grid in this area can interconnect

different member states in the region and enable wind power in GW scale to be transported to the external AC connection points. In addition, the meshed HVDC grid in the region can enhance the security of power supply and facilitate competition of electricity trade among countries. The NSCOGI (North Seas Countries Offshore Grid Initiative) describes the advantages of such an offshore grid as providing security of power supply, competition of electricity markets and integration of offshore renewable energy resources [17], [18], [19].

However, such a grid does not exist in the region today and it is unlikely that it can be built at once. According to a working group in CIGRE (International Council on Large Electric Systems), the first step towards a fully meshed HVDC grid is a simple non-meshed multi-terminal configuration [20]. This development could start from an inter-connector or from an offshore WPP connection. For example, in the North Sea region, there are several HVDC-cables which are used to transport energy between various countries. The longest of these inter-connectors is the NorNed cable (580 km) connecting an area in Norway and to an area in the Netherlands [21]. Expanding this system by integrating a WPP or WPPs can result in technical and economical challenges and opportunities to the existing system; the aspects that have not been properly addressed in the previous studies so far.

There are some studies on HVDC grids in general and HVDC grids in the North Sea region in particular. For instance, in [16] the aim of the North Sea transnational grid research project was described. In [19] and [22], an overview of the possible technologies that can be used in the building of the grid in the North Sea area were described. In [23] an overview of the technical, economical and regulatory obstacles of building a European super grid was discussed. In [24], a bench mark test system for the offshore grid in the North Sea was presented. In [25], an overview of a feasibility study of offshore HVDC grid was made where the focus was on the need for a highly reliable coordinated control functions for the system and the need for selective protection plan for a reliable operation of the system. In [26], steady state and dynamic modelling of VSC (Voltage Source Converter) HVDC systems for power system simulation were presented. A study on MTHVDC networks with a focus on system integration, dynamics and control was made in [27]. However, the study in [27] lacks a detailed steady state analysis of different systems in the area of interest. In [28], control, dynamics and operation of VSC MTHVDC transmission system was studied. From an operation and a control point view, the main focus of the study in [28] was on a precise control of scheduled powers in a system operated by a voltage droop controllers. In addition, the concept of a secondary control was also introduced where the main focus was to restoring some of the deviation in the scheduled powers resulting from the actions of the voltage droop controllers in the system.

The literature survey on the previous studies indicates that there is lack of detailed investigations of HVDC grids at steady state. To the author's knowledge, there are hardly any publicly available studies that investigated and quantified the economical aspects of building HVDC grid in general and the HVDC grid in the North Sea region in particular. Building an HVDC by connection a WPP or WPPs onto a system designed for power exchange results in technical challenges and the proposed control strategies in the literature were not developed around these challenges. In addition, in order to investigate the building or the expansion of the system by using WPPs, it is important to develop a model that can be used to simulate time and space correlated wind power data from the WPPs.

1.2 Objective of the thesis

The objective of this thesis is to investigate and quantify some of the economical and technical aspects of building the HVDC grid in the North Sea region at steady state. Specifically, the objective is to investigate the impact of integrating a WPP or WPPs into a transmission system built for power exchange. In order to conduct this study, an obvious objective is to first develop a control strategy that can be used to enable the integration WPPs into a system which is built for power exchange. In addition, the objective is to model time and space correlated power from the WPPs and to establish the possible power exchange data in the area of interest. The last, but not the least, objective is to develop a procedure that can be used to determine different costs in the system such as the investment costs of the systems, the cost of power loss, the cost of altering scheduled power exchanges and the cost of transmission or transmission tariff in the system.

1.3 Contributions of the thesis

To the best knowledge of the author, the following are the main contributions of this study.

- A procedure that can be used to study the economics of building an HVDC grid in the North Sea and similar areas is one of the main contributions of the thesis. The procedure combines wind power modelling, steady state control of the system and calculations of different cost elements in the system from which recommendations on system design and reinforcement can be made.
- A modified ARIMA based modelling procedure for the application of wind power simulation is another contribution of the thesis. In addition, a model structure and the corresponding model parameters that can be used to simulate time series wind speed data in the Baltic Sea area for a given average wind speed is also another useful contribution of the thesis.
- A steady state control strategy which is based on local droop (primary) control followed by central secondary (supervisory) control is another contribution of the thesis that cannot be ignored. The control strategy can be used to enable to the integration WPPs onto a system which is designed for power exchange.

1.4 List of publications

The publications resulting from this thesis are listed as follow

- I K. Yunus, T. Thiringer, and P. Chen, " Arima-based frequency-decomposed modelling for wind power simulation and a common model to simulate wind speed at multiple locations," Submitted to IEEE Transactions on Power Systems.

Chapter 1. Introduction

- II K. Yunus, T. Thiringer, and O. Carlson, "Steady state control strategy for a meshed hvdc grid with wind power plants," in 12th Wind Integration Workshop, International Workshop On Large Scale Integration of Wind Power into Power System as well as on Transmission Networks for Offshore Wind Power Plants, 2013.
- III K. Yunus, T. Thiringer, and O. Carlson, "Droop based steady state control algorithm for a meshed hvdc grid," in 2014 IEEE PES Transmission and Distribution Conference and Exposition; 15-17 April 2014 in Chicago, IL, USA, 2013.

The author has also contributed to the following publications

- I K. Yunus, H. De La Parra, and M. Reza, "Distribution grid impact of plug-in electric vehicles charging at fast charging stations using stochastic charging model," in Proceedings of the 2011-14th European Conference on Power Electronics and Applications (EPE 2011), Aug. 2011, pp. 1-11.
- II K. J. Yunus, M. Reza, H. Zelaya-De La Parra, and K. Srivastava, "Impacts of stochastic residential plug-in electric vehicle charging on distribution grid," in Innovative Smart Grid Technologies (ISGT), 2012 IEEE PES, Jan. 2012, pp. 1-8.
- III K. Yunus, G. Pinares, L. Tuan, and L. Bertling, "A combined zone-3 relay blocking and sensitivity-based load shedding for voltage collapse prevention," in Innovative Smart Grid Technologies Conference Europe (ISGT Europe), 2010 IEEE PES, Oct. 2010, pp. 1-8.
- IV A. Marinopoulos, J. Pan, M. Zarghami, M. Reza, K. Yunus, C. Yue, and K. Srivastava, "Investigating the impact of wake effect on wind farm aggregation," in PowerTech, 2011 IEEE Trondheim, Jun. 2011, pp. 1-5.

Chapter 2

HVDC grid and the North Sea

In this chapter, materials from literature which are necessary to achieve the objectives of the thesis are presented. In the first part of this chapter, the topology of a typical HVDC transmission system, power flow model of the system, control strategy in the system and investment cost of the system are presented. In the second part of this section, the vision of an HVDC transmission grid in the North Sea, existing exchange power profiles in the area, cost of energy and transmission tariff in the area as well as available wind power potentials in the area are presented. In the last part of the chapter, a standard ARIMA based time series modelling procedure, which can be used for wind power simulation, is presented.

2.1 HVDC transmission system

In the history of electric power system, DC was the first type of transmission that was used in the early days. Although AC transmissions later on came to play important roles, the development of DC transmissions has continued [29]. Today, the wish to transport bulk power over long distances, and in particular under the sea, has raised interest in DC transmission system, which nowadays referred to as HVDC due to the high voltage involved. An important component of an HVDC transmission system is the converter which is used to convert AC to DC or DC to AC. There are different types of converter technologies and CSC (Current Source Converters) are still the most used for the application of bulk power transmission. However, VSC (Voltage Source Converter) is becoming popular for HVDC transmission applications. This is mainly because of its higher flexibility compared to the classical CSC [30], [31].

There are a number of VSC based HVDC transmission systems commissioned worldwide and systems with power ratings from a few tenths of MW up to over 1000 MW are available [32]. Table 2.1 shows some of the existing VSC based HVDC transmission systems world wide [30], [32]. As can be seen from the figure, almost all of the existing VSC HVDC transmission systems are point-to-point and meshed HVDC transmission systems do not exist today. According to the data in the table, the highest voltage and power in the installed systems is ± 350 kV and 600 MW respectively

Table 2.1: Examples of VSC HVDC projects worldwide

Project	Capacity	Voltage	Distance	Cost	Year	-shore	Country(s)
Gotland HVDC Light®	50MW/ ± 25MVar	± 80 kV	2 x 70 km		1999	Off	Sweden
Directlink	3 x 60 MW	± 80 kV	6 x 65 km		2000		Australia
Tjæreborg	8 MVA	± 9 kV	2 x 4.5km		2000	Off	Denmark
Eagle Pass	36 MVA	132 kV	Back2back		2000		US
MurrayLink	200 MW	± 150 kV	2 x 180 km		2002		Australia
Troll A	2 x 40 MW	± 60 kV	4 x 68 km		2005	Off	Norway
Estlink	350 MW	± 150 kV	2 x 105 km		2006		Finland
Valhall	78 MW	150 kV	300 km		2009		Norway
BorWin1	400 MW	± 150 kV	2 x 200 km		2009	Off	Germany
Caprivi Link	2 x 300 MW	± 350 kV	970 km		2009		Zam/Nam

2.1.1 Point-to-point and meshed HVDC transmission system

A meshed HVDC grid can be seen as an interconnection of point-to-point transmission systems. A point-to-point HVDC transmission system connects two points in a system where each point is equipped by a converter station. There are different configurations of point-to-point HVDC transmission systems and Figure 2.1 shows the main elements of a bipolar VSC HVDC transmission system. The system is composed of two VSCs and a transmission link connecting the two converter stations. Each converter is connected to an AC grid through a phase reactor, a filter and a transformer [30].

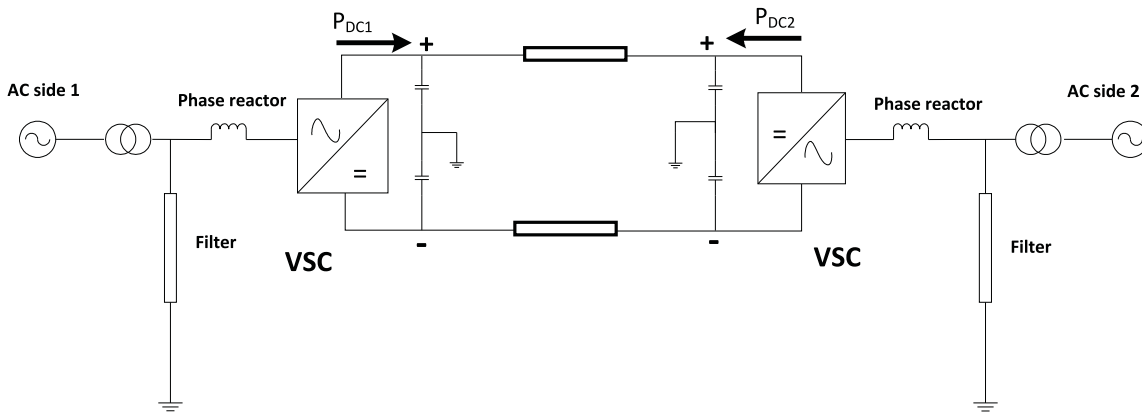


Figure 2.1: Point to point VSC HVDC transmission system

A meshed HVDC grid can be formed from point-to-point transmission systems where two or more branch cables share the same converter in the system an example of which is shown in Figure 2.2. Similar to a point-to-point HVDC transmission system, there are different ways of configuring a meshed HVDC transmission system [30], [20]. Figure 2.2 shows an example of configuring a six terminal HVDC transmission system. Six AC connections, out of which two are WPPs, are connected to the grid. Note that the phase reactors, the filters and the transformers are omitted from the circuit for the sake of simplicity.

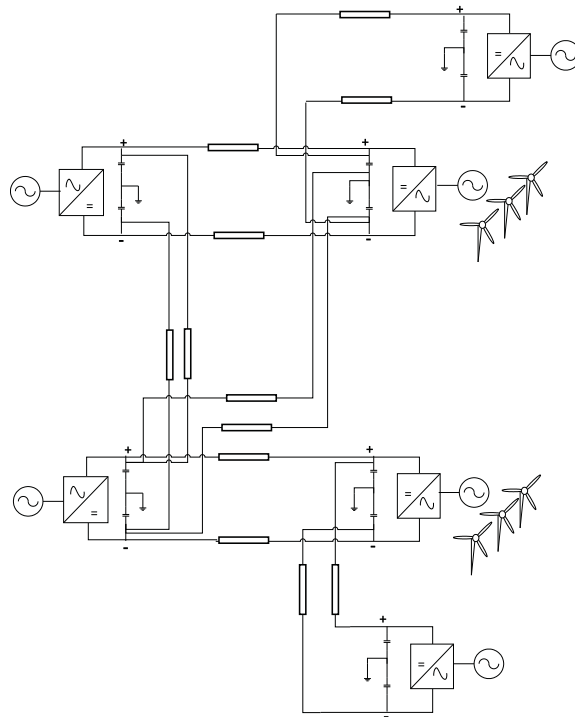


Figure 2.2: Six terminal meshed HVDC transmission system with two WPPs and four external AC connection points

Figure 2.3 shows a simplified presentation of the HVDC grid presented in Figure 2.2 to make the overview of the system simpler [33], [34].

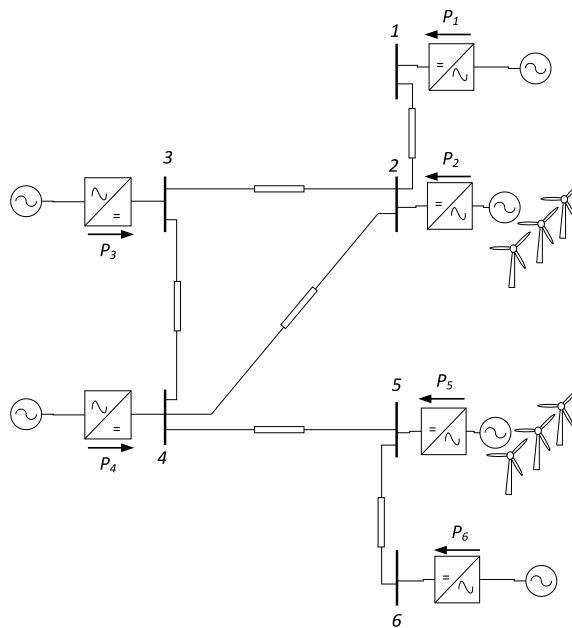


Figure 2.3: Simplified six terminal meshed HVDC transmission system with two WPPs and four external AC connection points

2.1.2 Power flow model and NR method

A power flow equation of an HVDC grid can be developed by using the same procedure as that for AC [35], [26]. Appendix A shows the steps required to develop a generic AC power flow equation for a power system with any number of buses and a derivation of a power flow equation for a DC side of a meshed HVDC grid. The generic power flow equation of the DC side of a meshed HVDC grid is formulated as

$$P_k = \sum_{j=1}^N |U_k| |U_j| G_{kj} \quad (2.1)$$

where P_k is active power injected at bus k , U_k and U_j are DC voltages at bus k and j respectively, G_{kj} is conductance of the branch connecting bus k and bus j and N is the number of buses in a system.

The power flow equation presented in (2.1) is non linear and requires a non-linear method to solve it. Hence, the NR (Newton-Raphson) method, presented in Appendix B, is used to solve the power flow equation in (2.1). The system variable in (2.1) is the nodal voltage U . Hence, the deviation in the solution of the nodal voltage at the n^{th} iteration is given by

$$\begin{bmatrix} \Delta P_1^{[n]} \\ P_2^{[n]} \\ \vdots \\ \Delta P_N^{[n]} \end{bmatrix} = \begin{bmatrix} J_{11} & J_{12} & \cdot & \cdot & \cdot & J_{1N} \\ J_{21} & J_{22} & \cdot & \cdot & \cdot & J_{2N} \\ \cdot & \cdot & \cdot & \cdot & \cdot & \cdot \\ \cdot & \cdot & \cdot & \cdot & \cdot & \cdot \\ J_{N1} & J_{N2} & \cdot & \cdot & \cdot & J_{NN} \end{bmatrix} \begin{bmatrix} \Delta U_1^{[n]} \\ \Delta U_2^{[n]} \\ \cdot \\ \cdot \\ \Delta U_N^{[n]} \end{bmatrix} \quad (2.2)$$

$$\Rightarrow [\Delta P^{[n]}] = [J][\Delta U^{[n]}] \Rightarrow [\Delta U^{[n]}] = [J]^{-1}[\Delta P^{[n]}]$$

where $\Delta U^{[n]}$ is the deviation in the solution of the nodal voltage U at the n^{th} iteration, J is the Jacobian matrix which a function of the partial derivatives of the function f (refer Appendix B for detail), $\Delta P^{[n]}$ which is defined as

$$\Delta P^{[n]} = P - f(U^{[n]}) \quad (2.3)$$

By using the deviation in the solution of the nodal voltage $\Delta U^{[n]}$ at the n^{th} iteration, the bus voltage can be updated into

$$U^{[n+1]} = U^{[n]} + \Delta U^{[n]} \quad (2.4)$$

The function f in (2.3) is related to the power flow in (2.1), and it is expressed as

$$f(U_k) = U_k \sum_{j=1}^N Y_{kj} U_j = U_k^2 Y_{kk} + U_k \sum_{j=1, \neq k}^N Y_{kj} U_j \quad (2.5)$$

Note that the elements of the Jacobian matrix in (2.2) are all expressed in terms of the partial derivatives of the system function f with respect to the system variables, which are the bus voltages in this case. The partial derivatives of this function when the row and column indices of the Jacobian matrix are equal ($k = j$) and when they are different ($k \neq j$), respectively, are expressed as

$$\begin{aligned}\frac{\partial f_k}{\partial U_k} &= 2U_k Y_{kk} + \sum_{j=1, \neq k}^N Y_{kj} U_j \\ \frac{\partial f_k}{\partial U_j} &= Y_{kj} U_k\end{aligned}\quad (2.6)$$

Using the relations in (2.6), the elements of the Jacobian matrix are calculated.

In order to solve (2.2), one of the system buses is used as a reference (or slack) bus. At the reference bus, the bus voltage is fixed (say to 1 pu) and the injected power at the bus is equal to the power at all other buses and the power loss in the system. As a result, the rows and columns containing the reference bus is removed from (2.2) and the remaining system of equations is solved. Using the solutions, the power injected at the reference bus is calculated using (2.1). The resulting power at the reference bus can be either positive (generation) or negative (load).

2.1.3 Control of HVDC transmission system

A power flow in an HVDC transmission system is the result of the actions of the controllers in the converter stations [33]. The objective of a power flow control in an HVDC transmission system is to control the DC voltage in the system within its limits and fulfilling the power input/output at the PCC (Point of Common Coupling) to the AC system without exceeding maximum currents through the valves, lines or cables [20]. Figure 2.4 shows a block diagram of a controller at one converter station in a point-to-point HVDC transmission system. As can be seen from the block diagram, the controller can be set in

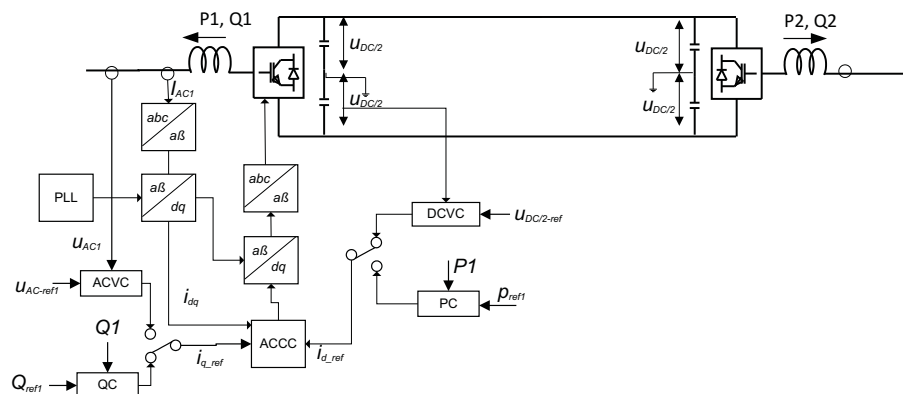


Figure 2.4: Control in a point-to-point HVDC transmission system

different control modes. On the AC side of the converter, either AC voltage or reactive power can be controlled. On the DC side of the converter, either DC voltage or DC power

can be controlled, which is the control mode relevant for the study in this thesis, since only the DC side of the grid is considered.

In a point-to-point HVDC transmission system, if one converter controls the DC voltage, the other converter controls DC power [28]. However, controlling a meshed HVDC grid is not as simple as controlling a point-to-point HVDC transmission system. Several methods are suggested in the literature to control a power flow in a meshed transmission grid [34], [28]. Among these methods, voltage droop control strategy is the most popular. The basic principle of voltage droop control in the DC system is similar to frequency droop control in an AC system. In an AC system, droop control is used as a primary control, using frequency as power balance signal, to share power deviation (resulting from disturbances in the system) among different generators in the system having the control capability [35].

However, in a DC grid, power balance signals are system bus voltages. When there is less power injected into a DC grid, the system bus voltages decrease and vice versa. Hence, in a meshed HVDC grid with local droop controllers, when the system bus voltages decrease, the droop controllers react by injecting more power into the system. Similarly, when the system voltages increase, the droop controllers react by reducing the power injected into the system so that the system bus voltages decrease. Figure 2.5 shows a droop controller at a converter station. Observe that for a negative value of the droop characteristics (m), when the bus voltage (U) is less than the reference (U_{ref}), the reference power to the converter (P_{ref}) gets higher. Similarly, when the bus voltage is higher than the reference voltage, the reference power to the converter gets lower.

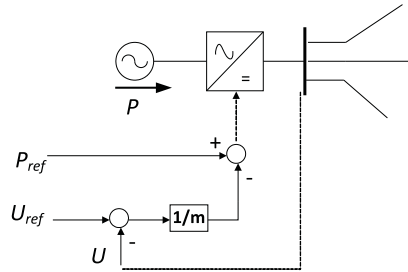


Figure 2.5: Droop controller at a converter station

The magnitude of the reaction of a local droop controller depends on the magnitude of the slope of the droop characteristics used in the controller (m). Figure 2.6 shows a voltage droop characteristics. It is a linear relationship defined by a voltage and a power of a bus in a system. For a given slope of the droop characteristics (m) used in a droop controller, the magnitude of the reaction of the droop controller can be calculated as

$$\frac{\Delta U_k}{\Delta P_k} = \frac{U_k - U_{k0}}{P_k - P_{k0}} = m_k \implies \Delta P_k = \frac{1}{m_k} \Delta U_k \quad (2.7)$$

The relation in (2.7) can be combined with the DC power flow equation in (2.1) to form a steady state model of the power flow equation with the local droop controllers. Assume that bus k has droop control capability with a voltage droop characteristics having a slope m_k , and assume also that P_k is the scheduled or reference power injected at the same bus. If there is a deviation in voltage at bus k (ΔU_k) from the reference due to a

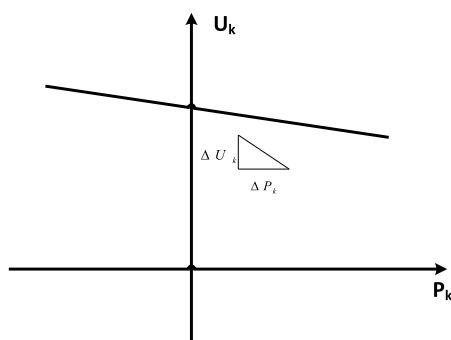


Figure 2.6: Standard voltage droop characteristics

disturbance; the reference power at the bus (P_k) is reduced by an amount ΔP_k , which is given in (2.7). The steady state model of the HVDC grid with droop controllers can then be formulated as

$$P_k - \Delta P_k = P_k - \frac{1}{m_k} \Delta U_k = U_k \sum_{j=1}^n G_{k,j} U_j \quad (2.8)$$

where P_k is the scheduled or the reference power injected at bus k , ΔU_k is the change in voltage at bus k and m_k is the slope of the droop characteristics at bus k which must have a negative value.

In a given HVDC grid, some buses in the system may not have droop control capability. Hence, in a system having n number of buses, if a converter at bus k does not have droop control capability, the value of the slope m_k in (2.7) is set to ∞ to represent this. If the value of m_k in (2.7) is ∞ , ΔP_k will be zero, for any value of ΔU_k . From control point of view, the controller at bus k controls the bus power to a fixed reference value, P_k . If the value of m_k is zero, it means that the bus k is a slack bus (the change in voltage at the bus is zero). In general a typical recommended value of the droop parameter, m_k , ranges from 3% to 4% [28].

2.1.4 Cost of VSC HVDC transmission system

Economic analysis is probably the most important aspect of steady state analysis of an HVDC transmission grid. The total cost of a VSC HVDC transmission system is mainly composed of the cost of transmission cables, the cost of VSC converters and installation cost [36], [37]. In this section, these costs are formulated to assist the calculation of the total investment cost of an HVDC transmission system.

Cost of cables

Cost of cables constitute a major part of the total investment cost of an HVDC grid. ENTSO-E (European Network of Transmission System Operators for Electricity)

has summarized different costs of HVDC transmission cables in one of its report [36]. Table 2.2 shows average costs of some of the subsea cables presented in the report. Note that the costs are in euro (€) per meter of cable supplied excluding installation cost.

Table 2.2: Cost of extruded subsea HVDC cable for 320 kV voltage level

Cross-sections Area (mm^2)	ENTSO–E Cost (€/m)
1200	345–518
1800	345–575
2000	403–660

It is often difficult to get the cost of cables used in a specific study. An example for this is the unavailability of the cost information for the list of cable technologies used in this study which are obtained from an industry report [32]. This is because cost data is often a sensitive information for an industry and it is often obtained from commissioned projects. This makes it important to develop an expression that can be used to estimate cost of a cable for a given voltage and power ratings. Such an expression to calculate the cost of HVDC cable is developed in [38], [39], which is formulated as

$$Cost = A_p + B_p S_n \quad (2.9)$$

where $Cost$ is the unit cost of a cable in a bi-pole configuration in SEK/km , S_n is the rated power of the bi-pole configuration in $watt$, and A_p , B_p are constants related to specific system voltage. For a voltage level of ± 320 kV, the parameters are given as $A_p = 2 \times 10^6$ and $B_p = 0.006$ [38], [39].

By using (2.9), the costs of some of the submarine cables presented in [32] are estimated. Table 2.3 shows the comparison of the costs of cables from the ENTSO–E report and the equivalent estimated cost of the cables from the report in [32] calculated using (2.9). The results in the table show that the relation in (2.9) can be used to estimate the cost of HVDC transmission cables with a voltage level of ± 320 kV. Note that the relation in (2.9) considers the cost of cables in SEK. To convert SEK into €, an exchange rate of 9 SEK per € is assumed, which is an average exchange rate during the year 2008 to 2014.

Table 2.3: Cost of extruded subsea HVDC cable for 320 kV voltage level

Cross-sections Area (m^2)	S_n (Watt) (bi-pole set-up)	ENTSO–E cost (€/m)	Estimated using (2.9) cost (€/m)
1200	943×10^6	345–518	425.4444
1800	1190×10^6	345–575	507.7778
2000	1272×10^6	403–660	535.1111

By following a similar procedure as in Table 2.3, the estimated costs of some of the submarine cables in [32] with a voltage level of ± 320 kV are calculated by using the relation in (2.9). The results are presented in Table 2.4. Note that the cable power in Table 2.3 are given for the two cables in the bipolar configuration while the costs of the cables are given for a single cable in the bipolar configuration.

Table 2.4: Comparison given and estimated cable cost information for bipolar submarine HVDC transmission cables with a voltage level of ± 320 kV

Cable ID	Area (mm^2) per pole	Resistance (ohm/km, 20^0C) per pole	Rated current(A) per pole	Rated Power(MW) per bi-pole	Cable cost per pole (€/m)
1	95	0.193	338	216	183
2	120	0.153	387	248	194
3	150	0.124	436	279	204
4	185	0.0991	496	317	217
5	240	0.0754	580	371	235
6	300	0.0601	662	424	252
7	400	0.0470	765	490	274
8	500	0.0366	887	568	300
9	630	0.0283	1030	659	331
10	800	0.0221	1187	760	364
11	1000	0.0176	1355	867	400
12	1200	0.0151	1474	943	425
13	1400	0.0126	1614	1033	455
14	1600	0.0113	1745	1117	483
15	1800	0.0098	1860	1190	508
16	2000	0.0090	1987	1272	535
17	2200	0.0080	2086	1335	556
18	2400	0.0073	2198	1407	580

Cost of VSC

The cost of VSC is another important component of the total cost of an HVDC transmission system. The study made in one of the European Commission projects, called

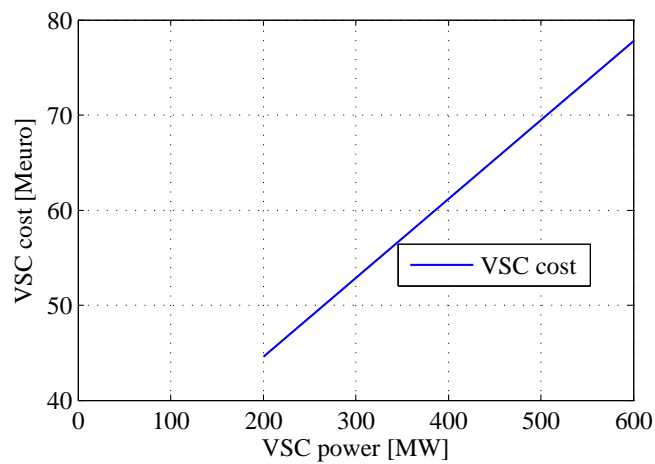


Figure 2.7: Cost of VSC converter as a function of power rating

REALISEGRID [37], has developed a relationship between the cost of a VSC as a function

of power rating as can be seen in Figure 2.7. The relationship in the figure is formulated as

$$Cost[Meuro] = 0.083P[MW] + 28 \quad (2.10)$$

where $Cost$ is the cost of the VSC in M€ and P is the rated power of the converter in MW [40]. Figure 2.7 shows how the cost of the VSC converter changes as a function of power.

In order to verify the validity of the VSC cost model in (2.10), the cost of a VSC presented in the ENTSO-E report are used [36]. The cost of VSCs presented in the report include the cost of AC switch yard stations excluding the cost of platforms [36]. Table 2.5 presents the comparison the costs of VSC from ENTSO-E and the corresponding estimated costs of the VSC using the model in (2.10). The results show that the model can be used to make a good estimate of the cost of VSC especially when the voltage levels are above 320 kV. Hence, this relation can be used to fairly estimate the cost of the VSC considered in this study which have a voltage level of ± 320 kV (640 kV).

Table 2.5: Comparison the cost of VSC from ENTSO-E and the corresponding cost estimated by the relation in (2.10)

Converter Technology	Power(MW)	Voltage(kV)	ENTSO-E cost (M€)	Estimated cost (M€) using (2.10)
VSC	500	300	75 – 92	69.5
VSC	850	320	98 – 105	98.55
VSC	1250	500	121 – 150	131.75
VSC	2000	500	144 – 196	194

Installation cost of the system

According to the report from ENTSO-E in [36], the cost of installation varies greatly in the range of 230 to 977.5 € per meter. Some of the factors affecting this price are the market conditions for specialist vessels, the location of cable installation relative to the supplier's manufacturing facilities, the type of cable and its burial depth, the number of cables and the configuration and the rating of the cable and its size. In this thesis, an average installation cost of 604 € per meter is used.

2.2 HVDC grid in the North Sea

As stated before, a meshed HVDC transmission grid does not exist today in the North Sea region or elsewhere. However, there are a number of HVDC transmission systems in the North Sea area which are used for different purposes. An example of an HVDC transmission system in the region is the NorNed HVDC transmission link which is used to connect the power systems in Norway and in the Netherlands [41]. Another example is the BorWin1 HVDC transmission system which is used to connect offshore wind farms to the

2.2. HVDC grid in the North Sea

shore in Germany. There are a number of similar other HVDC transmission systems in the area which are in operation.

Moreover, there is a growing interest to have a meshed HVDC grid in the North Sea area. There are a number of forces driving the idea of building the meshed HVDC grid in the area. One of the driving force is a market force; the desire to generate more revenue by transporting more exchange power over the meshed HVDC grid. Another driving force is the need to enhance security of power supply in the region by using the interconnected systems. In addition, there is also a growing interest to integrate more WPPs into the electric power system in the region, which is another driving force. Hence, there are a number of planned HVDC transmission projects in the area to realise the future meshed HVDC grids.

As a result of the increasing interest to build an HVDC grid in the North Sea region, some stakeholders have already proposed the visions of the meshed HVDC grid in the North Sea region. Figure 2.8 shows a vision of the future HVDC grid in the region proposed by EWEA (European Wind Energy Association) [42]. Similar visions are also proposed by



Figure 2.8: Vision of HVDC grid in the North Sea area proposed by EWEA. Existing HVDC links in the area are also indicated in red in the figure [42].

many other organizations like Airtricity, Sintef and Statnett [28]. Figure 2.8 also shows the existing offshore transmission links in the region and the wind power potential in the areas considered to be feasible for WPP development.

2.2.1 Existing power exchange in the North Sea

Existing exchange power data in the North Sea is one of the important input data required to investigate different scenarios of HVDC transmission systems in the area. As can be seen in Figure 2.8, there are limited number of existing transmission links in the area. Figure 2.9 shows the duration curve of the exchange power profiles on some of the existing transmission links. The exchange data is obtained from Nord Pool spot during the year 2012 [43]. For instance, the blue curve in the figure shows the annual duration curve of the exchange power between Denmark and Germany. The result shows that Germany injects power into Denmark for about 18% of the year; for the other 82% of the year, Denmark injects power into Germany. Similarly, the green curve shows the annual duration curve of the power exchange between Denmark and Norway; and the red curve shows the annual duration curve of the exchange between the Netherlands and Norway.

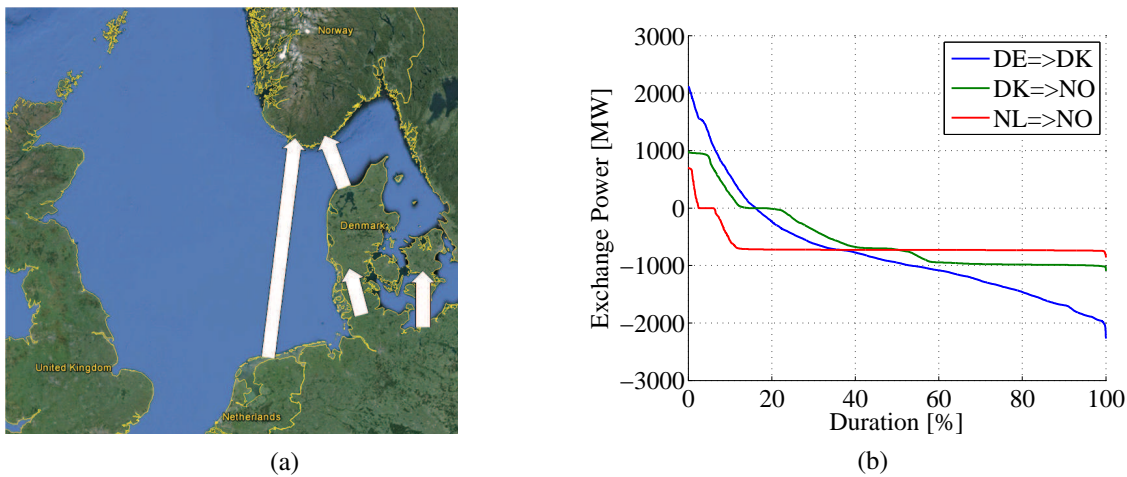


Figure 2.9: Existing power exchange profiles in the North Sea area (a) directions of power flow (b) annual durations curve

2.2.2 Energy cost, transmission tariff and NPV calculation

As stated before, economic analysis is an important aspect of steady state analysis in an HVDC transmission system. In order to make an investment decision to build a new HVDC transmission system or to reinforce the existing system, it is important to know the cost of energy, the cost of transmission and the cost of changing scheduled exchange power. According to a report from the European commission entitled '*Energy prices and costs report*' [44], the average cost of energy in the main whole sale European markets during 2007 to 2014 is about 50 € per MWh. Similarly, according to a report from ENTSO-E, the average cost of transmission (transmission tariff) in the countries of the North sea region is about 10 € per MWh [45]. In this study, the cost of altering the scheduled exchange power is assumed to be the same as transmission tariff. All the costs stated above are to be paid continuously over time. Hence, NPV (Net Present Value) calculation is the appropriate tool to use to calculate the cost of altering the scheduled exchange power, the cost of power

loss and transmission costs in the system. The results from the NPV calculations can be used as a basis to make an appropriate investment decision.

In economics, present value, also known as present discounted value, is a future amount of money that has been discounted to reflect its current value, as if it existed today [46]. If A is the amount of money to be paid by the end of n years and i is the interest rate during this time, the present value of A is calculated as

$$PV(A) = \frac{A}{(1+i)^n} \quad (2.11)$$

Similarly, if an amount of money, A , is paid every year for n number of years; the NPV of the money accumulated over n years can be calculated as

$$NPV(A) = \frac{A}{(1+i)^1} + \frac{A}{(1+i)^2} + \dots + \frac{A}{(1+i)^n} = \frac{A}{i} \left[1 - \frac{1}{(1+i)^n} \right] \quad (2.12)$$

NPV calculation can be used as a basis for a proper investment decision. In this thesis, NPV calculation is used to calculate the cost of altering or changing the scheduled power, the cost of power loss and the cost of transmission over a certain investment period of an HVDC transmission system. The result from the NPV calculation can be used to make a decision whether the system needs to be reinforced or not.

2.2.3 Wind power potential in the North Sea

According to EWEA, there is more than 65,000 MW harvest-able wind power capacity in the North Sea alone [42]. Figure 2.10 shows the distribution of wind power potential in the area. As can be seen from the figure, the wind power resource in the region is divided into four areas to facilitate the investigation of different grid scenarios in the area.

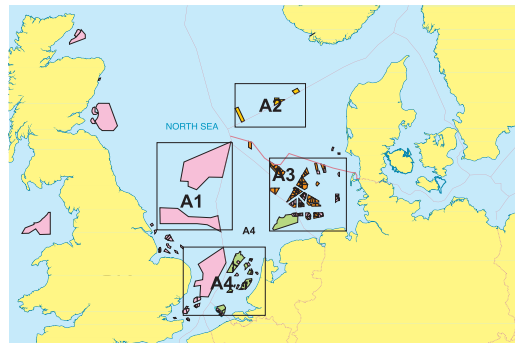


Figure 2.10: Estimated WPP cluster points in the North Sea

Estimated values of offshore wind power capacities in the areas marked A1, A2, A3 A4 in Figure 2.10 are about 13 GW, 3.5 GW, 24 GW and 25 GW respectively. Note that the total wind power capacities in each area are the sum of the capacities of the existing WPPs,

WPPs that are under construction and planned WPP areas for future use [42]. Based on these data, different penetration levels can be considered to investigate the HVDC transmission grids in the area under different scenarios. For a given WPP capacity, the corresponding power from the WPP (which is another important input data for system analysis) can be calculated by using the wind speed at the WPP and the equivalent power curve of the WPP.

2.3 ARIMA based time series modelling procedure

Wind power from a given WPP is a function of wind speed at the WPP. For a given wind speed at the WPP, the power output from the WPP is governed by a characteristic power curve of the WPP [47], [48], [49]. Figure 2.11 presents different power curve models of WPPs (turbine and area power curve) developed by the TradeWind project [50]. Figure 2.11(a) shows the turbine power curve models for different applications. The figure shows that the output electrical power from the wind turbine is zero if the wind speed is less than a certain value. The wind speed value below which the turbine power is equal to zero is called *Cut – in speed*. If the wind speed is greater than the *Cut – in speed*, the turbine power output starts to increase as the speed increases until the speed reaches the *rated output wind speed* at which the turbine output is at the rated power. If the wind speed increases above the *rated output wind speed*, the turbine output power remains constant to its rated value until the wind speed reaches the *Cut – out speed*. If the wind speed is greater than the *Cut – out speed*, the turbine output power reduces to zero. Observe that the maximum output power from the model (100%) is the rated power of the turbine. Figure 2.11(b) shows the area power curve models for different applications. Note that the maximum output power from the power curve model is less than 100% which is due to the loss in the system [50].

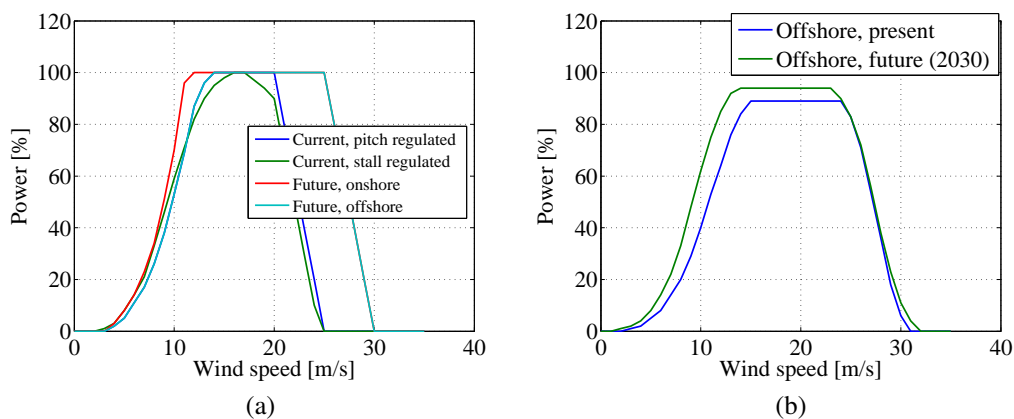


Figure 2.11: Power curve models (a) turbine power curves (b) equivalent area power curves according TradeWind [50]

As described above, wind power is a function of wind speed. Hence, an important step to model wind power time series data from a WPP is to model wind speed time series data

at the WPP. Wind speed time series data is stochastic in nature and some of its important characteristics are strong time correlation, periodicity and probability distribution.

There are different types of wind speed models. Some of these are the discrete Markov model [51], [52], [53] and ARIMA based models [54], [47], [48], [55]. The discrete Markov model has three major problems; quantisation error, many model parameters and require a large set of time series data compared with the ARIMA based model [49]. ARIMA based wind speed model is a time series model which is easy to implement and does not have much of the problems of the Markov method [56], [57], [58]. In this section, a summary of the standard ARIMA based modelling procedure is presented. Interested readers are referred to [59], [60] for more detailed information.

2.3.1 Standard Univariate ARIMA model

Let $y(1), y(2), \dots, y(N)$ be an observed time series data which is modelled by a random process $Y(t)$ (refer Appendix C). The standard ARIMA model of the process, $Y(t)$, is expressed as

$$\left(1 - \sum_{i=1}^p \phi_i B^i\right) (1 - B)^d Y(t) = \theta_0 + \left(1 - \sum_{i=1}^q \theta_i B^i\right) a(t) \quad (2.13)$$

where p is the order and ϕ_i are the coefficients of the AR(Auto Regressive) components; B is a back shift operator where $B^i Y(t) = Y(t - i)$; d is the degree of differencing which is used to transform data with time dependent mean to data with time independent mean; $Y(t)$ is the time series model; θ_0 is referred to as a deterministic trend term; q is the order and θ_i is the coefficient of the MA(Moving Average) component and $a(t)$ is a white Gaussian noise with zero mean and variance of σ_a^2 [59], [60].

The model in (2.13) has $p + q + 2$ unknown variables; the deterministic trend term θ_0 , the AR coefficients $\phi_1, \phi_2, \dots, \phi_p$, the MA coefficients $\theta_1, \theta_2, \dots, \theta_q$ and the variance of the white noise σ_a^2 . The variables can be obtained from the observed data, $y(t)$, by using a maximum likely hood estimator, a Yule-Walker estimator, a least square estimator [59], [60].

The model in (2.13) is called the ARIMA(p, d, q) model of order p and q with ' d ' differencing level. When $d = 0$, the ARIMA(p, d, q) model is reduced into the ARMA(p, q) model. When $d = 0$ and $q = 0$; the ARIMA(p, d, q) model is reduced into an AR(p) model and when $p = 0$ and $d = 0$; the ARIMA(p, d, q) model is reduced into an MA(q) model.

For a time series data with a time dependent variance, the Box-Cox's power transformation can be used to stabilize the variance [59], [60]. The idea behind the Box-Cox's power transformation is to find the appropriate transformation factor v that can transform data with time dependent variance to data with time independent variance. The criteria for the selection of v is to find the value of v that minimizes the residual sum of squares which is calculated as

$$SS(v) = \sum_{t=1}^N \left(T(y(t)) - \widehat{m}_y \right)^2 \quad (2.14)$$

where $T(y(t))$ is a function of time and is calculated as

$$T(y(t)) = \frac{y^v(t) - 1}{vG^{v-1}} \quad (2.15)$$

and G is the geometric mean of the observed time series, which is a constant and can be calculated as

$$G = \left(\prod_{i=1}^N y(t) \right)^{1/N} \quad (2.16)$$

The power transformed data become $[y(t)]^v$. For a process with non-stationary mean and variance, the transformation to stabilize the mean and the variance needs to be done together. Since differencing can result in negative time series data, it is recommended to apply power transformation on the time series before differencing [59], [60].

Model Identification and Diagnostic Checking

In a time series analysis, the most crucial step is to identify the appropriate structure of an ARIMA model for a given time series data. The first stage of model identification can be done in three steps [59], [60]. The first step is to analyse the observed time series data and determine the required type of transformation (differencing and/or power transformation, if necessary). The second step is to identify the corresponding ARIMA model by comparing the estimated ACC (Auto Correlation Coefficient) and PACC (Partial Auto correlation Coefficient) of the transformed time series data with the theoretical ACC and PACC (refer Appendix C). For a given time series data $y(t)$, the estimated ACC at time lag k , $\hat{\rho}_y(k)$ can be calculated as

$$\hat{\rho}_y(k) = \frac{\frac{1}{N-k} \sum_{t=1}^{N-k} (y(t) - \bar{y})(y(t+k) - \bar{y})}{\sigma_y^2} \quad (2.17)$$

where \bar{y} and σ_y^2 are the mean and variance of the data respectively and N is the length of the data [59], [60]. Similarly, given the estimated sample ACC, $\hat{\rho}_k$, the estimated PACC of the data, $\hat{\Phi}_{kk}$, according to [59], [60], can be calculated as

$$\hat{\Phi}_{k+1,k+1} = \frac{\hat{\rho}_{k+1} - \sum_{j=1}^k \hat{\Phi}_{kj} \hat{\rho}_{k+1-j}}{1 - \sum_{j=1}^k \hat{\Phi}_{kj} \hat{\rho}_j} \quad (2.18)$$

and

2.3. ARIMA based time series modelling procedure

$$\hat{\Phi}_{k+1,j} = \hat{\Phi}_{kj} - \hat{\Phi}_{k+1,j+1}\hat{\Phi}_{k,k+1-j} \quad (2.19)$$

The third and last step is to determine the deterministic trend term θ_0 such that the mean of the simulated time series data is equal to the mean of the observed time series data.

Once the model structure is identified, the model parameters can be estimated by using one of parameter estimation tools. A diagnostic check is then made on the resulting model. This can be done by using the ACC and PACC of the residual¹ where both have to be within the critical limits for time lags different from zero. The values $\pm 2\sqrt{\text{var}[\hat{\rho}_k]}$ and $\pm 2\sqrt{\text{var}[\hat{\Phi}_{kk}]}$ can be used as critical limits on $\hat{\rho}_k$ and $\hat{\Phi}_{kk}$ of the residual to test the hypothesis that the residual is a white noise where

$$\text{var}[\hat{\rho}_k] \cong \frac{1}{N} \left\{ 1 + 2 \sum_{v=1}^q \rho_v^2 \right\}, k > q \quad (2.20)$$

and

$$\text{var}[\hat{\Phi}_{kk}] \cong \frac{1}{N} \quad (2.21)$$

$\text{var}[\hat{\rho}_k]$ and $\text{var}[\hat{\Phi}_{kk}]$ are the variance of the estimated ACC and PACC of the time series data respectively [59], [60].

Verification and final diagnostic checking

To justify that the identified model is the right model, it has to pass a final diagnostic check. The final diagnostic check involves comparing the simulated time series data against the measurement. The relevant parameters to be compared at this stage are the mean, variance, time correlation and probability distribution of the simulated and the measured time series data. If the simulation is not as good as the measurement, the deterministic trend term, transformation factors and/or the identified model structure need to be updated until the comparison of the simulated time series data against the measurement is acceptable.

Figure 2.12 shows the flow chart of the standard ARIMA based modelling procedure. The procedure starts by taking time series data as an input, which for instance can be wind speed. Then non-linear transformation followed by linear transformation is applied on the data (when necessary) to transform it into stationary time series data. Following this, the initial model identification is made for the transformed data which is followed by model parameter estimation. The first stage of diagnostic checking is made on the identified model. If the model is not ok, the model structure is updated using the information from the diagnostic checking and a new parameter estimation is made. The same process is repeated until the model is justified by the diagnostic checking.

¹ The residual is the value of $a(t)$ in (2.13) for a given time series data $y(t)$ and the estimated model parameters. In an ARMA based model, the residual is assumed to be a white noise. After the model is identified, if the residual is found out not to be a white noise, the initially identified model need to be updated since the assumption that the residual is a white noise is no longer valid.

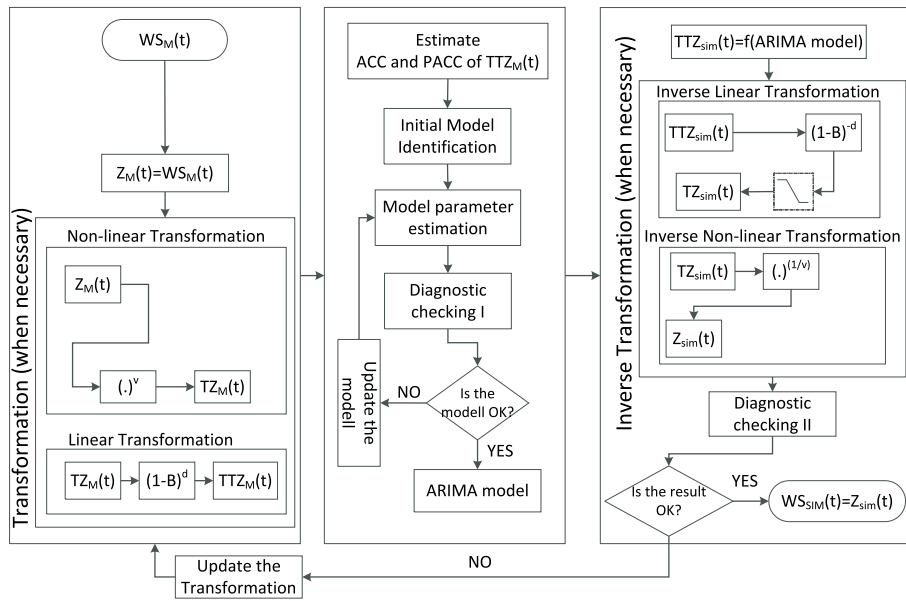


Figure 2.12: A flow chart of the standard LARIMA modelling procedure

If the model is ok, it is used to simulate time series data. Due to the possible presence of an integrator in the model (originated from differencing), the simulated data can be out of an acceptable range. Hence, a limiter is used to limit the simulated data within a limit. The resulting ARIMA model with a limiter is then termed as Limited ARIMA, which is abbreviated LARIMA(p, d, q), the idea of which is proposed in [49]. The resulting time series data are inverse transformed to get the desired simulation result. The final diagnostic checking is made on the simulated time series data by comparing the simulated time series data against the measurement on the basis of the mean, variance, probability distribution and time correlation. If the comparison does not result in a good match, the process is repeated with updated values of transformation parameters and model structures until acceptable results are achieved.

2.3.2 Standard Multivariate ARIMA model

Recall that an important characteristics of wind speed time series data is that there exists a strong correlation in time between the data. In addition to this, in a given geographical location, there could be a correlation of the wind speed data in space due to a similar wind condition. Hence, a good wind speed model for a power system analysis not only captures the correlation in time, but also the correlation in space of the wind speed data from different sites is needed.

Limited studies were made on time and space correlated modelling of wind speed data. Among those studies is an artificial intelligence based approach which includes Neural Network and Fuzzy Logic modelling methods [61], [62]. The approaches are non-linear and are developed to improve forecasting accuracy at a given wind power plant site by using spacial correlation and measured data from nearby sites. This approach is more costly and complicated compared with the statistical approach to be used in a typical power

2.3. ARIMA based time series modelling procedure

system study which requires simultaneous time and space correlated wind speed data over large areas. Some studies are also made to model time and space correlated wind speed data using a statistical approach which included vector or multivariate ARIMA (VARIMA) based modelling methods. This method is a linear model and it can be used to simulate simultaneous time and space correlated wind speed over large areas, which makes this approach to be appropriate to be used in the power system studies over wide area.

The VARIMA modelling procedure is similar to the ARIMA modelling procedure. The difference in the VARIMA model is that instead of modelling a time series data at a single location, multiple time series data at different locations are modelled at the same time.

Recall that an auto-correlation of a wind speed data is the correlation of wind speeds in time. The theoretical autocorrelation coefficients of a random process is usually not know, but can be estimated from the observed time series data, $y(t)$ by using the sample autocorrelation coefficient. The sample autocorrelation coefficient at time lag k is calculated by using (2.17). In addition, the cross-correlation of the wind speed is the correlation of the wind speed from multiple sites which are geographically distributed in space. Assume that there are n wind speed sites and the observed time series data from each sites is denoted by $y(t) = [y_1(t), y_2(t), \dots, y_n(t)]^T$. The sample cross-covariance matrix at time lag k can be calculated as

$$\hat{\Gamma}_y(k) = \begin{bmatrix} \hat{\gamma}_{11}(k) & \hat{\gamma}_{12}(k) & \cdot & \cdot & \cdot & \hat{\gamma}_{1n}(k) \\ \hat{\gamma}_{21}(k) & \hat{\gamma}_{22}(k) & \cdot & \cdot & \cdot & \hat{\gamma}_{2n}(k) \\ \cdot & \cdot & \cdot & \cdot & \cdot & \cdot \\ \cdot & \cdot & \cdot & \cdot & \cdot & \cdot \\ \cdot & \cdot & \cdot & \cdot & \cdot & \cdot \\ \hat{\gamma}_{n1}(k) & \hat{\gamma}_{n2}(k) & \cdot & \cdot & \cdot & \hat{\gamma}_{nn}(k) \end{bmatrix} \quad (2.22)$$

where the sample cross-covariance, $\hat{\gamma}_{ij}$, of the wind speeds between wind site i and j at time lag k is calculated as

$$\hat{\gamma}_{ij}(k) = \frac{1}{N-k} \sum_{t=1}^{N-k} (y_i(t) - \bar{y}_i)(y_j(t+k) - \bar{y}_j) \quad (2.23)$$

where \bar{y}_i and \bar{y}_j are the mean values of the sample data $y_i(t)$ and $y_j(t)$ respectively [60]. The corresponding sample CCC (cross-correlation coefficients) $\hat{\rho}_{ij}(k)$ can be calculated as

$$\hat{\rho}_{ij}(k) = \frac{\hat{\gamma}_{ij}(k)}{\sqrt{\hat{\gamma}_{ii}(0)\hat{\gamma}_{jj}(0)}} \quad (2.24)$$

For stationary processes $Y(t) = [Y_1(t), Y_2(t), \dots, Y_n(t)]^T$, the VARIMA model of order p and q (VARIMA($p, 0, q$)), is defined as

$$(I - \Phi_p B) Y(t) = \Theta_0 + (I - \Theta_q B) a(t) \quad (2.25)$$

where I is an $n \times n$ identity matrix; the AR coefficients $\Phi_p = \{\varphi_{ij}\}$ are $p \times p$ matrix where p is the order of the AR process and φ_{ij} are $n \times n$ estimated AR matrix coefficients ; the

MA coefficients $\Theta_q = \{\theta_{ij}\}$ are $q \times q$ matrix where q is the order of the MA process and θ_{ij} are $n \times n$ estimated MA matrix coefficients; Θ_0 is the deterministic trend term of an $n \times 1$ matrix and the multi-variate Gaussian white noise $a(t) = [a_1(t), a_2(t), \dots, a_n(t)]^T$ has a zero mean and an $n \times n$ covariance matrix, \sum_a [60]. Observe that the model in (2.25) does not have the integrating or the differencing term that appears in the ARIMA model. It is often tricky to use the integrating term in the VARIMA model and it is recommended not to use it as well since it does not help to get a better result [60]. Hence, the time space correlated data in VARIMA modelling are transformed by using only variance transformation factor, v , when needed.

Chapter 3

Building HVDC grid in the North Sea

In this chapter, different cases of HVDC transmission systems to be investigated in this thesis are presented. Figure 3.1 shows the main characteristics of the systems investigated in this thesis. It consists of an HVDC grid that acts as a hub to interconnect external AC grids and WPPs in the system.

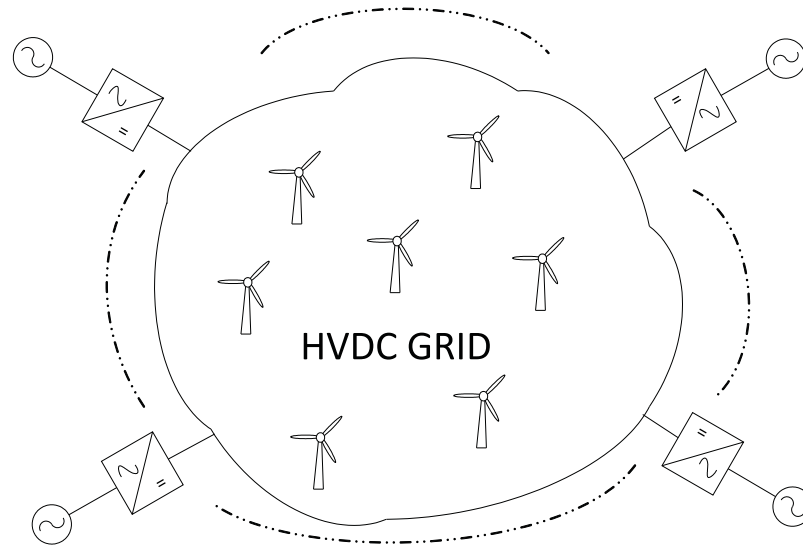


Figure 3.1: Elements of HVDC grid that acts as hub to interconnect external AC grids and WPPs

Recall that a meshed HVDC grid does not exist today and it is unlikely to build it at once. Recall also that, according to a work group in CIGRE, the future HVDC grid can be built in steps and the first step towards a fully meshed HVDC grid is a simple non-meshed configuration [20]. This development could naturally start from an inter-connector or from an offshore wind farm connection. Figure 3.2 shows the building of an HVDC grid from existing inter-connector. A WPP is added onto the inter-connector and then additional inter-connector is added on top of the resulting system. More inter-connectors and WPPs can be added onto this system to create a fully meshed HVDC grid with WPPs and interconnection with the external AC grids. In this thesis, it is assumed that similar development steps are expected in the building the HVDC grid in the North Sea region. Using this as a basis,

different cases in region are developed to be investigated in the following chapters of the thesis.

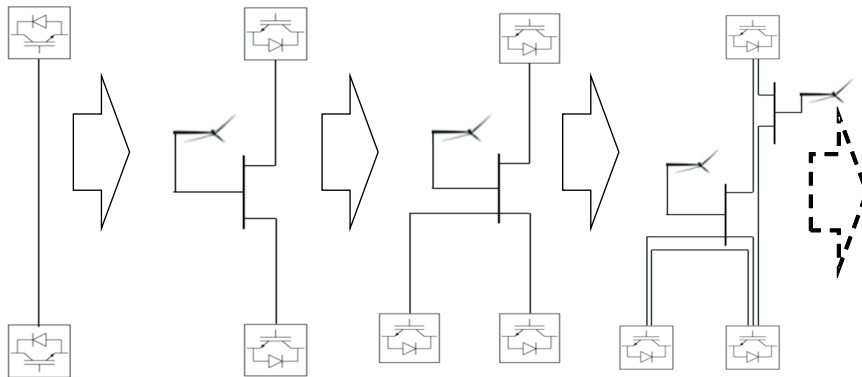


Figure 3.2: The steps toward building a HVDC transmission grid

3.1 Case 1: Two bus system, base case

Figure 3.3 shows a VSC based HVDC transmission link between Norway and the Netherlands which can be compared with the existing NorNed link. The NorNed link is 580 km long and is built using the classical CSC HVDC transmission technology [41]. Figure 3.3(a) shows the network diagram of the system and the length of the cable in this system is the same as the NorNed system where as the rating of the cable used in this system is different from that used in the NorNed system. The choice of the dimension of the cable used on in this system is based the measured exchange power data on the NorNed link during 2012. Figure 3.3(b) shows the annual duration curve of the exchange power

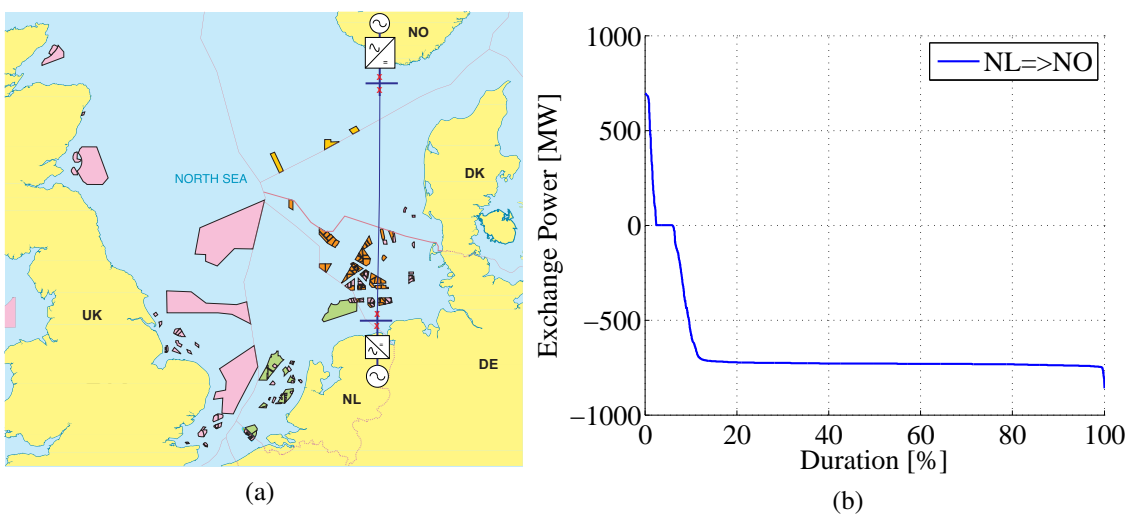


Figure 3.3: Data considered in Case 1 system (a) topology (b) annual duration curve of exchange power data

on the NorNed HVDC link during 2012, where the data is obtained from the NordPool

3.2. Case 2: Three bus system, with one WPP

spot. From Figure 3.3(b), it can be seen that for about 94% of the year, power flows from Norway to the Netherlands. For about 2.5% of the year, the power flows from the Netherlands to Norway and for the other 3.5% of the time, the transmission line is idle, with zero exchange power. Note also that the peak value of the power exchange during the year is about 860 MW. Taking this into account, the data presented in Table 3.1 are assumed to be used for this case study. Note that the technology considered for this study is VSC HVDC transmission technology and the corresponding cable data is taken from the list of cable technologies presented in Table 2.4. The cable is dimensioned based on the peak value of the exchange power and the suitable available cable technology in the data sheet. Observe that the sign xn is used in Table 2.4 and in the tables of all the other cases to indicate the number of parallel cables in a branch. Hence, the total rating of the branch is calculated by multiplying the numbers.

Table 3.1: Network dimensions the system defined in Case 1

From bus	To bus	Length (km)	Power(MW)	Area(mm^2)
NO	NL	580	943x1	1200x1

3.2 Case 2: Three bus system, with one WPP

In order to build Case 2, a WPP is connected to the inter-connector between Norway and the Netherlands which is defined in Case 1. Hence, the same exchange power profile and the same cable dimensions are used in this case. Figure 3.4 shows the network diagram of the system, where an offshore WPP is connected to the system.

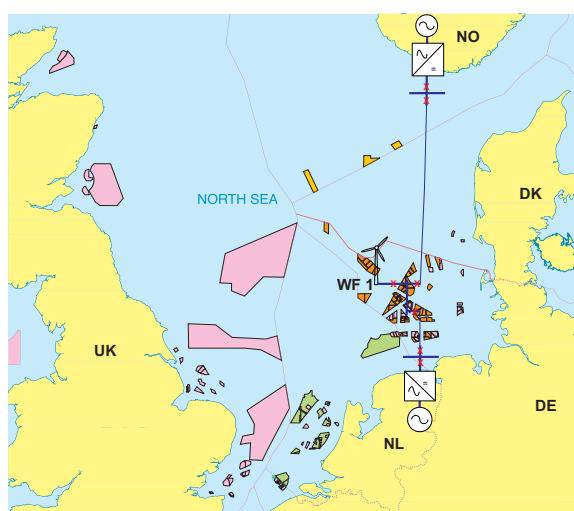


Figure 3.4: Topology of the system defined in Case 2 with a WPP

Table 3.2 shows the network dimension of the system in Case 2. Similar to case 1, the cable data are taken from the list cable technologies given in Table 2.4. The only difference between Case 2 and Case 1 is that Case 2 has one more bus where an offshore WPP is

connected. Note that, according to Figure 2.10, there is about 24 GW wind power capacity where the WPP in this case is located. Hence, to simulate this case, different percentages of the estimated wind power capacity is used which will be discussed in Chapter 5 and 6.

Table 3.2: Network dimensions the system defined in Case 2

From bus	To bus	Length (km)	Power(MW)	Area(mm^2)
NO	WF1	460	943x1	1200x1
NL	WF1	120	943x1	1200x1

3.3 Case 3: Six bus system, with three WPPs

Figure 3.5(a) shows the network diagram of the system defined in this case. It is a six bus system where four buses are connected to the external grids at locations in Norway, the Netherlands, Germany and Denmark, where the bus at Norway is assumed as a slack bus. The other two buses in the system are connected two offshore WPPs. Recall that in Figure 2.9, the annual duration curves of the exchange power profiles between Norway and Denmark, Norway and the Netherlands and Denmark and Germany are given. The exchange power profiles in this case is estimated based on the existing exchange data. Hence, the exchange power between Germany and the grid is considered to be the sum of the power exchanges between Denmark and Germany. The power exchange between Denmark and the grid is considered to be the sum of the power exchanges between Denmark, Germany and Norway. Similarly, the power exchange between the Netherlands and the grid considered to be the power exchange between Norway and the Netherlands. Since Norway is rich

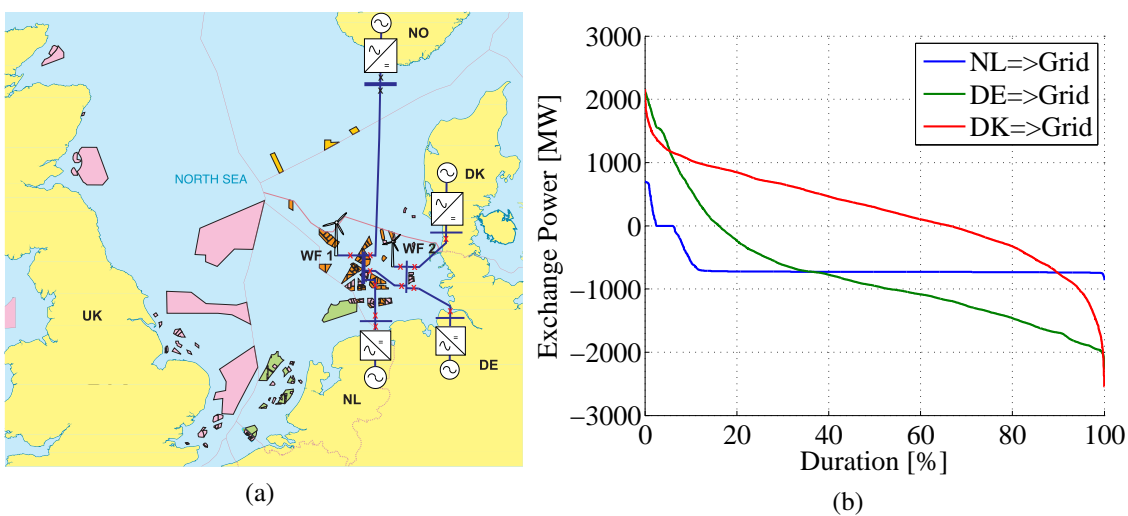


Figure 3.5: Data considered in Case 3 system (a) topology (b) annual duration curve of the estimated exchange power data

in hydro power, it is considered as a balancing bus or a slack bus in all the cases considered

3.4. Case 4: Nine bus system, with four WPPs

in this study. The annual duration curves of the assumed exchange power profiles between the grid and the external buses are shown in Figure (b). Note that there are two WPPs in Figure 3.5(a) and the geographical locations of the wind power plants are approximated and the corresponding time and space correlated wind speed data and hence wind power data can be determined for given WPP capacities, as described in Section 2.3 . Similar to Case 2, different capacities of WPPs will be considered during the simulation in Chapter 5 and Chapter 6.

Table 3.3 shows the dimension of the system defined in Case 3. The rating of the cables are dimensioned in such away the system can transport the exchange power profiles presented in Figure 3.5(b).

Table 3.3: Network dimensions the system defined in Case 3

From bus	To bus	Length (km)	Power(MW)	Area(mm ²)
NO	WF1	460	943x2	1200x2
NL	WF1	120	943x1	1200x1
DE	WF2	100	1190x2	1800x2
DK	WF2	70	1335x2	2200x2
WF1	WF2	80	1117x1	1600x1

3.4 Case 4: Nine bus system, with four WPPs

Figure 3.6(a) shows the network diagram of the system defined in this case. It is a nine bus system where five buses are connected to the external grids located in areas in Norway, the Netherlands, Germany, Denmark and UK. The other four buses are connected to offshore WPPs. The power exchange data in this case is estimated based on the power

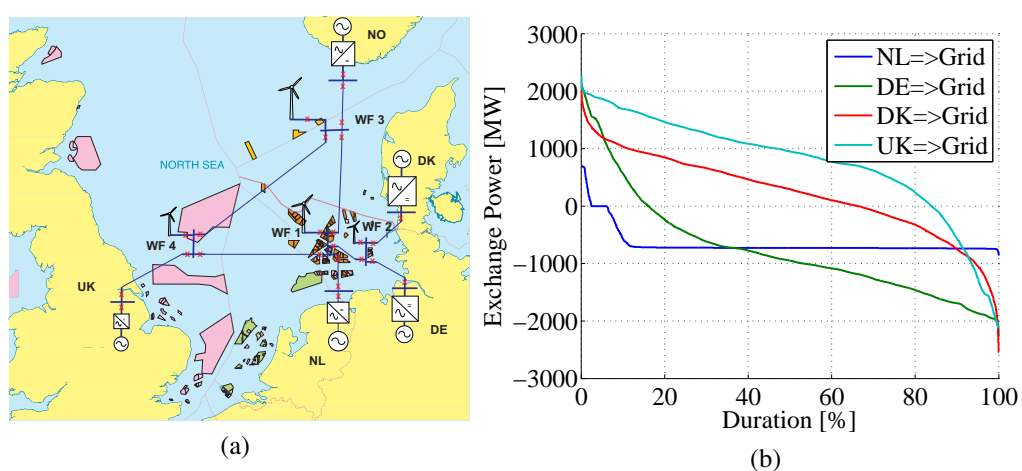


Figure 3.6: Data considered in Case 4 system (a) topology (b) annual duration curve of the estimated exchange power data

exchange data established in Case 3. Recall that, in Case 3 the power exchange data from the Netherlands to the grid, from Germany to the grid and Denmark to the grid are all estimated where as the exchange power data at Norway is determined based on the other power exchange data. To the author’s knowledge, similar power exchange data from UK to some neighbouring country in the region is not available. Hence, the power exchange data from UK to the grid defined in Case 4 is determined by taking the sum of the power exchange data from Norway, Denmark, Germany and the Netherlands to the grid which can be determined from the power exchange considered in Case 3. Figure 3.6(b) shows the estimated exchange power profiles between the grid and the surrounding countries. Note also that there are four WPPs in this system and the corresponding wind power from the WPPs can be determined from the WPP capacities and wind speed data at each WPPs, which will be considered in Chapter 5 and Chapter 6

Table 3.4 shows the estimated network dimensions of the system defined in Case 4. The length of the network cables are estimated based on known distances. The ratings of the cables are dimensioned so that the grid can transport the estimated exchange data presented in Figure 3.6b.

Table 3.4: Network dimensions the system defined in Case 4

From bus	To bus	Length (km)	Power(MW)	Area(mm^2)
NO	WF3	130	867x4	1000x4
NL	WF1	120	1033x1	1400x1
DE	WF2	100	1117x2	1600x2
DK	WF2	70	1117x2	1600x2
UK	WF4	200	1190x2	1800x2
WF1	WF2	80	1117x1	1600x1
WF1	WF3	330	1033x1	1400x1
WF1	WF4	300	1407x1	2400x1
WF3	WF4	400	867x2	1000x2

Chapter 4

Time and space correlated wind speed modelling for wind power simulation

As discussed in Section 2.3, ARIMA based wind speed model can be used to simulate time and space correlated wind speed from which the corresponding wind power can be determined. ARIMA based wind speed models developed so far require measurement data over many years to develop a wind speed model [47], [63]. For example, reference [47] used a three year hourly wind speed data and an hourly mean and standard deviation of the wind speeds from a 37-year data base to develop the corresponding ARIMA based wind speed model. The studies made in [48] and [55] are based on the wind speed model developed in [47]. In practice, it is often difficult to get this kind of data in places of interest. In addition, there us a standard ARIMA based modelling procedure used to model any kind of time series data [59], [60]. To the authors knowledge, the application of the ARIMA based modelling procedure for wind speed modelling is hardly found in the literature. Moreover, it is also observed that the methods adapted in the reviewed literature and the standard ARIMA based time series modelling procedure could not be used to model a 10 minute average wind speed time series data.

Hence, in this chapter three main contributions are made. First, the modified standard ARIMA based modelling procedure is presented. The modified ARIMA modelling procedure can be used to model wind speed time series data with high sampling frequency (10 minute average and lower). Second, the application of the proposed modelling procedure for the simulation of time series wind speed in the Baltic sea area is presented. Moreover, a generic model that can be sued to simulate time series wind speed in the area, for a given average wind speed, is also presented. Third, the application of vector ARIMA model to simulate time and space correlated wind speed in the North Sea is also presented.

4.1 ARIMA based time correlated wind speed model

4.1.1 Measured wind speed time series data

In this section, an ARIMA based model is developed for a given wind speed time series data by using the modelling procedure presented in Section 2.3. Figure 4.1 is a wind speed time series data from Näsudden peninsula in the Baltic sea and it is a 10 minute average data taken during 1st of January to 31st of December 2005 measured at a height of 120 m. In Figure 4.1(a) the wind speed during the year and in Figure 4.1(b) the wind speed during the first month of the year are presented. As can be seen from Figure 4.1, the measured wind speed data is highly non-stationary (both in mean and variance).

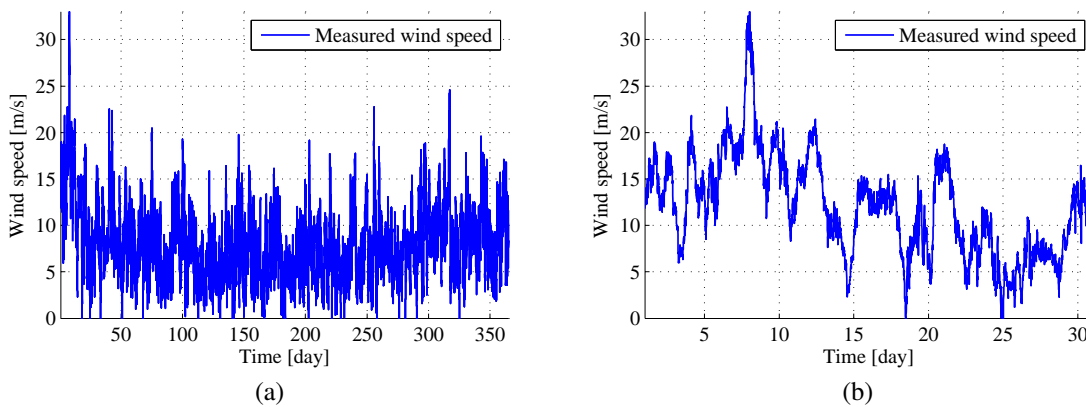


Figure 4.1: Measured wind speed (10 minute average data) (a) Over a year (b) Over the first month of the year

The non-stationary characteristics of the data can also be seen from the ACC and PACC of the data, as shown in Figure 4.2 where the solid line shows the ACC and PACC of the wind speed data calculated using (2.17) and (2.18) and the dashed lines show the critical limits calculated using (2.20) and (2.21).

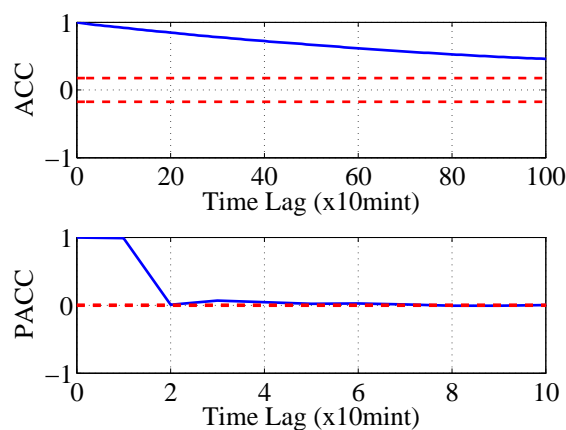


Figure 4.2: ACC and PACC of the measured wind speed data

Note that the ACC of the measured wind speed data in Figure 4.2 does not quickly come within the critical limits, (during the first few lag) indicating that the observed wind speed data could be originated from a non-stationary process demanding the application of an appropriate transformation on the data.

4.1.2 Transformation of wind speed data

Table 4.1 shows some values of the transformation factors, v , the corresponding transformation and the residual sum of squares of the time series. From the table, it can be seen that the transformation factor $v = 0.5$, i.e. the square-root transformation results in the minimum residual sum of squares.

Table 4.1: Box-Cox Power Transformation and Logarithm of the residual sum of squares of the time series wind speed data

Transformation factor (v)	Transformation	$\lg(SS(v))$
-2	$y(t)^{-2}$	16.1604
-1	$y(t)^{-1}$	14.1791
-0.5	$(\sqrt{y(t)})^{-1}$	13.7081
0	$\lg(y(t))$	13.4937
0.5	$\sqrt{y(t)}$	13.4682
1	$y(t)$	13.5948
2	$y(t)^2$	14.2430

After applying the square-root transformation to stabilize the variance followed by one degree of differencing to stabilize the mean, the resulting transformed data is presented as in Figure 4.3. Figure 4.3(a) shows the transformed wind speed data which looks stationary

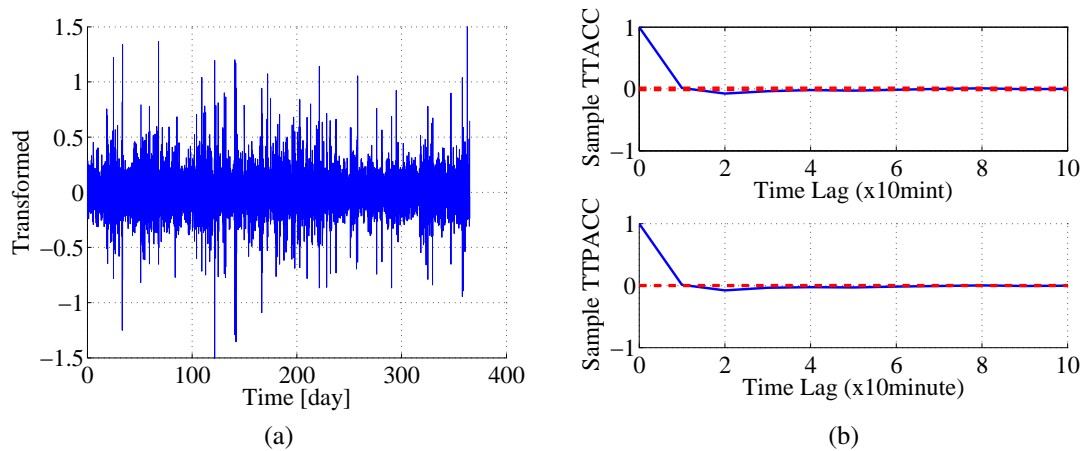


Figure 4.3: Transformed time series data (a) and ACC and PACC of the transformed time series data (b)

both in mean and variance. Figure 4.3(b) shows the ACC and PACC of the transformed

time series data, where both the ACC and PACC of the transformed time series damps down in the first few lags reflecting the characteristics of a stationary time series data as discussed in [59], [60].

4.1.3 Model identification and diagnostic checking

Comparing the ACC and PACC of the transformed time series data in Figure 4.3(b) with the theoretical ACC and PACC discussed in [59], [60], it seems that the underlying structure of the $ARIMA(p, d, q)$ could be $ARIMA(1, 1, 1)$. The presence of an integrator (originated from differencing) in the $ARIMA(1, 1, 1)$ model can result in unreasonably high and/or low wind speed values. Hence, a limiter is used before the integrator to limit the simulated wind speed within an acceptable range, which can also be seen in Figure 2.12. The resulting ARIMA model with the limiter is referred to as $LARIMA(1, 1, 1)$.

Figure 4.4 is a plot of the ACC, PACC and PDF (Probability Density Function) of the residual. Figure 4.4(a) shows the probability distribution of the residual. Figure 4.4(b) shows the ACC and PACC of the residual. Note that the ACC and PACC of the residual in Figure 4.4(b) is not bounded within the critical limit that occurs mainly at a lower time lag.

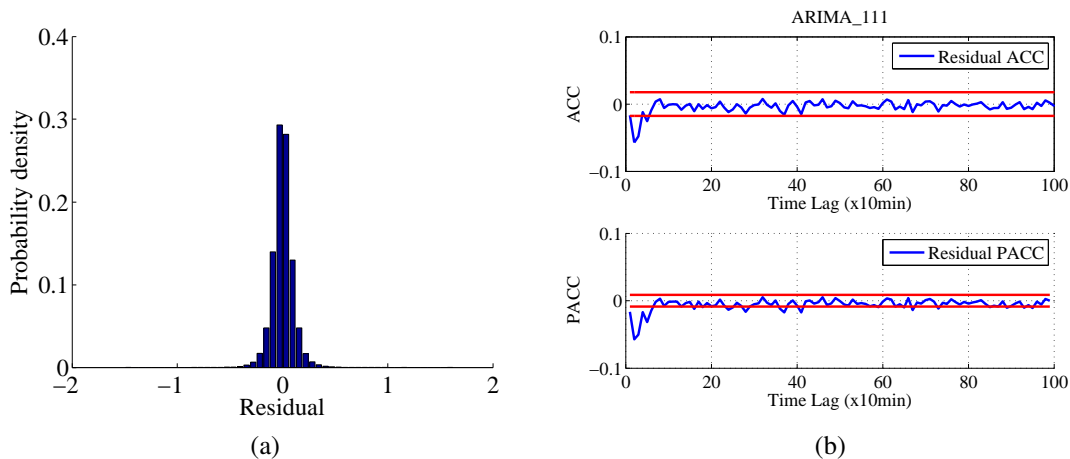


Figure 4.4: $LARIMA(1,1,1)$ (a) Residual PDF (b) Residual ACC and PACC

Comparing the ACC and PACC of the residual to the theoretical values in [59], [60], it seems that the residual itself is an $ARIMA(1,0,1)$ process. Hence, this information is used to modify the initially identified model, $LARIMA(1,1,1)$. The resulting updated model becomes $LARIMA(2,1,2)$. Figure 4.5 shows the ACC, PACC and PDF of the residual from the $LARIMA(2,1,2)$ model.

As can be seen from Figure 4.5, the ACC and PACC of the residual do not show any obvious pattern and are generally within the critical limits. Similarly, the probability distribution of the residual shows that the residual is normally distributed with a mean value of zero. Hence, the white noise assumption of the residual for $LARIMA(2,1,2)$ is valid.

Figure 4.6 shows the ACC and PACC of the transformed measured and simulated wind speed time series data. It shows a good match between the simulation and measurement.

4.1. ARIMA based time correlated wind speed model

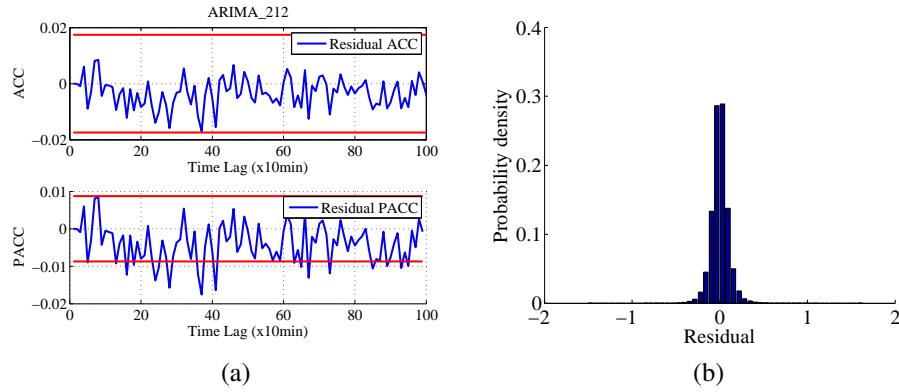


Figure 4.5: LARIMA(2,1,2) (a) Residual ACC and PACC (b) Residual PDF

However, checking the white noise assumption of the residual and the match in the ACC and PACC of the transformed time series data is not a sufficient condition to suggest that the identified model is the right model. Further analysis need be made on the simulated time series data to justify the adequacy of the identified model.

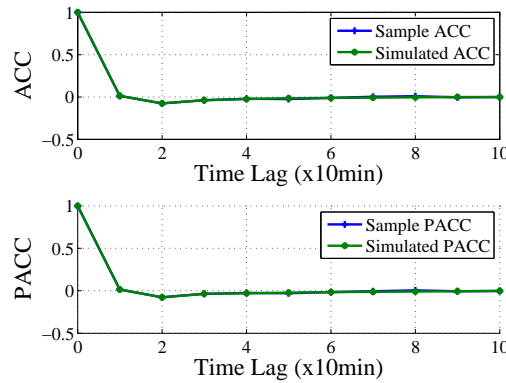


Figure 4.6: ACC and PACC of the transformed measured wind speed data

4.1.4 Verification and final diagnostic checking

Note that the measured wind speed data has a mean value of 8.01 m/s and a variance of $15.26 \text{ m}^2/\text{s}^2$. While the mean value of the simulated wind speed is the same as the measurement, the variance of the simulated wind speed is much larger than the measured value, $78 \text{ m}^2/\text{s}^2$. This large deviation in variance is reflected in the probability distribution plots as can be seen in Figure 4.7. Figure 4.7(a) shows the cumulative probability distribution of the measured and simulated wind speed time series data. Figure 4.7(b) shows the Q-Q¹ plot of the measured and simulated wind speed time series.

As observed in Figure 4.5, Figure 4.6 and Figure 4.7, while the assumption of a white noise is valid and there is a good match in ACC and PACC of the transformed measured

¹Q-Q (Quantile-Quantile) plot is a graphical method of comparing two probability distribution. If the two distribution being compared are similar, the Q-Q plot lies on the straight line ($y=x$)

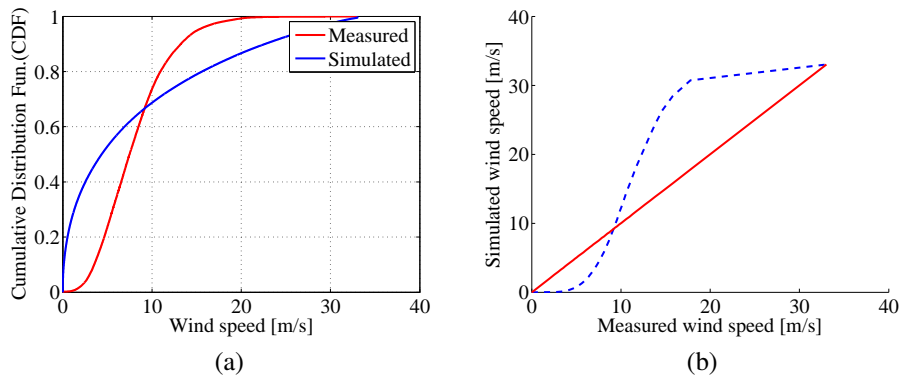


Figure 4.7: LARIMA(2,1,2), (a) Cumulative Distribution Function (CDF) (b) Q-Q plot of the measured and simulated wind speed

and simulated wind speed; the deviation in the probability distribution of the simulated and measured wind speed is significant. This deviation is associated with the deviation in variances, which is closely related to the variance transformation, presented in Table 4.1.

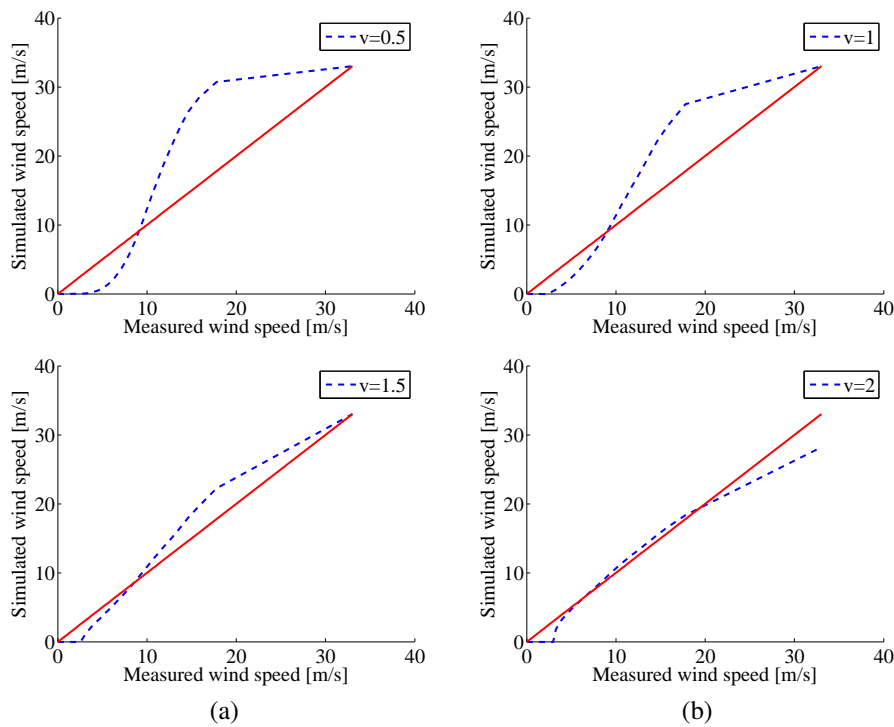


Figure 4.8: LARIMA(2,1,2) Q-Q plot of the measured and simulated wind speed (a) for $v=0.5$ and for $v=1.5$ (b) for $v=1$ and for $v=2$

Note that, the logarithms of the residual sums of squares of the time series presented in Table 4.1 are somehow closer to each other. Due to the non-stationary nature of the observed wind speed time series data, there might be a different value of v that can result in a better result although the logarithm of the residual sum of squares is not the smallest. Figure 4.8 shows the sensitivity of the model to the variance transformation factor, v ,

expressed in terms of the Q-Q plots.

The sensitivity analysis showed that the variance transformation factor $v = 2$ resulted in a better match in the Q-Q plot of the measured and simulated wind speeds, although it has a relatively higher residual sum of squares, as shown in Table 4.1. Figure 4.9 shows the comparison in time correlation of the measured (+) and the simulated (*) wind speed data when $v = 2$, indicating a clear mismatch between the simulation and measurement.

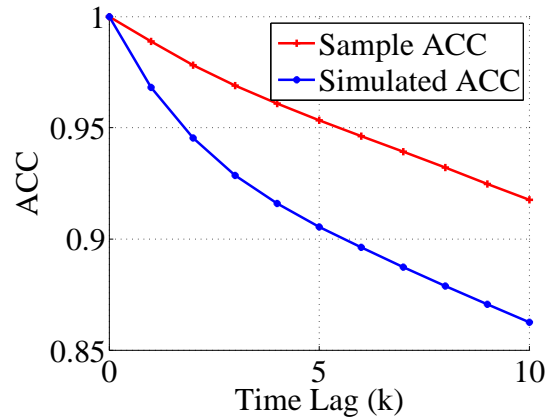


Figure 4.9: ACC of the measured and simulated wind speed data

Following the standard ARIMA based modelling procedure, all possibilities have been investigated to improve the simulation result. The model structure LARIMA(2,1,2) with a variance transformation $v = 2$ is found to be the 'best' as can be seen in Figure 4.8. The results indicate that the standard ARIMA based modelling procedure does not produce a simulated wind speed having a good match in both probability distribution and time correlation compared with the measurement for 10 minute average wind speed data considered in this paper. This requires a modification of the standard ARIMA based modelling procedure to produce a good simulation result. The modified ARIMA based modelling procedure, which is one of the contributions in this work, is discussed in the following sections.

4.2 Modified ARIMA based modelling procedure

4.2.1 Limiting the range of modelled wind speed

The mismatch in the Q-Q plots of the measured and the simulated wind speed, shown in the second row of Figure 4.8(b) at lower and higher wind speeds might be due the fact that the transformation factor does not produce a proportional weight at all wind speed ranges. In order to improve the result further, the sensitivity of the model to the range of the wind speed data is analysed. The results showed that by limiting the wind speed in the range of [2.5 , 26] m/s, the match in the measured and the simulated wind speed data can be improved greatly. Figure 4.10 shows some of the results generated from LARIMA(2,1,2) when the modelled wind speed is limited in the range of [2.5, 26] m/s. Note that the

variance of the simulated wind speed in this case is $14.19 \text{ m}^2/\text{s}^2$ compared with $14.72 \text{ m}^2/\text{s}^2$ for the limited measured wind speed.

The first row in Figure 4.10(a) shows the Q-Q plot and the second row shows the CDF of the measured and simulated wind speeds. The first row in Figure 4.10(b) shows the PDF of the measured and simulated wind speed and the second row shows the measured and simulated time series wind speeds.

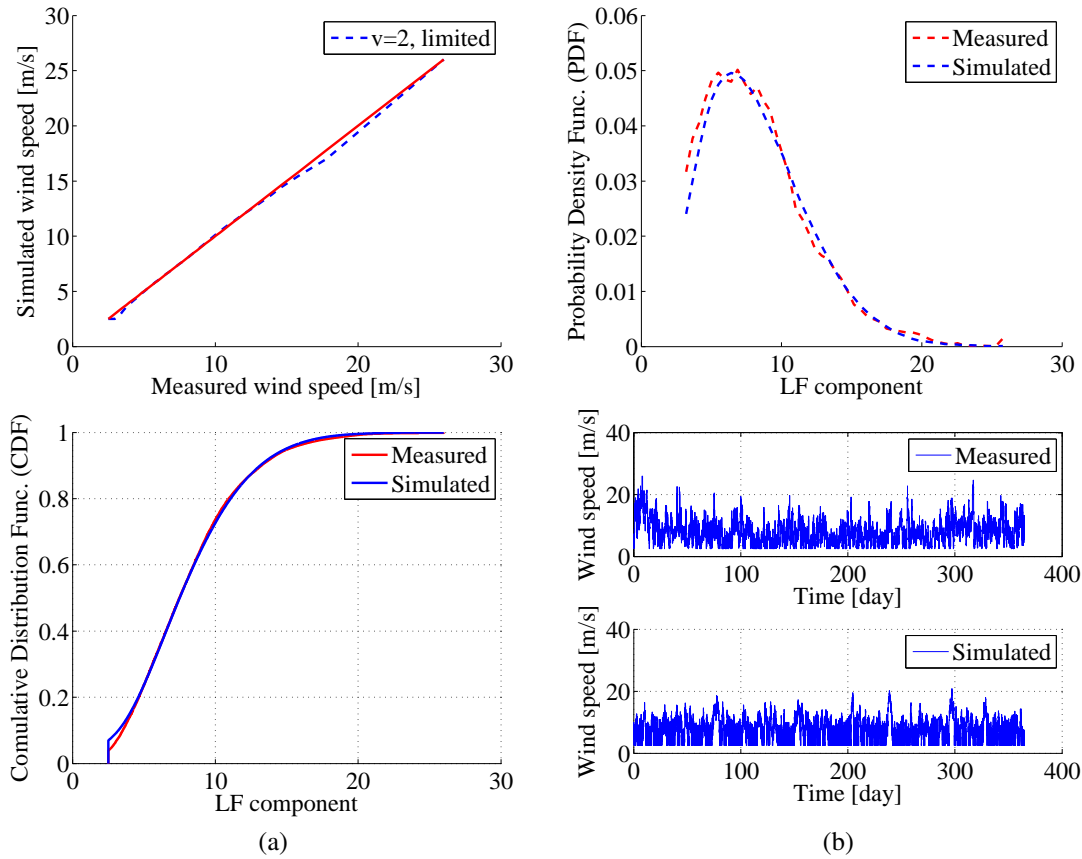


Figure 4.10: LARIMA(2,1,2) for a limited wind speed in the range [2.5, 26], (a) Q-Q plot and CDF plot (b) PDF and measured and simulated wind speed data

Comparing the measured and the simulated wind speed time series data in Figure 4.10(b), one can see that the periodic characteristics of the measured wind speed is poorly captured in the model. This can also be seen in Figure 4.11 which indicates that although there is a slight improvement in the simulated ACC, compared with the one in Figure 4.9, there is still a large deviation between the simulation and the measurement.

One way of looking at the different frequency components of a time series data is by using PSD (Power Spectral Density) of the data. Hence, in order to justify that all frequency (periodicity) components of the measured time series data are captured by the model, there has to be a good match in the PSD of the measured and the simulated time series data. According to [59] and [60], there is a direct relationship between the PSD and the ACC of a time series data. Hence, a good match in the ACC of the a series data imply that there is a good match in the PSD and hence a good match in periodicity of the measured and the

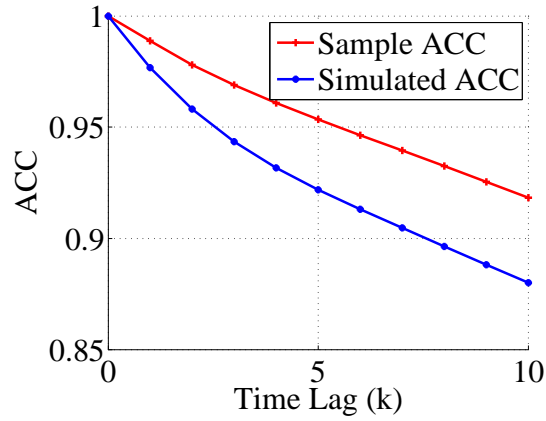


Figure 4.11: ACC of the measured and simulated wind speed data

simulated time series data. However, the mismatch in the measured and the simulated ACC in Figure 4.11 shows that the periodicity of the measured wind speed is poorly captured by the model. The investigation up to this point indicates an improved method is needed to capture time correlation, probability distribution and periodic characteristics of time wind speed data. In the following section, an improved ARIMA based wind speed modelling procedure based on the concept of frequency decomposition technique is introduced.

4.2.2 Frequency decomposition

The proposed, frequency decomposition based approach involves first splitting the wind speed data into HF and LF components. The LF and HF components of the wind speed are then modelled separately and the resulting time series data are combined to produce the final wind speed time series data where the periodic characteristics, time correlation and probability distribution of the measured wind speed data are captured in the model.

Determining the cut-off frequency

An important part of the proposed approach is to decide the cut-off frequency or cut-off period that divides the HF from LF components. As stated before, wind speed data has non-stationary characteristics. The major contributor to the non-stationarity of the wind speed is the LF component of the wind speed [64]. Hence, the HF component of the wind speed can be assumed as stationary. The cut-off period can then be chosen in such a way that the HF component is stationary.

For a time series data to be stationary, the ACC and PACC of the residual need to have the characteristics of a white noise for a large time lag; i.e. the ACC and PACC of the residual has to be within a critical limits which is calculated using (2.20) and (2.21). Figure 4.12 shows the ACC and PACC of the residual of the HF component of the wind speed with LARIMA(2,0,0) for different values of cut-off period along with the critical limiting values. Note that for $T_{cutoff} = 1day$, the residual ACC and PACC do not behave as a white

noise which indicates that the HF component at this cut-off frequency is not stationary. As the cut-off time increased from 1 day to 4 days, the ACC and PACC of the residual became closer and closer to the ACC and PACC of the white noise at a larger time lag. When $T_{cutoff} = 4day$, the ACC and PACC of the residual are within the limiting values for a larger time lags which indicates that the HF component at this cut-off time can be assumed stationary. It is important to notice at this point that the cut-off time (4 day) that emerged from this analysis is in line with the result from the Van der Hoven spectrum [64].

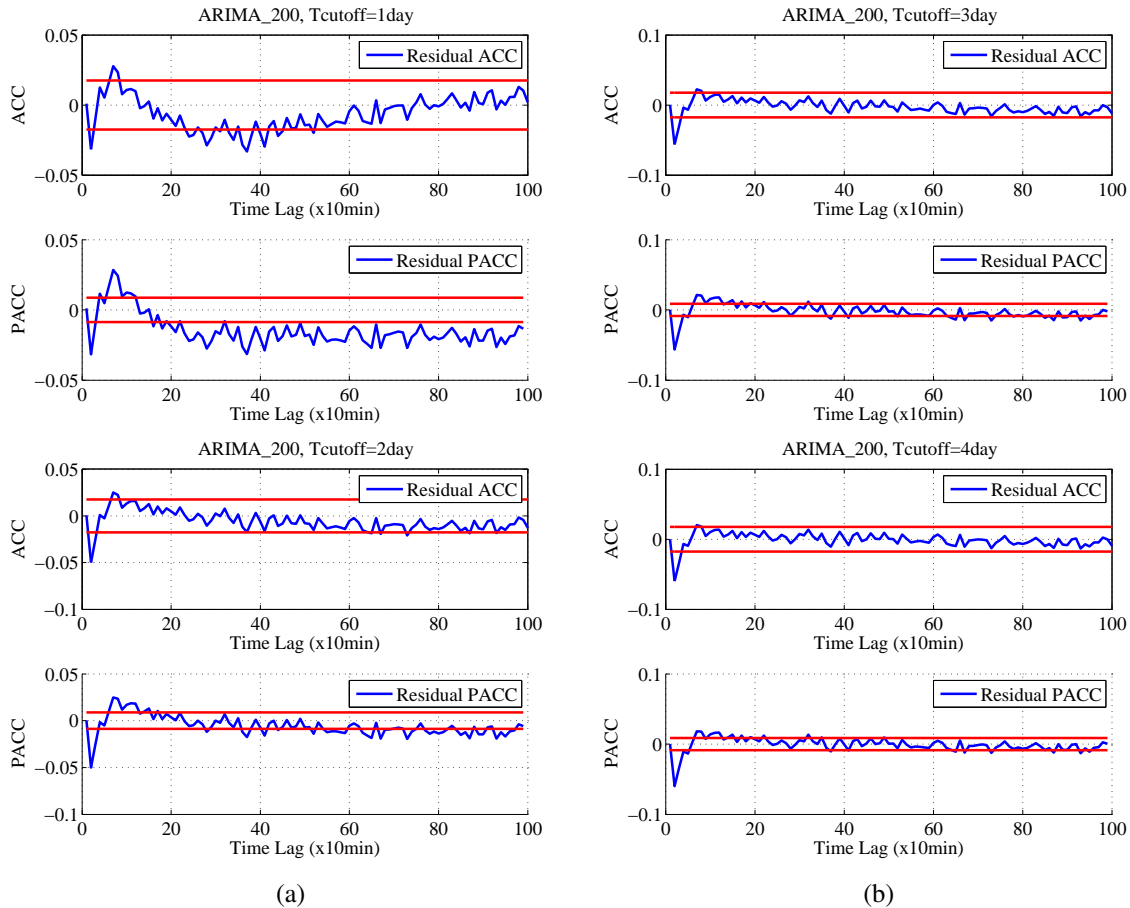


Figure 4.12: Residual ACC and PACC of the HF component of the measured wind speed with different values of the cut-off period ranging from 1 day to 4 days with LARIMA(2,0,0)

Modelling the HF component

Note that for $T_{cutoff} = 4day$, the residual ACC and PACC in Figure 4.12 at a lower time lag are not bounded within the limit. This indicates that the initially identified LARIMA(2,0,0) model for the HF component needs to be modified. Following the diagnostic checking procedure described in section (2.3.1), the updated model structure for the HF components of the wind speed is found to be LARIMA(6,0,0). Figure 4.13(a) shows the CDF plot of the HF components of the measured and simulated wind speed data showing a good match between the measurement and the simulation. Similarly, Figure 4.13(b) shows the ACC-PACC plot of the HF components. Both results in Figure 4.13 show the

sufficiency of the model structure, LARIMA(6,0,0), to capture characteristics of the HF components of the measured wind speed data.

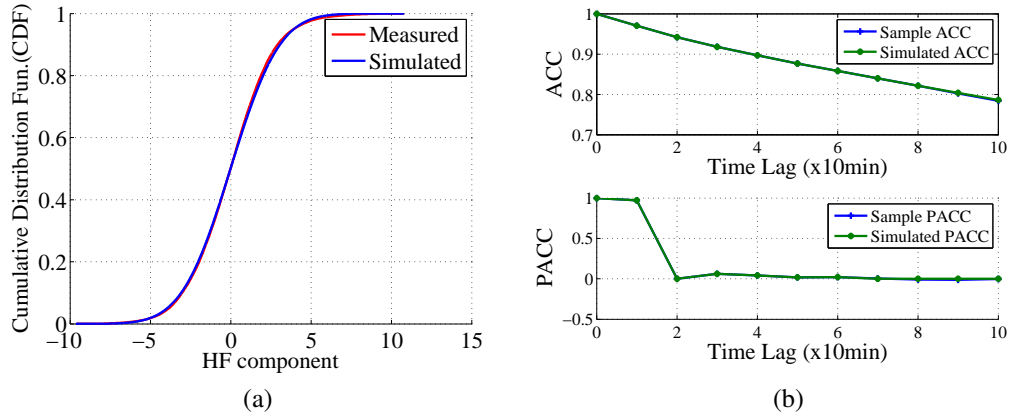


Figure 4.13: LARIMA(2,1,2), (a) cumulative probability distribution (b) Q-Q plot of the measured and simulated wind speed

Modelling the LF component

Once the stationary, HF, component of the wind speed is determined using the cut-off time, the LF component is obtained by subtracting the HF component from the original measured wind speed data. The resulting LF component is non-stationary and it can be modelled with a LARIMA model structure following the same design procedure as presented in Figure 2.12.

Before transforming the LF data, it is good to re-sample the data in order to make it suitable for modelling. Note that the sampling frequency of the measured wind speed is 144 samples per day, which is too high compared with the maximum frequency of the LF data ($f_{max} = 1/T_{cutoff}$) which is 0.25 cycle per day. This makes it difficult to see the temporal correlation of the data and hence the ACC and PACC of the data from which the initial model identification can be made.

To re-sample the LF component, sampling frequencies in the range of $[2 * f_{max}, 8 * f_{max}]$ are considered. According to the Nyquist sampling criteria, reconstruction of a signal is possible when the sampling frequency is greater than twice the maximum frequency of the signal being sampled. To see the effect of different re-sampling frequency on the CDF of the LF component of the data, $(2 * f_{max}, 4 * f_{max}, 6 * f_{max}, 8 * f_{max})$, are considered, which corresponds to one sample per two days, one sample per day, 3/2 samples per day and two samples per day respectively. Figure 4.14 shows the effect of different values of the re-sampling frequency on the CDF of the measured and the simulated LF time series data. From the analysis, it is observed that the sampling rate of $2 * f_{max}$ resulted in a relatively good result.

The re-sampled LF time series data is then transformed by using a transformation factor of $v = 0$ (logarithmic transformation) followed by one degree of differencing ($d =$

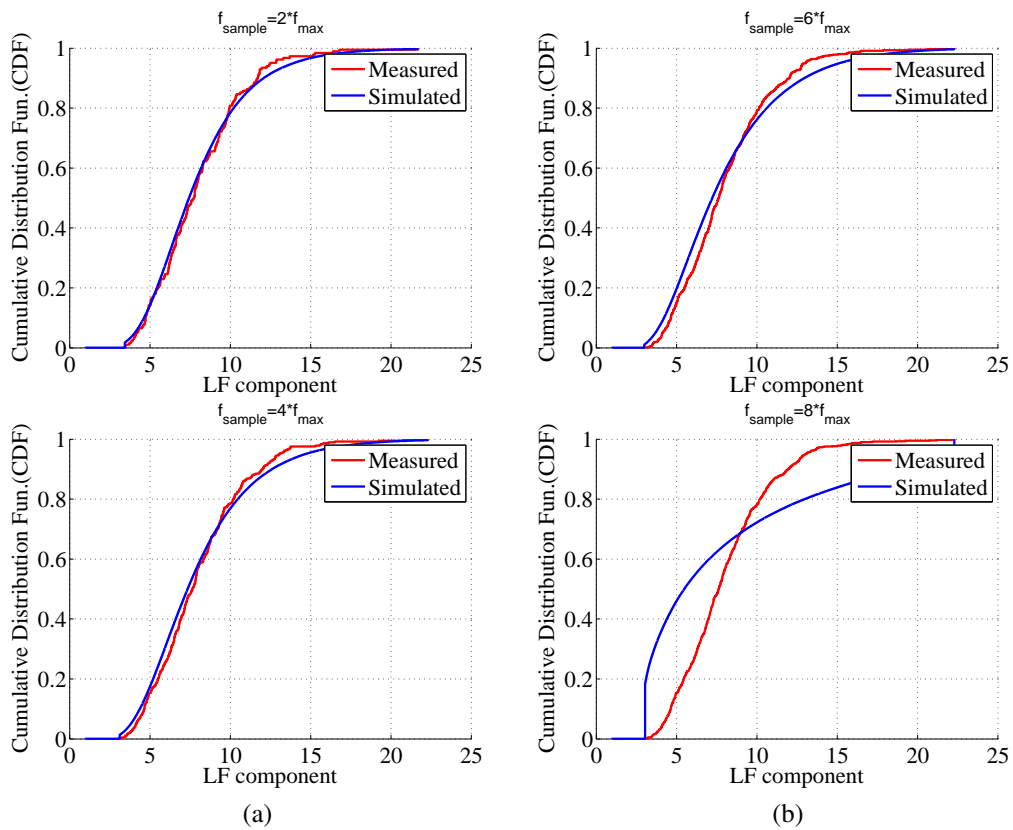


Figure 4.14: Effect of sampling frequency on the CDF plots of the LF component of the wind speed data

1). The resulting time series data is fit to a LARIMA(0,1,6) model structure. Figure 4.15

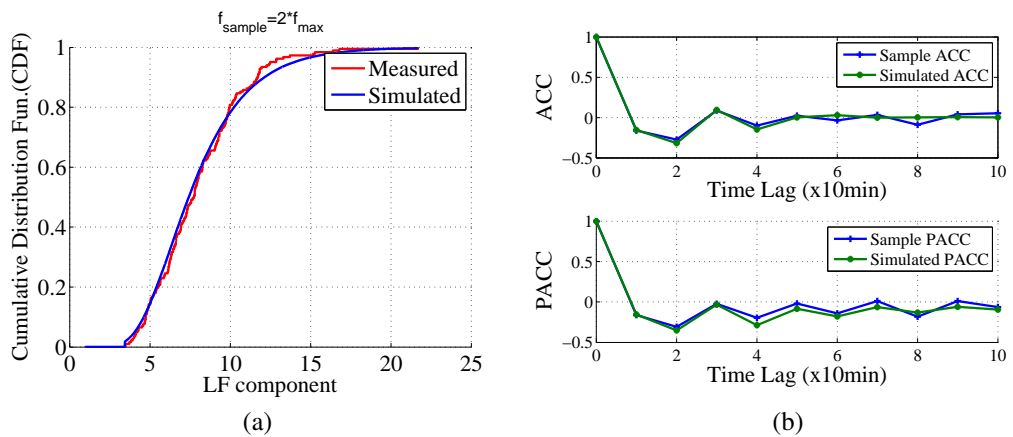


Figure 4.15: Results from LARIMA(0,1,6) for the low frequency components of the wind speed

shows some results from the LARIMA(0,1,6) model. Figure 4.15(a) shows the CDF plot of the LF component of the measured and the simulated wind speed. And Figure 4.15(b) shows the ACC and PACC of the LF components of the measured and the simulated wind speed. From these results one can see that the results in Figure 4.15 does not reach the

extreme fit as in Figure 4.13 but definitely good enough to capture the characteristics of the LF component of the wind speed data.

Combining the results from HF and LF Models to get the final result

Once the HF and LF components of the wind speed time series data are modelled separately, the last step is to combine the results from the two models to get the complete representation of the simulated wind speed data. Figure 4.16 shows some of the results of the combined model. Figure 4.16(a) shows the CDF of the measured and the simulated wind speed data showing a good match between the simulation and the measurement. Figure 4.16(b) shows the measured and the simulated wind speed time series data over a year.

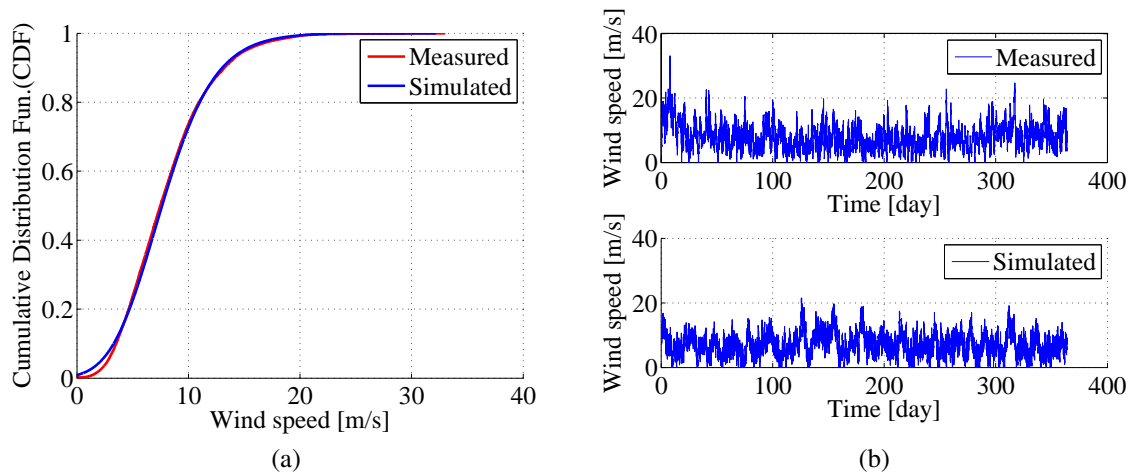


Figure 4.16: Measured (a) and simulation (b) results from the combined (HF + LF) wind speed model

Observe that qualitative comparisons of the measured and the simulated wind speed data show that the results are much more similar compared to the result presented in Figure 4.10. Note also that the simulated wind speed is generated using Monte Carlo simulation over a simulation period of 10 years. The simulated wind speed shown in Figure 4.16 is the data during the first one year of the simulation time. One important difference between the measured and simulated wind speed in Figure 4.16 is that the measured wind speed has a spike some time during the year while the simulated wind speed does not have these spikes. The spikes in the measured wind speed time series is a rare phenomena, it does not happen all the time. Hence, the simulated wind speed can have these spikes some times during the simulation time of 10 years.

Qualitatively speaking, the simulated and the measured wind speed data in Figure 4.16 look alike. The periodic characteristics of the measured wind speed is also captured well by the model. This can be supported quantitatively by using the ACC plot of the measured and the simulated wind speed data. Recall that a good match in the ACC of the measured and the simulated data implies a good match in the PSD which is a measure of periodicity.

Figure 4.17 shows the ACC of the measured and the simulated wind speed data indicating an excellent match compared with the one presented in Figure 4.11.

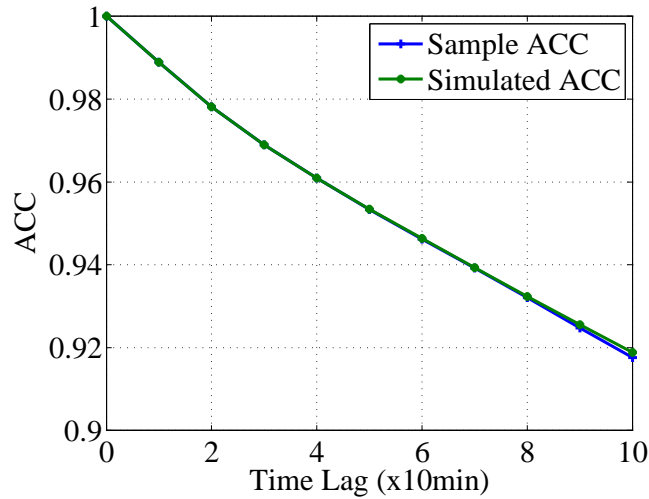


Figure 4.17: ACC of the measured and the simulated wind speed data resulting from the combined HF and LF components

4.2.3 Shifting the wind speed data (Adding a constant offset value to the signal)

Although not used in the modelling of the measured wind speed data presented in the preceding sections, shifting the measured time series data before the non-linear transformation can sometimes improve the quality of the model, as can be seen in Table 4.2 and 4.3 in Section 4.3.

4.2.4 Flow chart of the modified ARIMA based wind speed modelling procedure

The results presented in the preceding sections showed that the proposed modified ARIMA based modelling procedure can produce promising results. By combining the added control parameters introduced in the modified modelling procedure (limiting, frequency decomposition and shifting) with the parameters of the standard modelling procedure (variance transformation and differencing), much better results can be achieved. Figure 4.18 shows the flowchart of the modified ARIMA based modelling procedure. The procedure is similar to the standard procedure presented in Figure 4.18 except that it has the added model control parameters (limiting, frequency decomposition and shifting).

The modified ARIMA based modelling procedure presented in this paper is designed to be general. It can be used to develop an ARIMA based model of a given wind speed time series data that can capture time correlation, probability distribution and periodic characteristics of the given time series data. To support this claim, the modelling procedure is

4.3. Application of the proposed modelling procedure

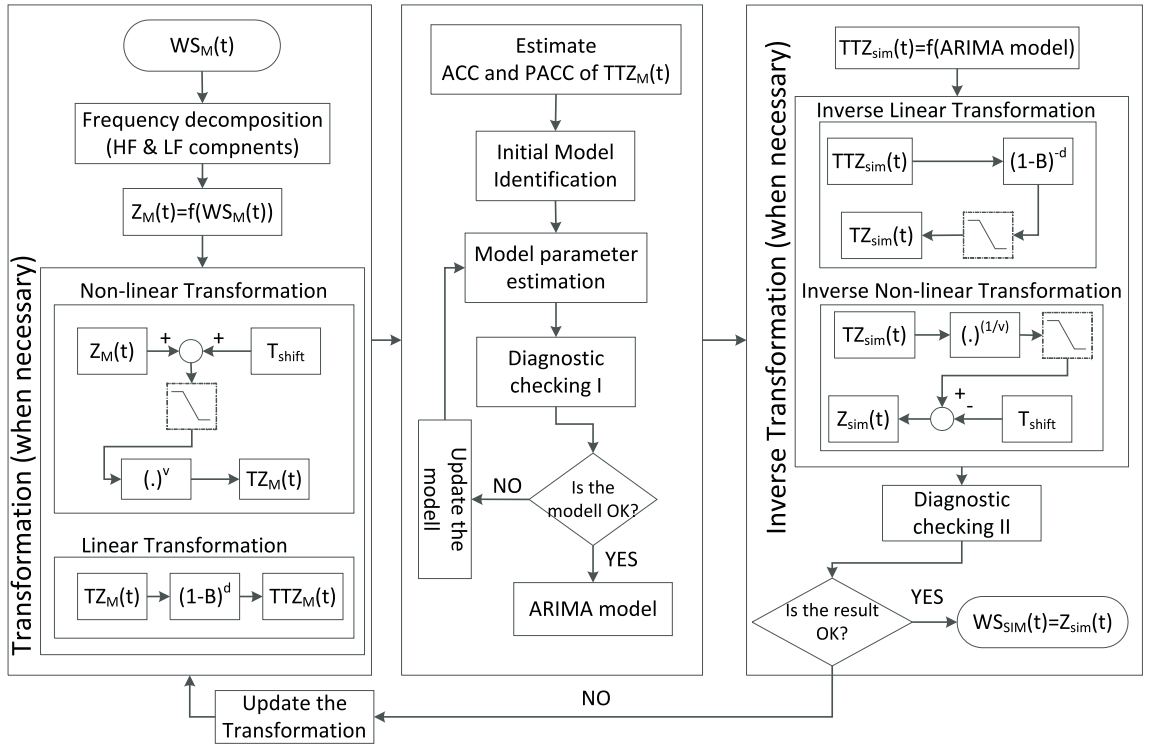


Figure 4.18: A flow chart of the modified ARIMA based modelling procedure

used to develop LARIMA models for wind speed data obtained from different geographical locations, as presented in the following section.

4.3 Application of the proposed modelling procedure

4.3.1 ARIMA(6,0,0) for HF and LARIMA(0,1,6) for LF component of wind speed

The proposed modelling procedure is tested using wind speed data from three different locations. Table 4.2 and 4.3 shows the model structure and model parameters of the HF and LF component of the wind speed from the three locations respectively. Data 1 in Table 4.2 and 4.3 represent measured wind speed data obtained from the Näsudden measurement site on the island of Gotland. Data 2 in both tables represent measured wind speed data from the Utgrunden measurement site close to the shore in the south east coast of Sweden and Data 3 represents measured wind speed data from 'Tjaereborg' in Denmark. The model parameters are developed based on 10 minute average wind speed data at each locations.

Since the proposed modelling procedure involves decomposing the wind speed, the same cut-off frequency or period ($T_{cutoff}=4\text{day}$) is used to split all the wind speed data into HF and LF components. Table 4.2 shows the model parameters of the HF components of the all wind speed data. It is observed that the HF components of all the wind speed data can be modelled with ARIMA(6,0,0) or simply AR(6) where a transformation factor

of $v = 1$ and degree of differencing, $d = 0$ is used. It is also observed that θ_0 and T_{shift} do not improve the result and hence both are set to zero in this case.

Table 4.2: Model parameters of the HF components of wind speed data from different locations. The model structure in each case is ARIMA(6,0,0)

Data source	Model Parameters
Data 1 HF component	$\theta_0 = -0.0001, T_{shift} = 0$ $\phi_1 = 0.9662, \phi_2 = -0.0571, \phi_3 = 0.0232$ $\phi_4 = 0.0245, \phi_5 = -0.0030, \phi_6 = 0.0210$
Data 2 HF component	$\theta_0 = -0.003, T_{shift} = 0$ $\phi_1 = 1.0350, \phi_2 = -0.1177, \phi_3 = 0.0352$ $\phi_4 = 0.0251, \phi_5 = 0.0058, \phi_6 = -0.0110$
Data 3 HF component	$\theta_0 = -0.001, T_{shift} = 0$ $\phi_1 = 0.9227, \phi_2 = -0.0648, \phi_3 = 0.0659$ $\phi_4 = 0.0143, \phi_5 = 0.0149, \phi_6 = 0.0159$

Table 4.3 shows the model parameters of the LF components of all wind speed data. Note that the lowest period in the LF component of the wind speed data is equal to the cut-off period ($T_{cutoff}=4\text{day}$) and for the 10 minute average data, the sampling frequency is $F_s = 6\text{samples/hour}$. This indicates that the LF component of the wind speed need to be re-sampled. As illustrated in Section 4.2.2, the re-sampling frequency is found to be $2 * F_{cutoff} / F_s$. It is observed that the re-sampling frequency is applicable for all the wind speed data. It is also observed that all the re-sampled LF components of the wind speed data can be modelled by LARIMA(0,1,6) or limited MA(6) where a transformation factor of $v = 0$ and degree of differencing, $d = 1$ are used. The limiter is used in this case due to the presence of an integrator in the model which results from the degree of differencing used. Finally, it is noted that θ_0 determines the average value of the simulated wind speed and the use of different values of T_{shift} can affect the result in a positive way.

Table 4.3: Model parameters of the LF components of wind speed data from different locations. The model structure in each case is LARIMA(0,1,6)

Data source	Model Parameters
Data 1 LF component	$\theta_0 = -0.0025, T_{shift} = 5$ $\theta_1 = 0.3258, \theta_2 = 0.5157, \theta_3 = -0.0890$ $\theta_4 = 0.1951, \theta_5 = -0.0132, \theta_6 = -0.0520$
Data 2 LF component	$\theta_0 = 0.0003, T_{shift} = 10$ $\theta_1 = 0.4008, \theta_2 = 0.5747, \phi_3 = 0.0352$ $\phi_4 = 0.0251, \phi_5 = 0.0058, \phi_6 = -0.0110$
Data 3 LF component	$\theta_0 = 0.00025, T_{shift} = 5$ $\theta_1 = 0.2029, \theta_2 = 0.7413, \theta_3 = -0.0986$ $\theta_4 = 0.2570, \theta_5 = -0.0433, \theta_6 = -0.2016$

From analysis made using the wind speed data at three locations, it is found out that the HF component of 10 minute average wind speed data can be modelled using ARIMA(6,0,0) or simply six order Auto Regressive model, AR(6). It is also found out that the LF component of 10 minute average wind speed can be modelled by LARIMA(0,1,6) or limited six

order Moving Average model with one degree of differencing, $d = 1$. The limiter is used in this case due to the presence of an integrator in the model which results from the degree of differencing used.

4.3.2 A model to simulate wind speed in the Baltic sea area

The wind speed models developed so far involves measurements. If one is interested in developing a wind speed model at a given location using a measured wind speed data over a certain period, the proposed modelling procedure could be used. If the measurements are 10 minute average data, one does not need to go through the modelling procedure; it is enough to fit the HF and LF component of the measured wind speed into ARIMA(6,0,0) and LARIMA(0,1,6) respectively. The resulting model can produce simulated wind speed data with a tight fit against the measurement in terms of time correlation and probability distribution.

However, wind speed measurements are not available at all places of interest. It is of great importance to develop a model that can produce simulated wind speed data with *acceptable* properties at places where there are no measured wind speed time series data. In order to get the kind of wind speed model and to define the term *acceptable*, it is important to study the variability of the model parameters and relevant properties of measured wind speed data from place to place and from time to time.

In order to study the variability of the model parameters (both HF and LF model parameters) as a function of location and time, the wind speed time series data from Näsudden and Utgrunden are investigated, which are located in the Baltic Sea region, North West Europe. Note that the wind speed models developed so far are based on measured wind speed data over one year. To see the variability of the model parameters from year to year, wind speed data over many years are considered in this study. The measurement data from Näsudden has 10 minute average wind speed over five year and the measurement data from Utgrunden has 10 minute average wind speed data over three years. The average wind speed at each location from year to year is shown in Table 4.4.

Table 4.4: Average wind speed at different location and different years

Average wind speed [m/s]	Näsudden	Utgrunden
All years	7.3116	7.4634
Year 1	6.6068	7.2836
Year 2	7.1334	7.787
Year 3	7.3203	7.4938
Year 4	7.9113	
Year 5	7.6855	

Figure 4.19 shows the model parameters of the different wind speed data from Näsudden. Figure 4.19(a) shows the parameters of the HF component and Figure 4.19(b) shows the parameters of the LF components. Note that there are similar patterns in the both HF and LF model parameters. For the HF components, the model parameters from year to

year are almost the same. However, there is a slight variation in model parameters of the LF components from year to year.

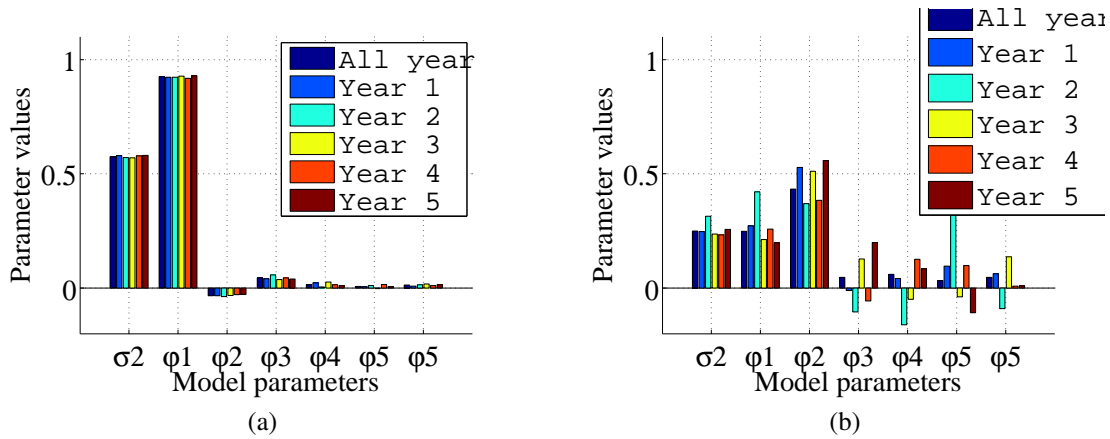


Figure 4.19: Annual variability of model parameters when wind speed measurements from different year are considered (a) HF component (b) LF component

Figure 4.20 shows the model parameters of the different wind speed data from Utgrunden. The pattern and the values of the model parameters in this case are similar to the one presented in Figure 4.19. Note that the model parameters of the LF component of the data from Utgrunden is more stable or uniform compared with the one from Näsudden. Similar result is observed when analysing wind speed time series data at Tjaereborg, which is close to the north sea. The result from Tjaereborg looks more like the result from Näsudden than the result from Utgrunden.

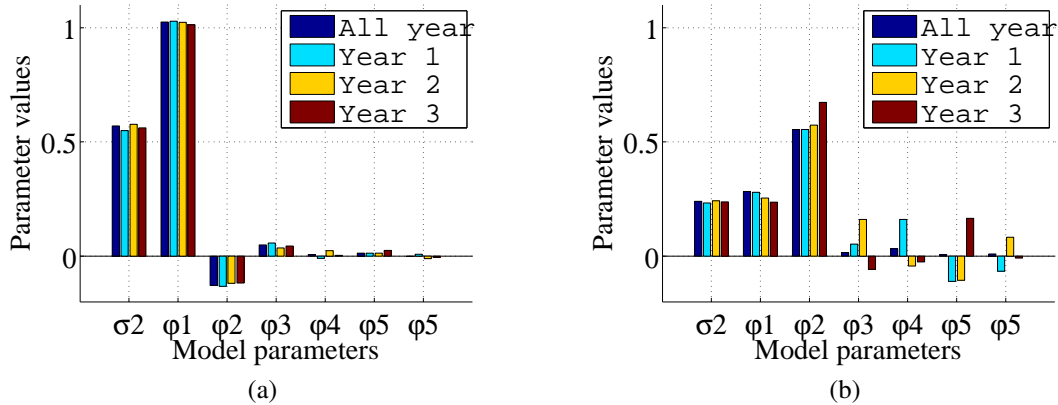


Figure 4.20: Annual variability of model parameters when wind speed measurements from different year are considered (a) HF component (b) LF component

It is worth pointing out two important points from the above results. The first point is that the model parameters, especially that of the HF component, are not much affected when measurement data being considered changes from year to year at a given location. The second point is that by comparing the model parameters at Näsudden and Utgrunden, it can be seen that there is a similar pattern in model parameters with a slight difference in

4.3. Application of the proposed modelling procedure

the magnitude of the model parameters. This is an interesting observation since it can be used to develop a wind speed model that can be used to simulate wind speed time series data at another location, particularly in the Baltic sea area and to some extent in areas close to the north sea. To establish this model, it is important to have a way to check how good this model is in simulating the wind speed data at the desired location with *acceptable* relevant properties. One way to establish acceptability of the model is to look at the annual variability of the relevant wind speed characteristics. If the model can produce a wind speed time series data at given location and the variability of the simulated wind speed compared with the measurement at the location is comparable with the annual variability of the relevant parameters at the location, the model can be taken as acceptable.

Figure 4.21 shows the variation of the relevant characteristics of the measured wind speed from year to year at Näsudden. Figure 4.21(a) shows the annual variation in ACC of the measured wind speed time series data. It is observed that the spread of the ACC curves in the figure are due to the different average wind speed from year to year. Figure 4.21(b) shows the annual variation in CDF of the measured wind speed time series data. This can be used as a basis to check if the simulated wind speed time series data at location using a given model is acceptable or not.

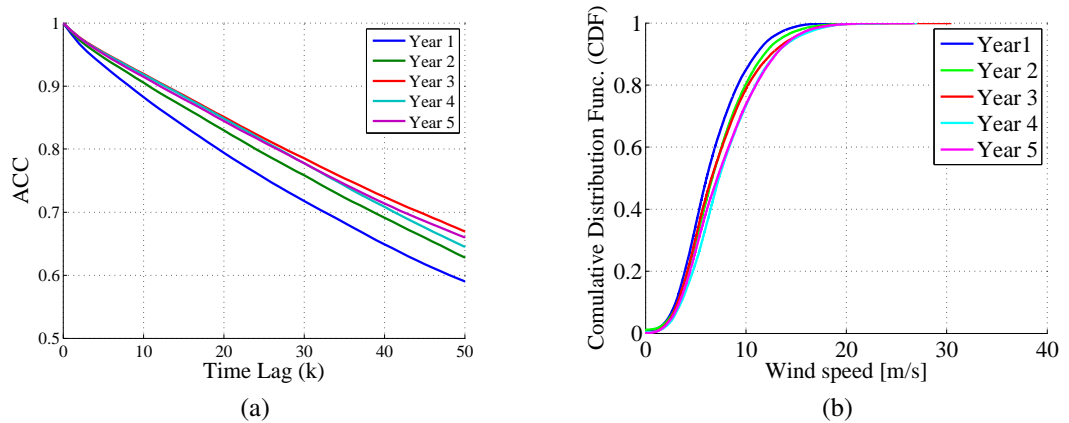


Figure 4.21: Annual variability of relevant characteristics of wind speed time series data (a) ACC (b) CDF

In order to show the possibility of simulating a wind speed time series data at a given location in the Baltic sea area using a generic model, the model parameters presented in Figure 4.20 (the model parameters developed at Utgrunden) is used to simulate the wind speed data at Näsudden. The actual values of the model parameters are given in Table 4.5 and Table 4.6. Model M1 stands for the model developed by using all year data at Utgrunden, similarly model M2 is associated with Year 1 data, M3 with Year 2 data and M4 with year 3 data.

Figure 4.22 shows the properties of the simulated wind speed data at Näsudden produced by using different models developed at Utgrunden, the parameters of which are shown in Table 4.5 and Table 4.6. Note that, to produce the results presented in Figure 4.22, T_{shift} and θ_0 in simulating the HF components is set to zero and θ_0 for HF component simulation is adjusted in such away that the average wind speeds presented in Table 4.4 are

achieved. Figure 4.22(a) shows the comparison of measured Year 1 data at Näsudden with the simulated data produced using different models from Utgrunden in terms of ACC and CDF. Similarly, Figure 4.22(b) shows of the comparison of the ACC and CDF of the measured, Year 2, wind speed data at Näsudden and the corresponding simulated wind speed data generated with different models. The same model is used to simulate wind speed time series at Tjaereborg in Denmark and similar result is obtained. It is observed that the CDF of the simulated wind speed at Tjaereborg has less deviation from the measurement where as its ACC has larger deviation compared with the simulated wind speed at Näsudden using the same model.

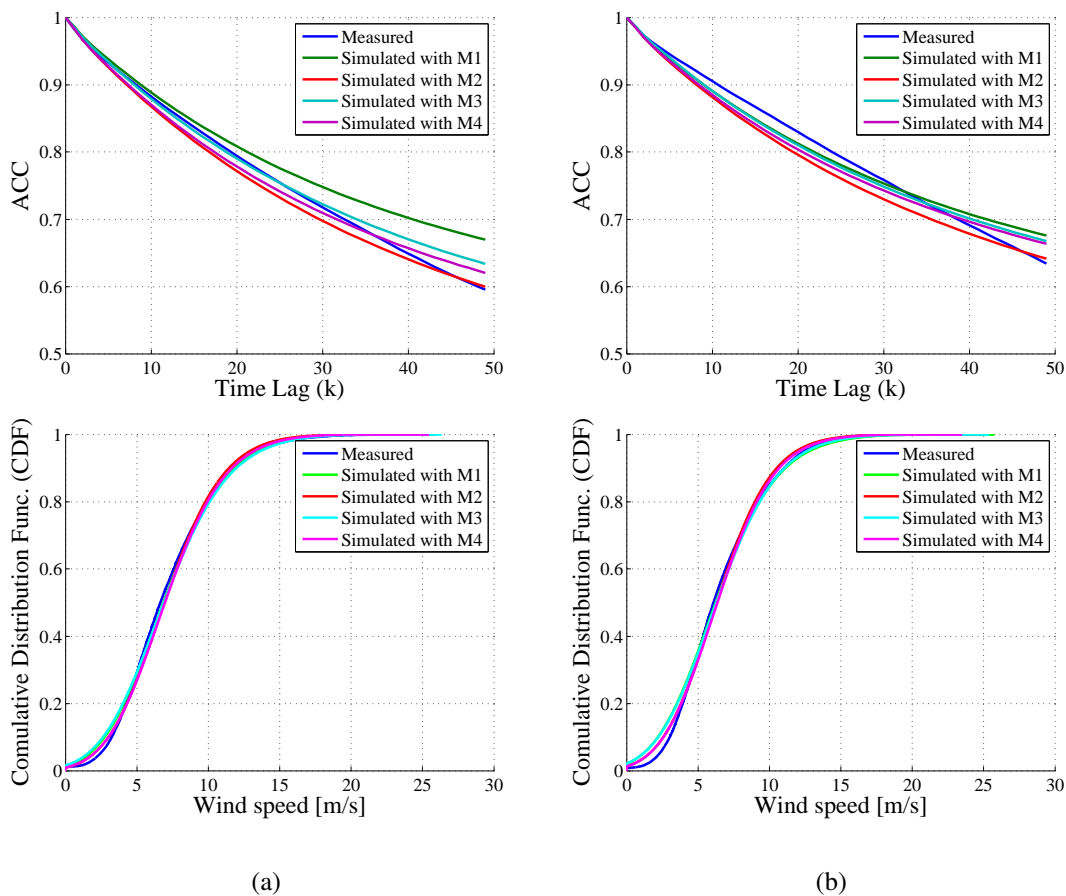


Figure 4.22: The deviation of the ACC and CDF of the simulated wind speed data from the measured wind speed (a) Näsudden Year 1 (b) Näsudden Year 2

Compared with the actual variation of ACC and CDF from year to year (as can be seen in Figure 4.21); the deviation of the ACC and CDF of the simulated wind speed, resulting from different models, from the measured wind speed data is relatively smaller. Similar result is observed when analysing Year 3, Year 4 and Year 5 wind speed data at Näsudden. From this, it can be concluded that in the Baltic sea region and to some extent in the north sea region where there is no measured wind speed data, the model presented in Table 4.5 and Table 4.6 can be used to simulate wind speed data having acceptable relevant properties given an average wind speed value in the area.

Table 4.5: HF component

	M1	M2	M3	M4
σ^2	0.5697	0.5493	0.5776	0.5617
ϕ_1	1.0247	1.0288	1.0232	1.0132
ϕ_2	-0.1291	-0.1316	-0.1188	-0.1182
ϕ_3	0.0491	0.0576	0.0357	0.0448
ϕ_4	0.0069	-0.0098	0.0235	0.0029
ϕ_5	0.0136	0.0126	0.0128	0.0246
ϕ_6	-0.0013	0.0079	-0.0106	-0.0047

Table 4.6: LF component

	M1	M2	M3	M4
σ^2	0.2395	0.2325	0.2425	0.2376
θ_1	0.2832	0.2795	0.2539	0.2362
θ_2	0.5549	0.5547	0.5736	0.6733
θ_3	0.0156	0.0525	0.1602	-0.0582
θ_4	0.0322	0.1603	-0.0429	-0.0254
θ_5	0.0064	-0.1111	-0.1061	0.1653
θ_6	0.0097	-0.0662	0.083	-0.0081

4.4 Time and space correlated wind power model

Recall that ARIMA based modelling procedure is used not only to model time correlated wind speed data, but also it can be used to model time and space correlated wind speed data. In this section, the application of VARIMA modelling procedure to develop VARIMA wind speed model is discussed. The application of the VARIMA modelling procedure for wind speed modelling in the north sea is demonstrated by modelling time and space correlated wind speed data at two locations and six locations.

4.4.1 Geographically distributed wind speed data in the North Sea

Similar to the univariate ARIMA modelling procedure, the first step in VARIMA modelling procedure is to get the measured or observed time and space correlated wind speed data. For this purpose, sample data in the north sea area is considered. The geographically distributed sample wind speed data used in this investigation is obtained from NASA (National Aeronautics and Space Administration) Earth science data centre [65], the data point of which is shown in Figure 4.23. Figure 4.23 shows 12*11 data points in the North Sea region where each point has an hourly average wind speed data over a year, from January 1, 2012 up to December 31, 2012 where observed wind speed data is made at a height of 50 m. The data points are bounded in the longitude range from 0° to 7.3333° and the latitude range from 53.5° to 58.5° . The grid points along the longitude are 0.6667° apart and those along the latitude lines are 0.5° apart. Assuming $1^\circ \text{longitude} = 63\text{km}$ and $1^\circ \text{latitude} = 111\text{km}$ in the area of interest, the distance between points along a longitude line is about 42 km and the one along the latitude line is about 55 km.

In order to check the validity of the data obtained from NASA in the area of interest, the space correlation of the time series wind speed data in the area is analysed the result of which is shown in Figure 4.24. Figure 4.24(a) shows the space correlation of the time series data at zero time lag along a 0° longitude line where the latitude ranges from 53.5° to 58.5° assuming $1^\circ \text{latitude} = 111\text{km}$. Figure 4.24(b) shows the meteorological observation of wind direction and pressure map during a specific time at the same area. Both results in Figure 4.24 show that there is a strong space correlation in the area. Based on this analysis, it is assumed that the wind speed data obtained from NASA are considered valid.

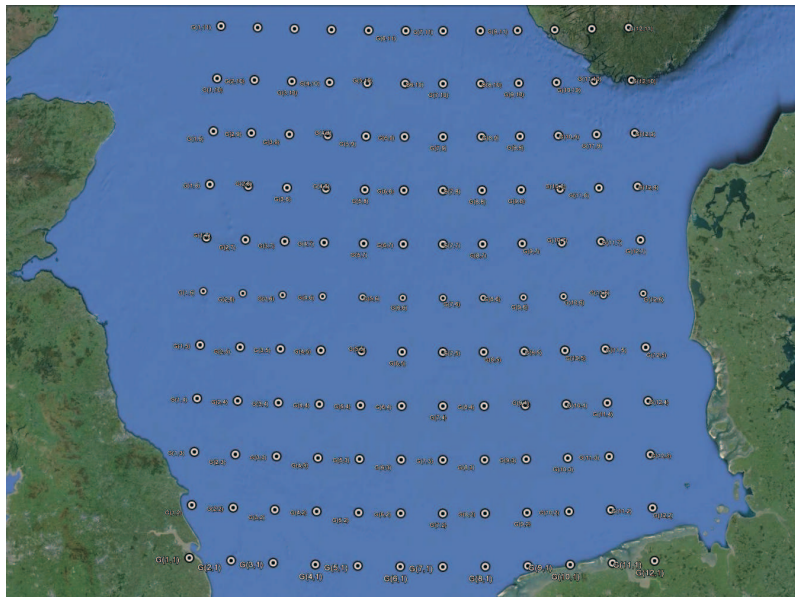


Figure 4.23: Geographically distributed sites in the offshore North Sea area each site having time series wind speed over one year (January 1 - December 31, 2012)

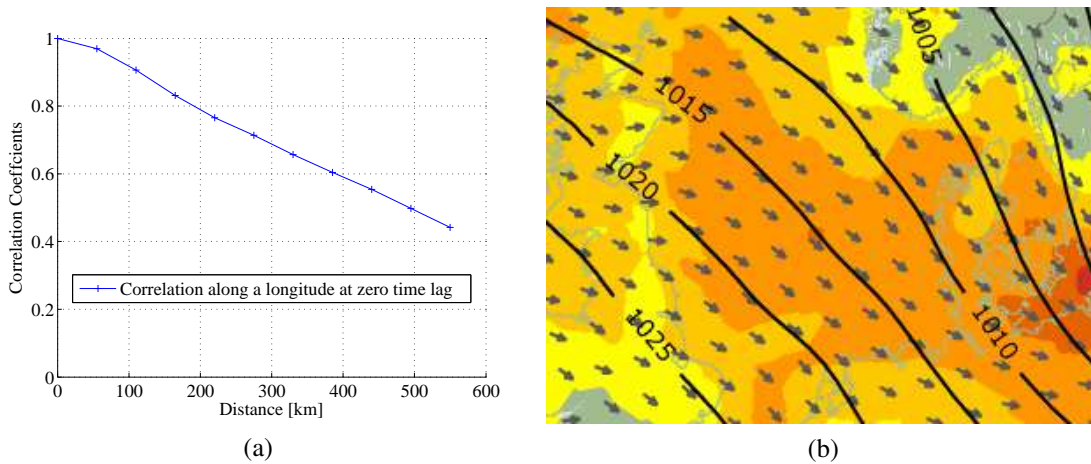


Figure 4.24: (a) Cross-correlation coefficient of wind speed data along a longitude (b) meteorological observation of wind direction and pressure map in the North Sea at a given time

4.4.2 Time and space correlated wind speed model between two sites

As described above, time and space correlated wind speed can be modelled using the VARIMA model. Similar to the univariate ARIMA modelling procedure presented in Section 4.1, the first step in VARIMA modelling is model identification. It is often tricky to identify a model structure for a VARIMA. However, model identification procedure of a univariate ARIMA can be applied to the individual time series data within the multi-variate time series data set, which can be used as a good start to identify the VARIMA model.

In this sub-section, a VARIMA model is developed for wind speed data from two locations which are geographically separated in the North Sea. The selected grid points

4.4. Time and space correlated wind power model

are $G(1, 1)$ and $G(5, 5)$, which can be seen in Figure 4.25 which shows the approximated coordinates of the two sites considered in the model. Site 1, $G(1,1)$ has a coordinate of $(0^\circ, 53.5^\circ)$ and similarly site 2, $G(5,5)$ has a coordinate of $(2.6667^\circ, 55.5^\circ)$. Note that in the coordinate pairs, say $G(x,y)$, x represent the longitude and y represents the latitude. Since the angle difference between each grid points in Figure 4.23 along the longitude line is 0.6667° and the angle difference between each grid points in along the latitude line is 0.5° , the coordinate of any other grid point $G(i,j)$ can then be calculated as $0 + (i - 1) * 0.6667^\circ, 53.5 + (j - 1) * 0.5^\circ$.

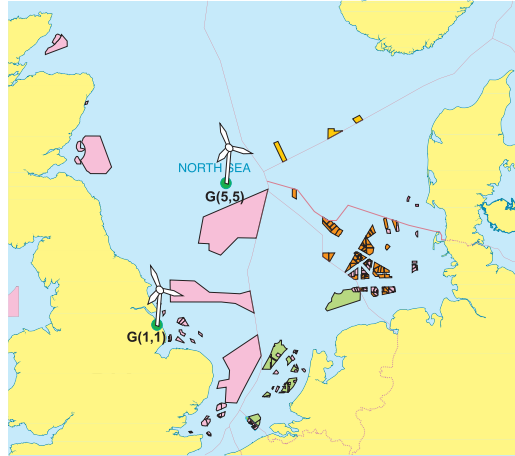


Figure 4.25: Locations of the two wind speed data sites in the North Sea

Figure 4.26 shows (a) the observed hourly average wind speed data from NASA over a year at Site 1 and Site 2 and (b) the corresponding ACC and PACC of the observed data. The average wind speeds at Site 1 and Site 2 are 7.2854 m/s and 8.8654 m/s respectively.

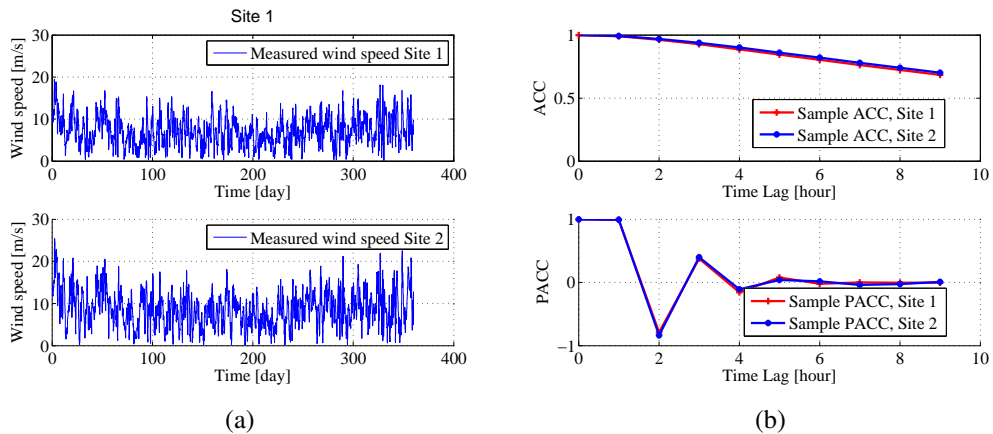


Figure 4.26: Measured quantities at Site 1 and Site 2, (a) hourly wind speed data over a year (b) ACC and PACC of the observed wind speed

It is very tricky to use differencing in a VARIMA model to transform the data and is not recommended for the transformation of multi-variate time series data. Instead, variance transformation is recommended whenever possible [60]. Table 4.7 shows the transformation factor, the corresponding transformation and the resulting residual errors of the wind speed data at both sites.

Table 4.7: Box-Cox Power Transformation and Logarithm of the residual sum of squares of the time series wind speed data

Transformation factor (v)	Transformation	$\lg(SS(v)) - G(1, 1)$	$\lg(SS(v)) - G(5, 5)$
-2	$y(t)^{-2}$	18.0411	21.22
-1	$y(t)^{-1}$	13.2881	14.3902
-0.5	$(\sqrt{y(t)})^{-1}$	12.1591	12.7638
0	$\lg(y(t))$	11.6307	12.1225
0.5	$\sqrt{y(t)}$	11.4541	11.9236
1	$y(t)$	11.4990	11.9682
1.5	$y(t)^{3/2}$	11.4541	11.9020
2	$y(t)^2$	12.0141	12.5028

Table 4.7 shows that the transformation factor $v = 0.5$ results in the minimum residual error and hence it is used to transform the data. The ACC and PACC of the resulting time series data is similar the one in shown in Figure 4.26. Using this result, the initial VARIMA model is identified as VARIMA(6,0); the sixth order vector auto-regressive model where $p = 6$ and $q = 0$. Using the transformed time series data, the model parameters are estimated using a function in MATLAB, called *vgxset*. The estimated model parameter is then used to generate the simulated wind speed data.

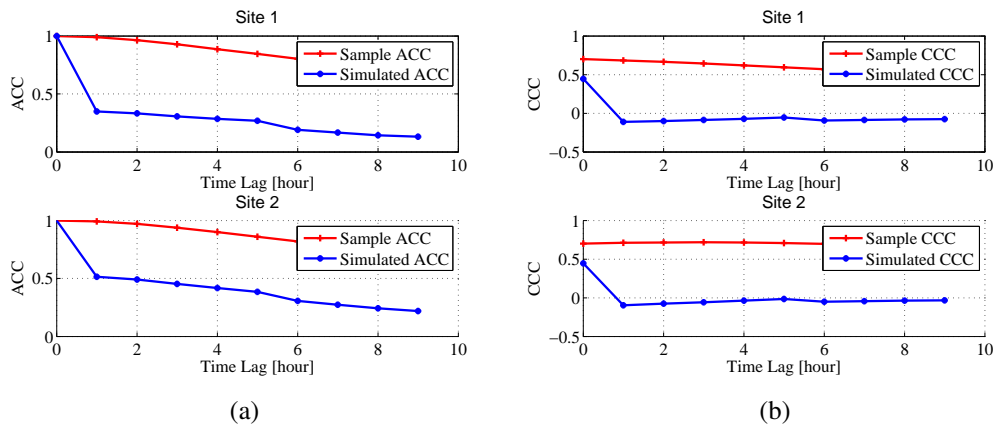


Figure 4.27: Comparison of observed and simulated data (a) ACC at site 1 and 2 (b) Cross Correlation Coefficient (CCC) at site 1->2 and 2->1 for $v = 0.5$

Figure 4.27 shows the ACC, PACC and CCC of the observed and the simulated wind speed data at the two sites. Figure 4.27 shows (a) ACC and (b) CCC of the observed and the simulated time series data at both sites. Both results shows that the ACC and CCC of the wind speed data are poorly captured by the model. It is observed that the main source of the problem is the choice of the transformation factor, v .

Note in Table 4.7 that the logarithm of the residual sum of squares of the time series data of both sites are close to one another, especially those resulting from the transformation factors in the range of $[-0.5, 2]$. In order to select the 'best' value of the transformation factor in the indicated range, the sensitivity of the model to different values of transformation

4.4. Time and space correlated wind power model

factors is made the results of which are presented in the following figures.

Figure 4.28 shows the sensitivity of the ACC of the simulated wind speed data at site 1 and 2 as a function of different transformation factors. The results in Figure 4.28 show that the transformation factor, $v = 1.5$, resulted in the 'best' result in terms of simulated ACC at both sites compared with the measurement. Observe, the transformation factors $v = 1$ and $v = 2$ have also resulted in good results although the results are not as $v = 1.5$.

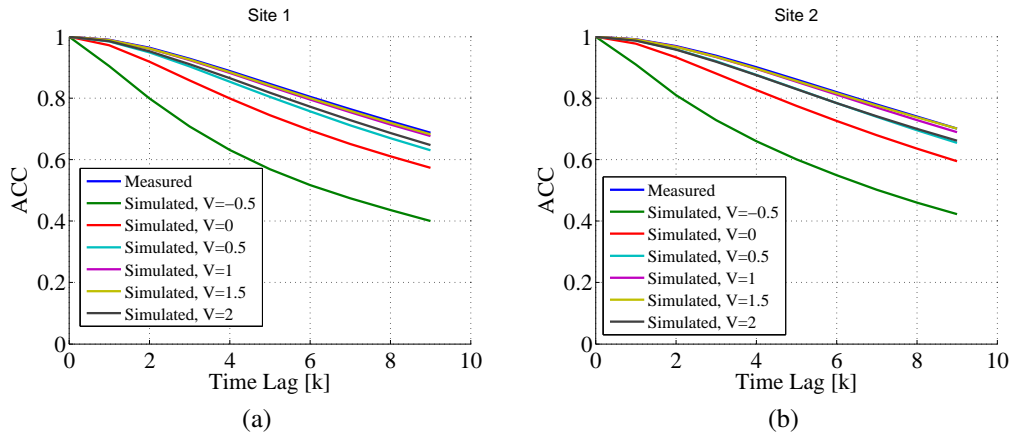


Figure 4.28: Sensitivity of simulated ACC as a function of transformation factor at site (a) 1 (b) 2

Figure 4.29 shows the sensitivity of the CCC of the simulated wind speed data at site 1 and 2 as a function of different transformation factors. In contrast to the result in Figure 4.28, the results in Figure 4.29 show that the transformation factor, $v = 1$ and $v = 2$, resulted in the 'best' result in terms of simulated CCC at both sites compared with the measurement.

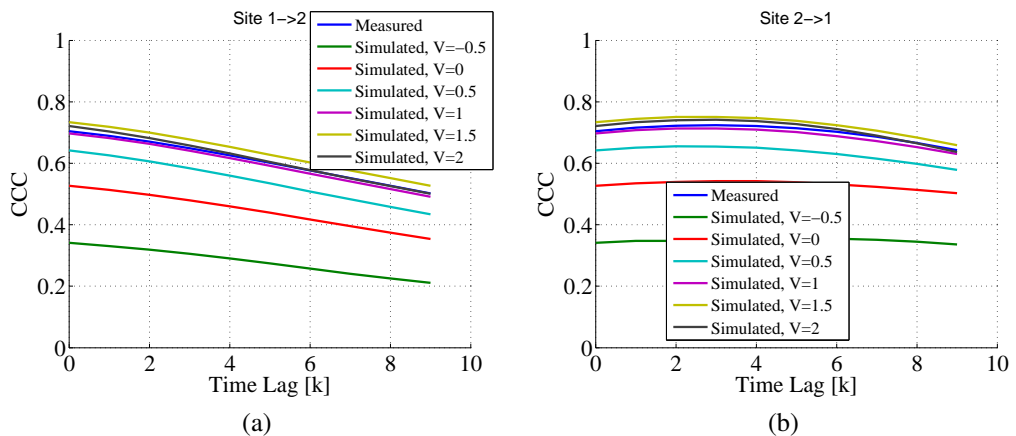


Figure 4.29: Sensitivity of simulated CCC as a function of transformation factor at site (a) 1 (b) 2

However, the match in ACC and CCC of the measured and the simulated wind speed is a sufficient condition for the model to be good enough. The model should also produce a good match in the probability distribution of the measured and the simulated wind speed data. Figure 4.30 shows the sensitivity of the CDF of the simulated wind speed data at

site 1 and 2 as a function of different transformation factors. In contrast to the results both in 4.28 and Figure 4.29, the results in Figure 4.30 show that the transformation factor, $v = 0.5$, resulted in the 'best' result in terms of simulated CDF at both sites compared with the measurement. From the figure, it is also observed that the values v in the range of 0.5 and 1 can produce a better result compared the other transformation factors.

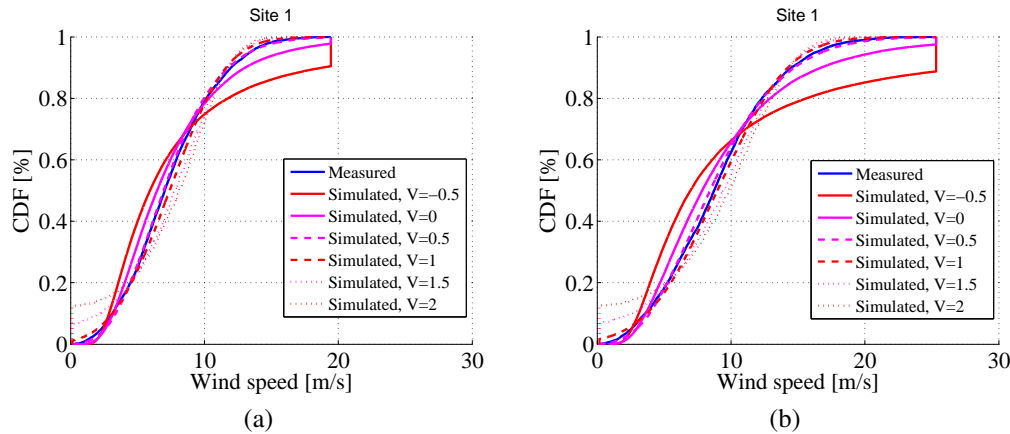


Figure 4.30: Sensitivity of simulated CDF as a function of transformation factor (a) Site 1 (b) Site 2

Note at this point that for the same model structure, different values of transformation factors have produced the 'best' simulation results in terms of ACC, CCC and CDF. The transformation factors $v = [1.5, 2, 0.5]$ have produced the 'best' simulation results in ACC, CCC and CDF respectively. This variation could be due to the fact a given transformation factor produces uneven effect a lower and higher wind speed values. This can be seen in Figure 4.30 for $v = 1.5$ and $v = 2$, where the CDF of the simulated wind speed diverges from the measurement more at the lower wind speed values than otherwise. This implies that the simulation results can be improved by shifting the observed wind speed time series data before transformation. In order to show this, simulations are made using different combinations of transformation factors, $v = [0.5, 1, 1.5, 2]$ and shift factors, $Tsh = [0, 10, 20, 30, 40]$. Out of all the possible combinations, it is found out that the result with a transformation factor $v = 2$ and different shift factors are found to be more relevant as can be seen in the following figures.

Figure 4.31(a) shows the variation of the ACC of the simulated wind speed as a function of shifting factor for a transformation factor, $v = 2$ at site 1. Note that the results at site 2 are similar to the results at site 1. Note also that Tsh stands for the shifting factor and $Tsh = 0$ stands for the simulation results when the observed wind speed data is not shifted before transformation. The results in Figure 4.31(a) show that for the transformation factor, $v = 2$, shifting the observed wind speed data before transformation improves the ACC of the simulated wind speed compared with the measurement. The result shows that the ACC of the simulated wind speed converges toward the ACC of the measured wind speed as the shift factor increases from 0 to 20. However, as the shift factor increases from 20 to 30 and then to 40, the ACC of the simulated wind speed starts to diverge from the ACC of the measured wind speed. This again indicates that, for a transformation factor, $v = 2$, the shift factor that can give the best match in the ACC of the measured and simulated wind speed lies somewhere in between $Tsh = 20$ and $Tsh = 30$. This result may change if different

4.4. Time and space correlated wind power model

values of v are considered. Figure 4.31(b) shows the variation of the CCC of the simulated

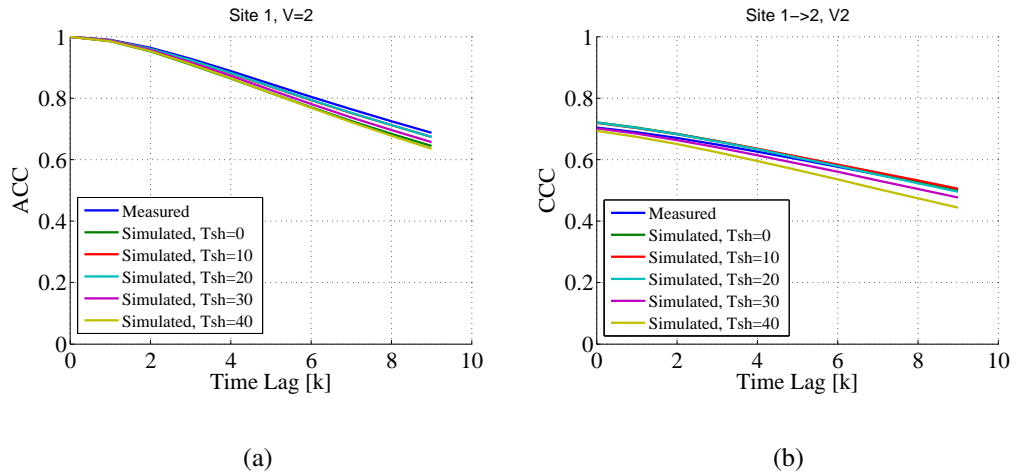


Figure 4.31: Sensitivity of simulated (a) ACC and (b) CCC as a function of shift factors for $v = 2$ Site 1

wind speed (from site 1 to site 2) as a function of shifting factor for a transformation factor, $v = 2$. Similar to the results in Figure 4.31(a), the CCC of the simulated wind speed converges toward the CCC of the observed wind speed data as the shift factor increases from 0 to 20. As the shift factor increases further, the CCC of the simulated wind speed diverges from the CCC of the measurement.

Figure 4.32 shows the variation of the CDF of the simulated wind speed as a function of shifting factor for a transformation factor, $v = 2$ at site 1. Note in Figure 4.32 that the CDF of the simulated wind speed are improved compared with the CDF of the observed wind speed, especially at the lower wind speed range. For all the shift factors, other than zero, the CDF of the simulated wind speed are quit similar.

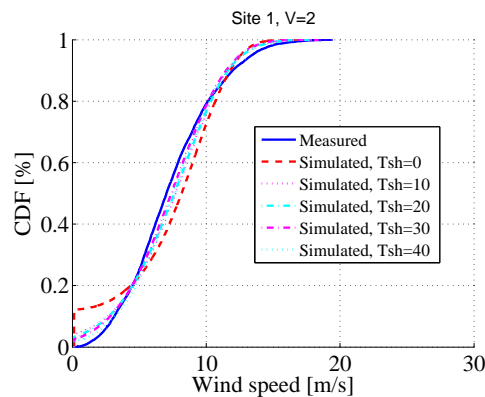


Figure 4.32: Sensitivity of simulated CDF as a function of shift factors for $v = 2$ Site 1

The analysis made above showed that a proper choice of the transformation factor combined with the shift factor can produce a simulated wind speed data with a good match both in ACC, CCC and CDF compared with the measurement. As a result, general recommendation that can be made at this point is to chose transformation factor between 0.5

and 1.5 and to use the appropriate shifting factor that can give result is a good match in the relevant parameters all at the same time. Figure 4.33 and Figure 4.34 show the results when a transformation factor $v = 1.5$ and a shifting factor $T_{shift} = 35$ are used. Figure 4.33 shows the improved ACC and CCC of the measured and the simulated wind speed data.

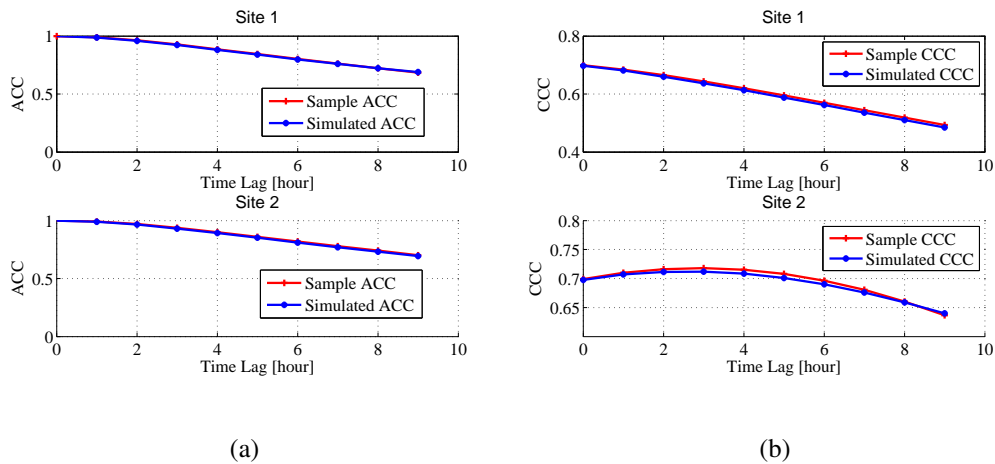


Figure 4.33: Measured and simulated data at site 1 and 2 for $v = 1.5$ and $T_{shift} = 35$ (a) ACC (b) CCC

Figure 4.34 shows the measured and simulated CDF and time series wind speed data. Figure 4.34(a) the CDF of the measured and the simulated wind speed data at both sites showing a good match. Figure 4.34(b) shows the resulting simulated and measured wind speed data at site 1. Similar result is observed at site 2.

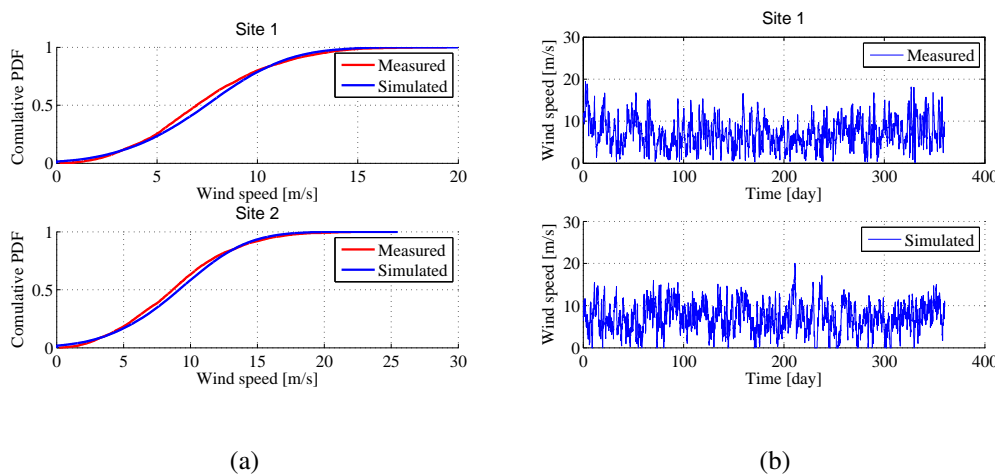


Figure 4.34: Measured and simulated data at site 1 and 2 for $v = 1.5$ and $T_{shift} = 35$ (a) CDF (b) wind speed

4.4.3 Time and space correlated wind speed model among six sites

In this subsection, the VARIMA model for wind speed data from six sites is developed. The geographical coordinates of the wind sites in the North Sea are shown in Figure 4.35, which illustrates the geographical distribution of the selected sites with their corresponding relative coordinates in space. The sites are purposely chosen such that the simulated results can be easily understood. The selected sites are named as G(1,1) (Site 1), G(1,2) (Site 2), G(5,5) (Site 3), G(5,6) (Site 4), G(9,9) (Site 5) and G(9,10) (Site 6). The corresponding coordinates associated to each site (in the form of (longitude, latitude) pair) can be determined using the method described in Section (4.4.2). For example, Site 1 and 2 are next to each other along a longitude line with the corresponding coordinates of (0,53.5) and (0,54) respectively.

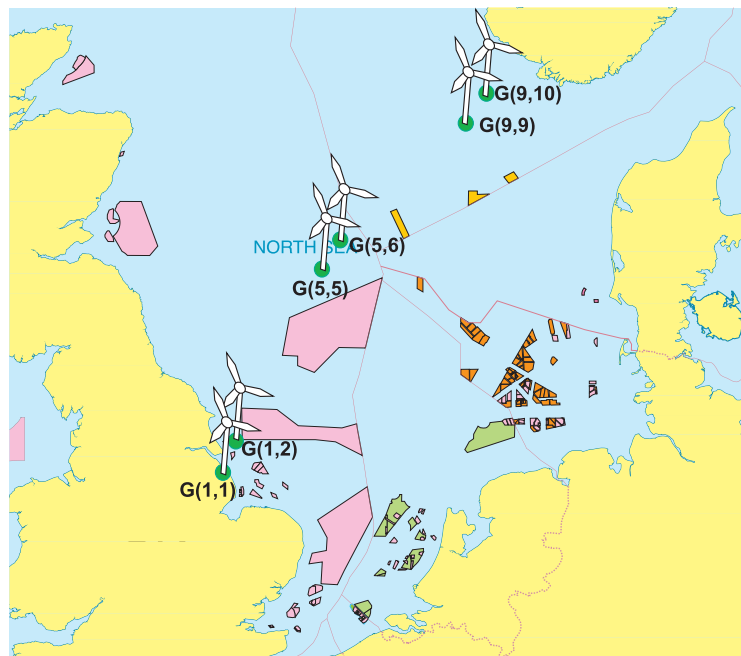


Figure 4.35: Location of the six sites

Since the sample wind speed time series data at different locations are non-stationary, the first step is to determine the appropriate transformation factors that can transform the time series data into a stationary one. Similar to the procedure used in the bi-variant VARIMA modelling described in Section (4.4.2), the variance transformation factors of $v = [-2, -1, -0.5, 0, 0.5, 1, 1.5, 2]$ are applied to each sample data at every grid points. The result showed that the transformation factor $v = 0.5$ resulted in the minimum residual sum of squares. Using this transformation factor and analysing the ACC and PACC of the individual transformed wind speed data, the model structure is found to be VARIMA(5,0).

The identified model, VARIMA(5,0), is simulated and the results are found to be not good enough. In order to improve the simulated results, an analysis of the model is made by slightly changing the transformation factor around the selected value, $v = 0.5$. The analysis has resulted in the fact that a much better simulation result can be obtained by using a transformation value of $v = 0.9$.

Figure 4.36 show the comparison of the observed and the simulated wind speed time series data at the six geographically distributed sites where Figure 4.36(a) shows the observed wind speed data and Figure 4.36(b) shows the simulated wind speed data over one month. As expected, the simulated wind speed data at site pairs [G(1,1), G(1,2)], [G(5,5), G(5,6)] and [G(9,9), G(9,10)] are strongly correlated similar to the observed data, as can easily be seen from the figure. Similarly, there is a weak correlation among the location pairs as can be seen both from the measured and simulated time series wind speed data.

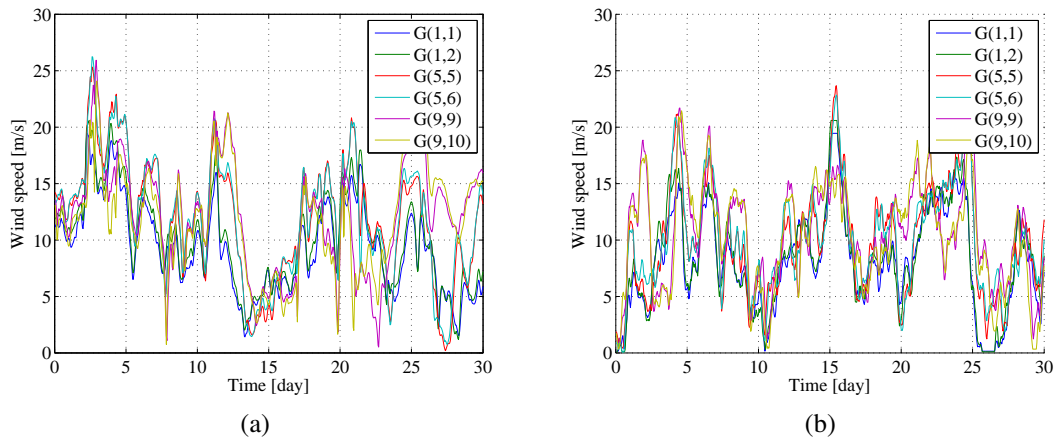


Figure 4.36: An hourly average observed and simulated wind speed data at the six Sites during a year

Similarly, Figure 4.37 shows the comparison the observed and simulated correlation in time (ACC and PACC) of the time series wind speed data. The results show that there is a good match between the observation and the simulation in terms of time correlation. Note also that the model captures the ACC in a better way than it capture the PACC at all sites.

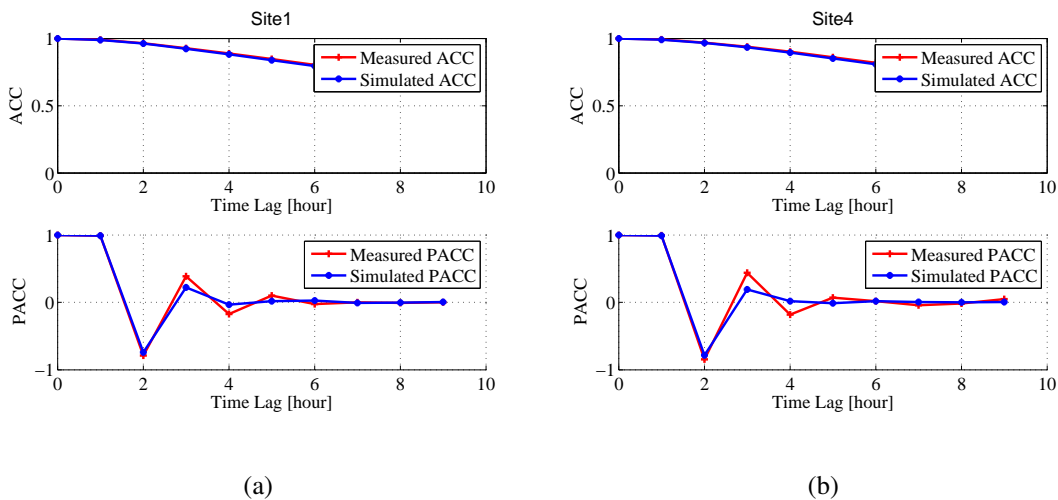


Figure 4.37: Comparison of observed and simulated time correlation (ACC and PACC) at some of the sites

4.4. Time and space correlated wind power model

Figure 4.38 shows the CDF plots of the observed and the simulated wind speed data at all sites. The results show that there is a good match in the CDF of the observed and the simulated wind speed data at all sites.

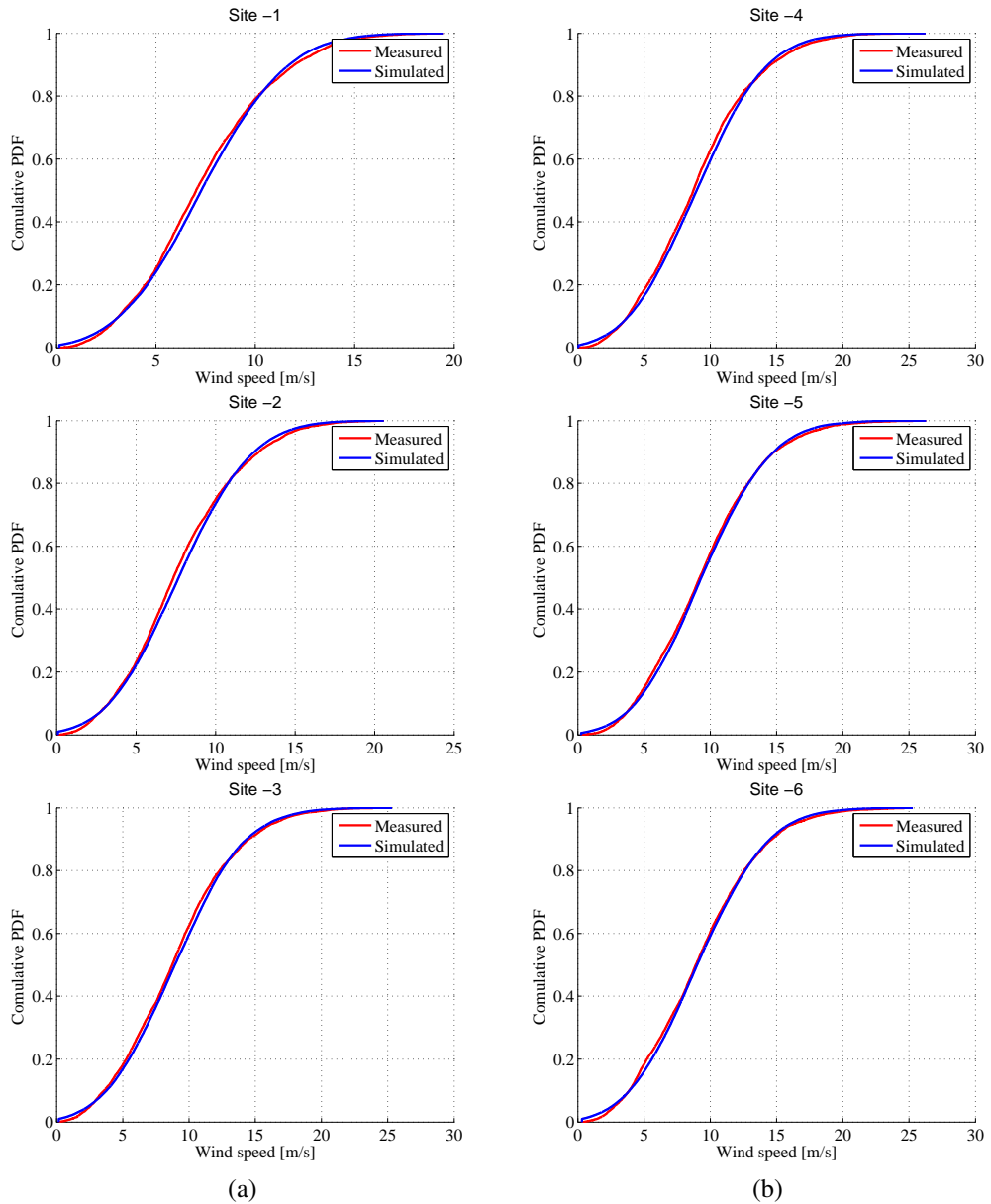


Figure 4.38: Comparison of the observed and simulated cumulative probability density function (CDF) at the six sites which are geographically distributed in space

Figure 4.39 shows the space or CCC plots of the observed and the simulated wind speed data at all sites. The results clearly show that the model captures the space correlation in a much better way compared with the some simulation results.

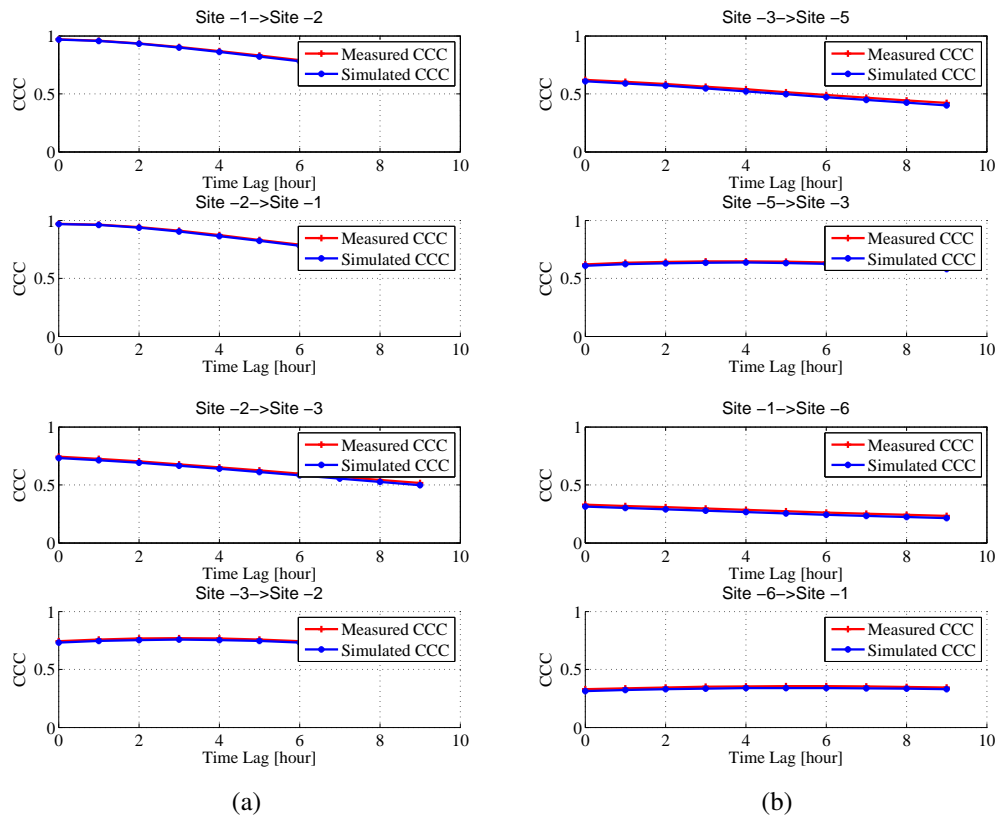


Figure 4.39: Comparison of measured and simulated space or CCC at all the six sites

4.4.4 General recommendation on VARIMA model

It has been demonstrated that the similar procedure defined for the uni-variate ARIMA modelling procedure can be used for VARIMA modelling. An first step to develop a VARIMA model is to determine the structure of the model. From the analysis made above it is observed that, to model an hourly average time and space correlated wind speed in the north sea region, using a VARMA of model structure ($VARMA(6, 0, 0)$) can produce a result that is good enough. Moreover, it is demonstrated that the choice of a proper transformation factor is crucial to produce good result. The analysis made in this section has also demonstrated that the choice of the transformation factor between 0.5 and 1.5 can produce acceptable results. In addition, while choosing the transformation factor in the suggested range, it we recommend beginning with a value of 0.9. And finally, considering the shifting the time series wind speed data while making the choice of the transformation factor is also another recommendation.

Chapter 5

Supervisory control in HVDC grids

Distributed local droop controllers, as discussed in Section 2.1.3, are the most discussed control strategy in HVDC transmission systems. This strategy enables shared management of a disturbance in the system among all buses having the droop control capability. However, the analysis made in this chapter shows that in an HVDC grid, local droop controllers alone cannot guarantee to keep the branch power flows in the system within the limiting values after a disturbance. Taking the inadequacy of local droop controllers into account, the need for a supervisory controller is discussed and the proposed supervisory control algorithm is presented in this chapter. In addition, the architecture of the hierarchical operation of local droop controllers (primary controller) followed by the supervisory controller (secondary controller) is demonstrated with case studies. Moreover, the maximum WPP capacities that can be integrated into a given system, without losing the controllability of the system, is also estimated. An important application of the proposed control strategy in this chapter is its use in the economic analysis of the HVDC transmission systems investigated in this thesis, as discussed in Chapter 6.

Figure 5.1 shows an example a HVDC grid consisting of external AC grids, distributed WPPs and a local droop controller. The system can have more than one local droop controller, but only one droop controller is shown in the figure. Note that the droop controller

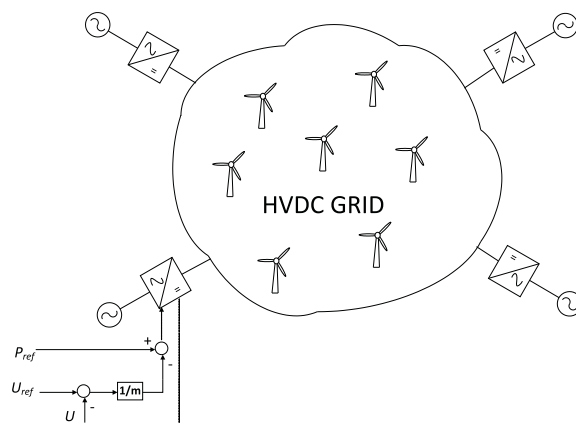


Figure 5.1: Local droop controllers in an HVDC grid

has reference power P_{ref} , reference voltage U_{ref} and a droop constant m , which should be negative. In all of the studies made in this thesis, the reference power to the controllers in the systems are the scheduled exchange power data of the system. And the reference voltages of the controllers in the system are the system bus voltages associated with the scheduled exchange power data of the system. In the following analysis, the reference power and voltage of the droop controllers are set to the base bus power and voltage of the specific case defined in Chapter 3. Recall that the scheduled exchange power data of all the cases considered in this study are defined in Chapter 3 and the magnitude of the droop constant can range from 3% to 4%, as discussed in Section 2.1.3. Observe from Figure 5.1 that the lower the value of the droop constant, the more the contribution of the local droop controllers to a disturbance will be and accordingly the lower the action of the supervisory controller. Hence, maximize the share of the power demand among the WPPs at the external connection points and to minimize the action of the supervisory controller, a 3% droop constant is used in this chapter and in Chapter 6.

5.1 Droop control strategy

Figure 5.2 shows uncontrolled simulation results when the system in Case 2, presented in Section 3.2, is simulated with a wind power profile from the WPP in the system with a capacity of 1700 MW. Figure 5.2(a) shows uncontrolled bus power profiles from the external connection points (NO and NL) and the WPP (WF 1) during the first 48 hours of the year. Figure 5.2(b) shows uncontrolled branch power flows in the system during the first 48 hours of the year. Observe that the power flow on branch NO->WF 1 substantially exceeds the rated power capacity of the cable (which is 1 pu in this case) during some time intervals. Of course, this is due to the integration of the WPP into the system designed for exchange and could not be allowed to operate in this condition. The objective here is to show the proposed mitigation strategy to tackle the problem resulting from the integration of the WPP into the system.

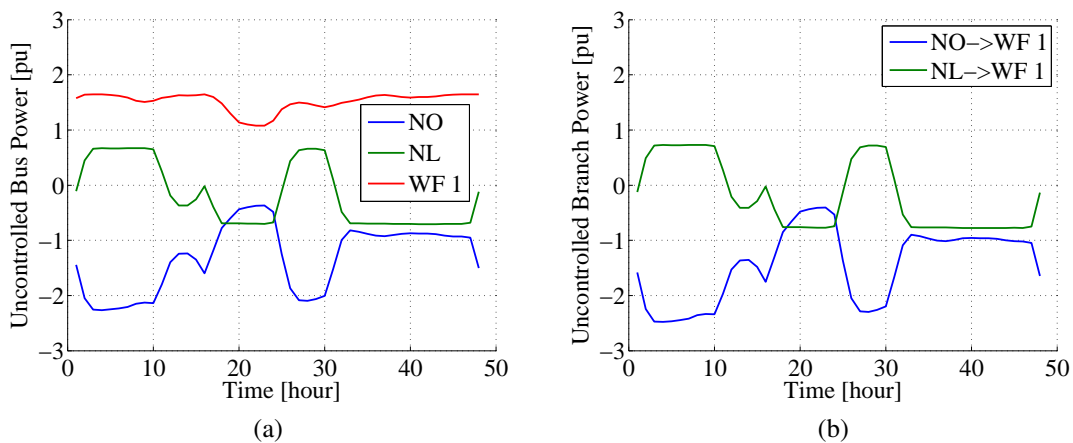


Figure 5.2: Simulation results when the WPP is connected to the system in Case without control (a) bus power profiles (b) branch power profiles during the first 48 hours of the year

Figure 5.3 shows the annual duration curves of the system bus and branch power profiles. Figure 5.3(a) shows annual duration curves of the system bus power and Figure 5.3(b) shows annual duration curves of the system branch power profiles. Note from the results in Figure 5.3(b) that the power flow on branch NO->WF 1 exceeds the rated capacity of the cable for 16% of the year getting up to 2.5 pu, where 1 pu is the rated value of the branch cable.

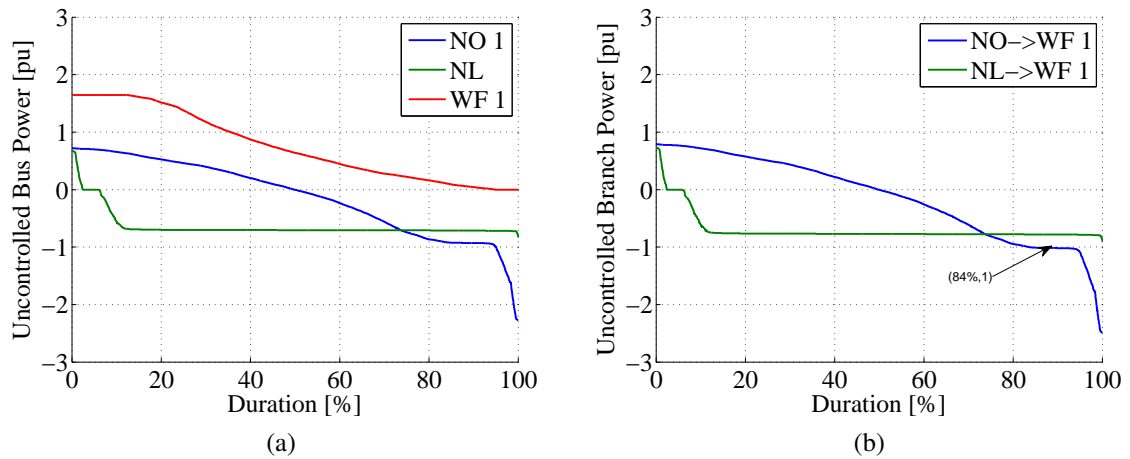


Figure 5.3: Simulation results when the WPP is connected to the system in Case without control, annual duration curves of (a) bus power profiles (b) branch power profiles

Note that Figure 5.2 and Figure 5.3 show the simulation results when the system is not controlled while connecting the WPP to the system. One way to control this system is by using a local droop controller at the bus located in the Netherlands. The local droop controller reacts when there is a disturbance in the system, which in this case is the integration the WPP to the system. Figure 5.4 shows the annual duration curves of the change in

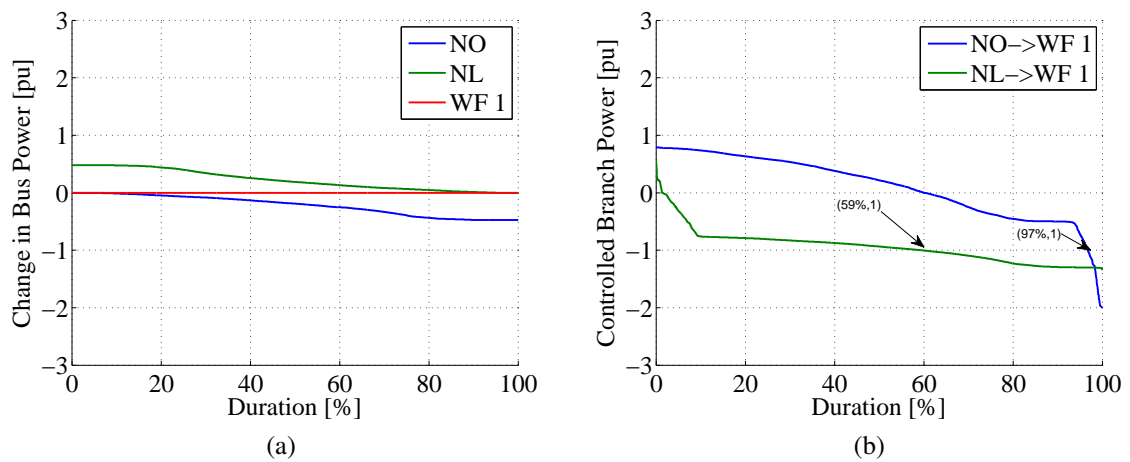


Figure 5.4: Simulation results when the WPP is connected to the system in Case with droop control, annual duration curves of (a) bus power profiles (b) branch power profiles

the scheduled bus powers and the branch power profiles when the system is controlled by

the droop controller located at the bus in the Netherlands. Figure 5.4(a) shows the annual duration curves of the change in the scheduled bus power profiles in the system resulting from the reaction of the local droop controller to the variation of power from the WPP. The maximum change in the scheduled bus power is up to about 0.48 pu. Figure 5.4(b) shows the annual duration curves of the system branch power profiles. Observe that the branch power flows on both cables in the system has exceeded the rated values of the cables during some time in the year.

There are two important differences between the results in Figure 5.3(b) and Figure 5.4(b). In contrast to the uncontrolled branch power flow in Figure 5.3(b), the maximum branch power flow on line (NO->WF 1) in Figure 5.4(b) has decreased from about 2.5 pu to about 2 pu due to the droop controller. In addition, the duration in which the line is overloaded has decreased from 16.5% to 3.2%. On the other hand, the branch power flow of line (NL->WF 1) has exceeded its rated value for about 41% of the time in the year getting up to a maximum value of 1.4 pu. Hence, one can see that the presence of the droop controller at the Netherlands has made more power to flow toward the Netherlands. This caused the power flow on the line (NL->WF 1) to exceed the limit.

Although there is a slight improvement in the peak branch power flow on branch NO->WF 1, it can easily be seen that the local droop controller alone do not guarantee that the branch power flows in the system are limited to the limiting values. This makes it important to have a supervisory control or a secondary control in the system to fix the problem which cannot be fixed by using the local droop controller.

5.2 Supervisory controller models

It is observed that the local droop controllers alone cannot limit the branch power flows in the system to its rated values all the time. This makes it important to have a supervisory controller that can make sure that the branch power flows in the system do not exceed the limiting values of the cables at any time. In order to develop a model of a supervisory control, one needs to understand the parameters affecting the power flow in the system.

A power flow in a branch is a function of a bus voltage and a current flowing through the branch which can be formulated as

$$P_{(i,j)} = U_i I_{(i,j)} \quad (5.1)$$

where $P_{(i,j)}$ is the branch power flow from bus i to bus j , U_i is the voltage at bus i and $I_{(i,j)}$ is the branch current from bus i to bus j . On the other hand, the current $I_{(i,j)}$, flowing through the branch can be calculated as

$$I_{(i,j)} = G_{(i,j)} (U_i - U_j) \quad (5.2)$$

where $G_{(i,j)}$ is the conductance of the branch from bus i to bus j and U_j is the voltage at bus j . The branch power flow can be expressed in terms of the bus voltages and the branch conductance by substituting (5.2) into (5.1), which can be formulated as

$$P_{(i,j)} = U_i G_{(i,j)} (U_i - U_j) \quad (5.3)$$

Equation (5.3) relates the bus voltages with the branch power flow. From this relationship, it is easy to see that the change in power flow on a given branch can be achieved in two ways. By changing branch conductance and/or the system bus voltages. The change in branch conductance can be achieved by either changing the physical structure of the branch or by using power electronic devices. This leads to more cost and loss in the system which should be avoided. Hence, changing the branch power flows by using the change in bus voltages seems more feasible. Hence, the change in branch power flow can be related to the change in bus voltage (for fixed value of the conductance) as

$$\Delta P_{(i,j)} = P_{(i,j)} - P_{(i,j)0} = U_i G_{(i,j)} (U_i - U_j) - U_{i0} G_{(i,j)} (U_{i0} - U_{j0}) \quad (5.4)$$

Note that $\Delta P_{(i,j)}$ is the desired change in branch power flow due to the disturbance, hence U_0 and U_i are the system bus voltages before and after the disturbance respectively. The change in bus voltage, compared with the magnitude of the bus voltage, is significantly small. Hence, the approximation, $U_i \cong U_{i0}$, is valid. Using this approximation, (5.4) can be simplified into

$$\Delta P_{(i,j)} \cong U_i G_{(i,j)} ((U_i - U_{i0}) - (U_j - U_{j0})) = U_i G_{(i,j)} (\Delta U_i - \Delta U_j) \quad (5.5)$$

Equation (5.5) shows that the change in branch power flows can be related to the change in bus voltages through bus voltages and conductances of the system. If the conductance of the system is assumed constant, the only way to affect the change in power flow in a branch is by changing the bus voltages. One way to affect the change in bus voltages is by using DC/DC converters in the system. The use of DC/DC converters in an HVDC grid could be limited due to techno-economic challenges. Achieving the change in bus voltages, and hence the change in branch power flow without using DC/DC converter, is therefore of great importance, which is the main focus of this section.

The change in bus voltage in the system can be related to the change in bus power in the system. A change in power at a given bus in a system can produce change in voltages at all buses in the system. If the power applied at a given in the system is varied while the power at all other buses are fixed, the variation of the bus voltage in the system resulting from the variation of power at the bus can be determined. If the variation of voltage at a given bus is plotted against the variation of the bus power, it forms a line with a constant positive slope. The slope of the line can be calculated as

$$m_{kj} = \frac{\Delta U_k}{\Delta P_j} \quad (5.6)$$

where m_{kj} is the slope of a line produced by the variation of voltages at bus k resulting from the variation of power at bus j , when the power at the rest of the system bus are kept constant. In this way, the change in bus voltages resulting from the change in bus powers

in the system can be related to form the elements of the droop matrix, which is formulated as

$$\begin{bmatrix} \Delta U_1 \\ \Delta U_2 \\ \cdot \\ \cdot \\ \cdot \\ \Delta U_n \end{bmatrix} = \begin{bmatrix} m_{11} & m_{12} & \cdot & \cdot & \cdot & m_{1n} \\ m_{21} & m_{22} & \cdot & \cdot & \cdot & m_{2n} \\ \cdot & \cdot & \cdot & \cdot & \cdot & \cdot \\ \cdot & \cdot & \cdot & \cdot & \cdot & \cdot \\ \cdot & \cdot & \cdot & \cdot & \cdot & \cdot \\ m_{n1} & m_{n2} & \cdot & \cdot & \cdot & m_{nn} \end{bmatrix} \begin{bmatrix} \Delta P_1 \\ \Delta P_2 \\ \cdot \\ \cdot \\ \cdot \\ \Delta P_n \end{bmatrix} \implies [\Delta U] = [m][\Delta P] \quad (5.7)$$

where ΔU_i is the change in voltage at bus i , ΔP_j is the change in power at buses j , m_{ij} is calculated as in (5.6).

Equation (5.7) relates the change in bus voltage changes to the change in bus powers through a droop matrix, m . Note that to calculate the elements of the droop matrices, only one bus power is varied at a time (while the powers at the other system buses are fixed) to calculate the change on the system bus voltages. For example, to calculate the change in bus voltages in the system resulting from the change in power at bus j , the change in power at all the system buses except the one at bus j are set to zero and the power at bus j is varied to calculate the corresponding variation in the system bus voltages from which the slopes which forms elements of the droop matrix are calculated. In this case, all elements of the droop matrix in column j represents the slope calculated using (5.6) when only the power at bus j is varied while the change in power at other buses are set to zero. Note also that the droop matrix, m , is dependent on the topology of the system and can be calculated off-line. By combining (5.5) and (5.7), the change in branch power flows in the system can be related to the change in the system bus powers which serves as a basis for the formation of the proposed supervisory controller.

5.2.1 Architecture of primary and secondary control in an HVDC grid

As discussed, the combined result of (5.5) and (5.7) forms the basis of the supervisory controller. Observe that the proposed control strategy in this study consists of not only the centralized supervisory control (secondary controller), but also the local droop controllers (primary controllers). Figure 5.5 shows an HVDC grid consisting of distributed WPPs, external AC grids and the proposed control strategy; primary control followed by secondary control. In the example shown, every external grid is connected to the HVDC grid through a converter having a primary controller and a LCU (Local Control Unit). The LCU can measure bus power, bus voltage and local branch powers and provides the measurements to the local primary controller and a CCU (Central Control Unit). The CCU takes in measurements from the LCUs and provide a new reference power and voltage that can be used by the local droop controllers when there is branch power flow limit violations. The reference power generated by the CCU can also be used by an electricity market operator.

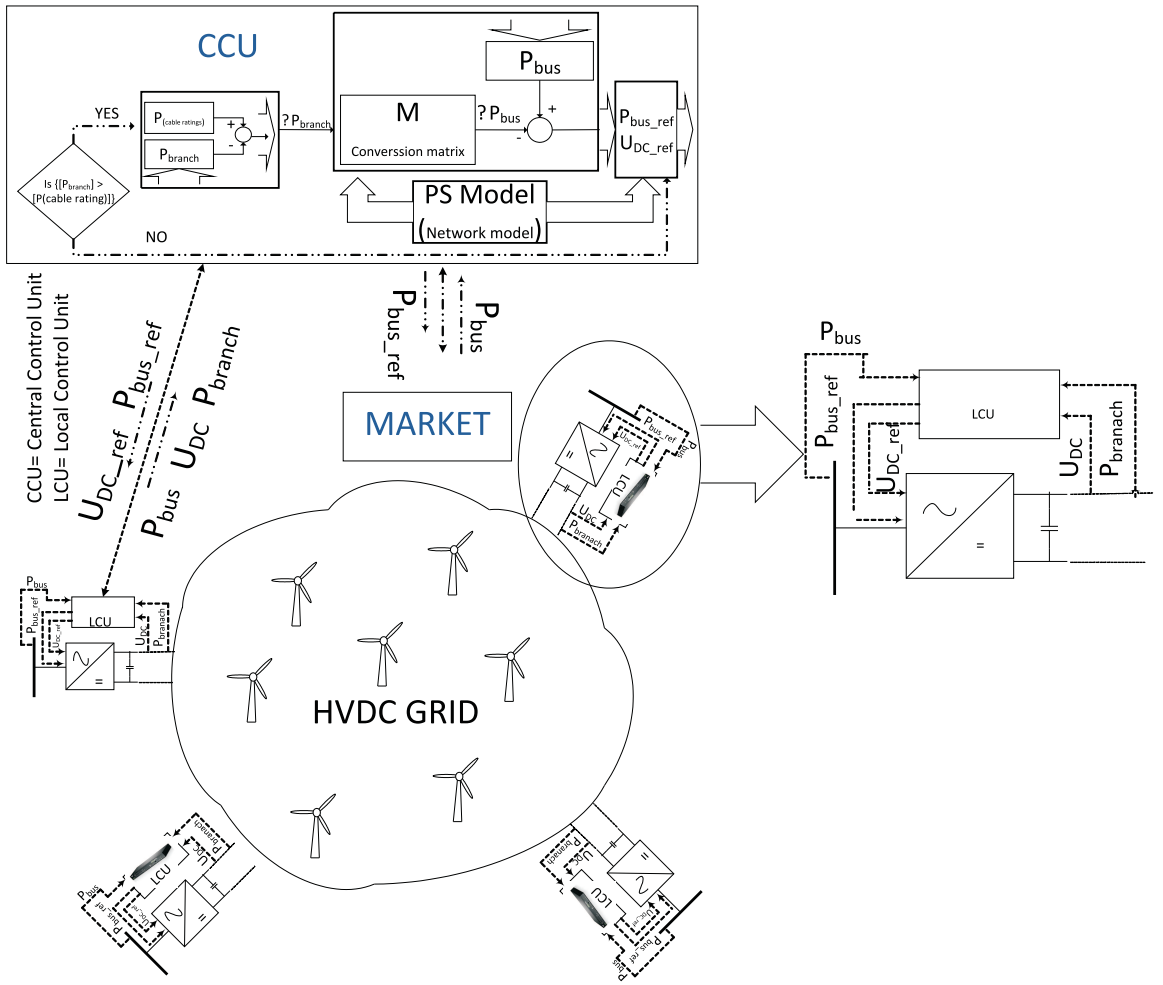


Figure 5.5: The architecture of the proposed control algorithm in a meshed HVDC grid; local primary controllers followed by the central secondary controller

5.2.2 Supervisory controller model for the system in Case 2

Taking Case 2 as an example and (5.5) as a basis, the change in branch power flow in this system can be related to the change in bus voltage of the system as

$$\begin{aligned}\Delta P_{(1,3)} &= U_1 G_{(1,3)} \Delta U_1 - U_1 G_{(1,3)} \Delta U_3 \\ \Delta P_{(2,3)} &= U_2 G_{(2,3)} \Delta U_2 - U_2 G_{(2,3)} \Delta U_3\end{aligned}\quad (5.8)$$

where 1 stands for bus *NO*, 2 stands for bus *NL* and 3 stands for bus *WF 1*. Since bus 1, located at Norway, is taken as a reference bus, ΔU_1 is zero. Hence, (5.8) can be rewritten as

$$\begin{bmatrix} \Delta P_{(1,3)} \\ \Delta P_{(2,3)} \end{bmatrix} = \begin{bmatrix} 0 & -U_1 G_{(1,3)} \\ U_2 G_{(2,3)} & -U_2 G_{(2,3)} \end{bmatrix} \begin{bmatrix} \Delta U_2 \\ \Delta U_3 \end{bmatrix}\quad (5.9)$$

Equation (5.9) formulates the relationship between the change in branch power flow and the change in bus voltage. Note that the matrix relating the change in branch power

to the change in bus voltage is dependent on the conductances and the bus voltages of the system. Hence it can only be calculated on-line. Similarly, by using (5.7), the relationship between the change in bus voltage and the change in bus power in this case can be formulated as

$$\begin{bmatrix} \Delta U_2 \\ \Delta U_2 \end{bmatrix} = \begin{bmatrix} m_{22} & m_{23} \\ m_{32} & m_{33} \end{bmatrix} \begin{bmatrix} \Delta P_2 \\ \Delta P_2 \end{bmatrix} \quad (5.10)$$

Recall that the matrix relating the change in bus voltage and the change in bus power in (5.10) depends only on the topology of the system and hence can be calculated off-line. Combining (5.9) and (5.10), the equation relating the change in branch power to the change in bus power is formulated as

$$\begin{bmatrix} \Delta P_{(1,3)} \\ \Delta P_{(2,3)} \end{bmatrix} = \begin{bmatrix} 0 & -U_1 G_{(1,3)} \\ U_2 G_{(2,3)} & -U_2 G_{(2,3)} \end{bmatrix} \begin{bmatrix} m_{22} & m_{23} \\ m_{32} & m_{33} \end{bmatrix} \begin{bmatrix} \Delta P_2 \\ \Delta P_2 \end{bmatrix} \quad (5.11)$$

$$\begin{bmatrix} \Delta P_{(1,3)} \\ \Delta P_{(2,3)} \end{bmatrix} = \begin{bmatrix} M_{11} & M_{12} \\ M_{21} & M_{22} \end{bmatrix} \begin{bmatrix} \Delta P_2 \\ \Delta P_3 \end{bmatrix} \quad (5.12)$$

Equation (5.12) forms the model of the supervisory control of the system in Case 2. Moreover, note that the power from the WPP cannot be controlled, $\Delta P_3 = 0$, which means that the power from the WPP is always injected into the grid all the time. Hence, (5.12) is reduced in to

$$\begin{bmatrix} \Delta P_{(1,3)} \\ \Delta P_{(2,3)} \end{bmatrix} = \begin{bmatrix} M_{11} \\ M_{21} \end{bmatrix} [\Delta P_2] \quad (5.13)$$

From (5.13), one can see that there are two knowns, $\Delta P_{(1,3)}$ and $\Delta P_{(2,3)}$, and one unknown, ΔP_2 . This implies that the power flow on both branches cannot be controlled at the same time, only one branch power can be controlled at a time. This phenomena is the source of a bottleneck that limits the maximum WPP capacity that can be connected to the system compared to the theoretical maximum WPP capacity. In the proposed control strategy, the branch that requires the highest change in power flow is controlled and the maximum WPP capacity that can be connected into the system is chosen in such away that the power flow on the uncontrolled branch is within the limiting value all the time.

Figure 5.6 shows the results when the system in Case 2 is controlled by the proposed control algorithm. Figure 5.6(a) shows annual duration curves of the change in the scheduled exchange powers in the system. In contrast to the results in Figure 5.4, the results in Figure 5.6 show that the supervisory control has managed to keep the branch power flows in the system within the limiting values of the cables during the whole year.

Figure 5.7 shows how the secondary controller is changing the reference power of the primary controller during the first 48 hours of the year. Observe that the secondary controller acts only when necessary. Observe also that the reference voltage of the primary controller should be changed accordingly.

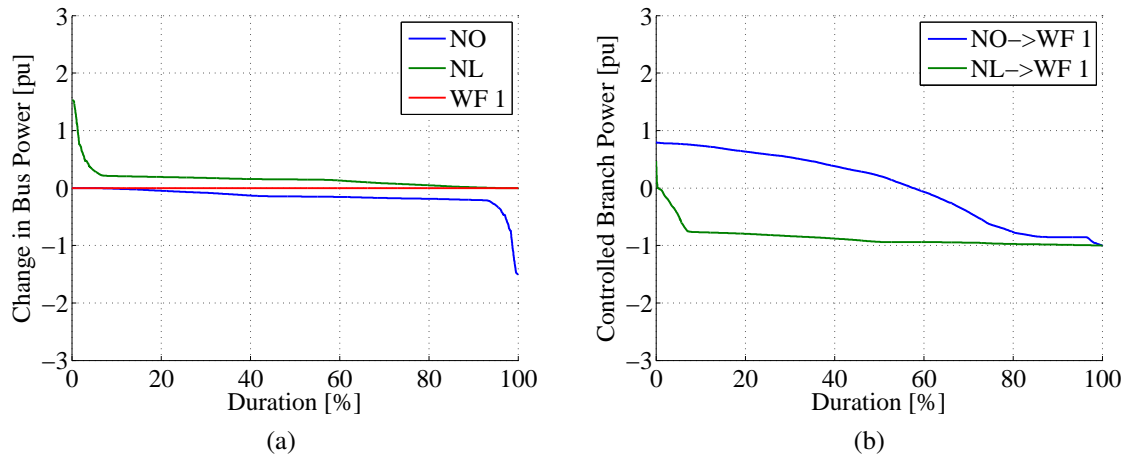


Figure 5.6: Annual duration curves of the system controlled by the primary followed by secondary control (a) change in bus power profiles (b) branch power profiles

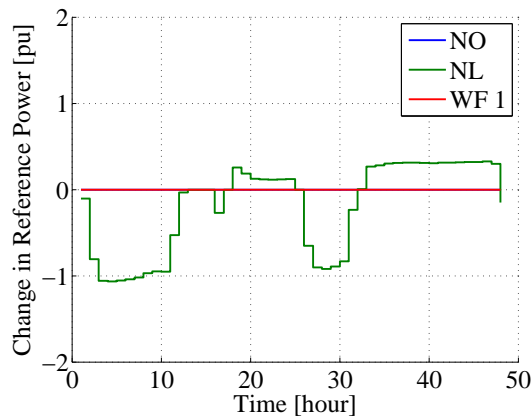


Figure 5.7: Change in the reference power of the local droop controllers during the first 48 hours of the year

5.2.3 Supervisory controller model for the system in Case 3

Similar to Case 2, Case 3 is also simulated with wind power profiles from the two WPPs in the system, WF 1 and WF 2, each having a capacity of 1700 MW and 2700 MW respectively. In order to share the disturbance in the system resulting from the integration of the WPPs, primary controllers are used at buses located in the Netherlands, Germany and Denmark.

Figure 5.8 shows normalized uncontrolled and droop controlled branch power flows in the system. Note from Figure 5.8(a) that when the system is not controlled, the branch power flows on the line NO->WF 1 and WF 1->WF 2 exceed the limiting values which get up to about -3 pu some time during the year. Figure 5.8(b) shows primary controlled branch power flows in the system. Observe that the maximum branch power flow in the system decreased from about -3 pu (uncontrolled case shown in Figure 5.8(a)) to -2 pu.

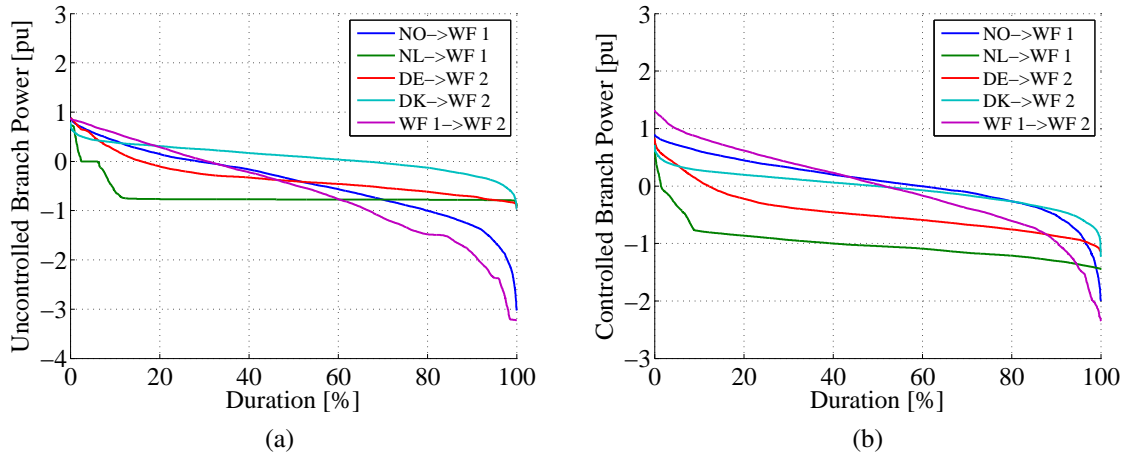


Figure 5.8: Annual duration curves of branch power flows (a) uncontrolled (b) droop controlled

Similar to the results observed in Case 2, Figure 5.8(b) shows that the primary controllers alone cannot limit the branch power flows within the limits which again indicates the need for the supervisory controller. In order to develop the model of the supervisory controller for the system defined in Case 3, the equation that relates the change in branch power flows and the change in bus voltages in the system needs to be formulated. Using (5.4) as a basis, this relationship is formulated as

$$\begin{bmatrix} \Delta P_{(1,5)} \\ \Delta P_{(2,5)} \\ \Delta P_{(3,6)} \\ \Delta P_{(4,6)} \\ \Delta P_{(5,6)} \end{bmatrix} = \begin{bmatrix} 0 & 0 & 0 & -U_1 G_{(1,5)} & 0 \\ U_2 G_{(2,5)} & 0 & 0 & -U_2 G_{(2,5)} & 0 \\ 0 & U_3 G_{(3,6)} & 0 & 0 & -U_3 G_{(3,6)} \\ 0 & 0 & U_4 G_{(4,6)} & 0 & -U_4 G_{(4,6)} \\ 0 & 0 & 0 & U_5 G_{(5,6)} & U_5 G_{(5,6)} \end{bmatrix} \begin{bmatrix} \Delta U_2 \\ \Delta U_3 \\ \Delta U_4 \\ \Delta U_5 \\ \Delta U_6 \end{bmatrix} \quad (5.14)$$

where index 1 stands for bus *NO*, 2 for bus *NL*, 3 for bus *DE*, 4 for bus *DK*, 5 for bus *WF1* and 6 for bus *WF2*. Similarly, the equation relating the change in bus voltage and the change in bus power of the system in Case 3 can be formulated as

$$\begin{bmatrix} \Delta U_2 \\ \Delta U_3 \\ \Delta U_4 \\ \Delta U_5 \\ \Delta U_6 \end{bmatrix} = \begin{bmatrix} m_{22} & m_{23} & m_{24} & m_{25} & m_{26} \\ m_{32} & m_{33} & m_{34} & m_{35} & m_{36} \\ m_{42} & m_{43} & m_{44} & m_{45} & m_{46} \\ m_{52} & m_{53} & m_{53} & m_{54} & m_{56} \\ m_{62} & m_{63} & m_{64} & m_{65} & m_{66} \end{bmatrix} \begin{bmatrix} \Delta P_2 \\ \Delta P_3 \\ \Delta P_4 \\ \Delta P_5 \\ \Delta P_6 \end{bmatrix} \quad (5.15)$$

Combining (5.14) and (5.15), the equation relating the change in branch powers and the change in bus powers in the system can be formulated as

$$\begin{bmatrix} \Delta P_{(1,5)} \\ \Delta P_{(2,5)} \\ \Delta P_{(3,6)} \\ \Delta P_{(4,6)} \\ \Delta P_{(5,6)} \end{bmatrix} = \begin{bmatrix} M_{11} & M_{12} & M_{13} & M_{14} & M_{15} \\ M_{21} & M_{22} & M_{23} & M_{24} & M_{25} \\ M_{31} & M_{32} & M_{33} & M_{34} & M_{35} \\ M_{41} & M_{42} & M_{43} & M_{44} & M_{45} \\ M_{51} & M_{52} & M_{53} & M_{54} & M_{55} \end{bmatrix} \begin{bmatrix} \Delta P_2 \\ \Delta P_3 \\ \Delta P_4 \\ \Delta P_5 \\ \Delta P_6 \end{bmatrix} \quad (5.16)$$

Note that the WPPs located at bus number 5 and 6 can not be controlled, hence $\Delta P_5 = 0$ and $\Delta P_6 = 0$. Taking this into account, (5.16) can be simplified into

$$\begin{bmatrix} \Delta P_{(1,5)} \\ \Delta P_{(2,5)} \\ \Delta P_{(3,6)} \\ \Delta P_{(4,6)} \\ \Delta P_{(5,6)} \end{bmatrix} = \begin{bmatrix} M_{11} & M_{12} & M_{13} \\ M_{21} & M_{22} & M_{23} \\ M_{31} & M_{32} & M_{33} \\ M_{41} & M_{42} & M_{43} \\ M_{51} & M_{52} & M_{53} \end{bmatrix} \begin{bmatrix} \Delta P_2 \\ \Delta P_3 \\ \Delta P_4 \end{bmatrix} \quad (5.17)$$

From (5.17), one can see that there are five known (left) and three unknown (right) variables. This implies that only three branch powers in the system can be controlled at a time. As in Case 2, the control strategy chooses the three branches with the highest required change in branch powers out of the five. Figure 5.9 shows some of the results when Case 3 is simulated using primary and secondary control. Figure 5.9(a) shows the change in the reference power of the primary controllers. Observe that the changes are made only when necessary. Figure 5.9(b) shows the duration curves of the resulting controlled branch power flows. Observe that the branch powers on line NL->WF 1 and line (DK->WH 2) still exceed the limiting values for about 0.5% of the year which gets up to -1.1 pu. If this violation cannot be tolerated in the system, it can be avoided by either reducing the capacities of the wind power plants in the system or by curtailing the wind power plants during this time or reinforcing the corresponding lines if feasible.

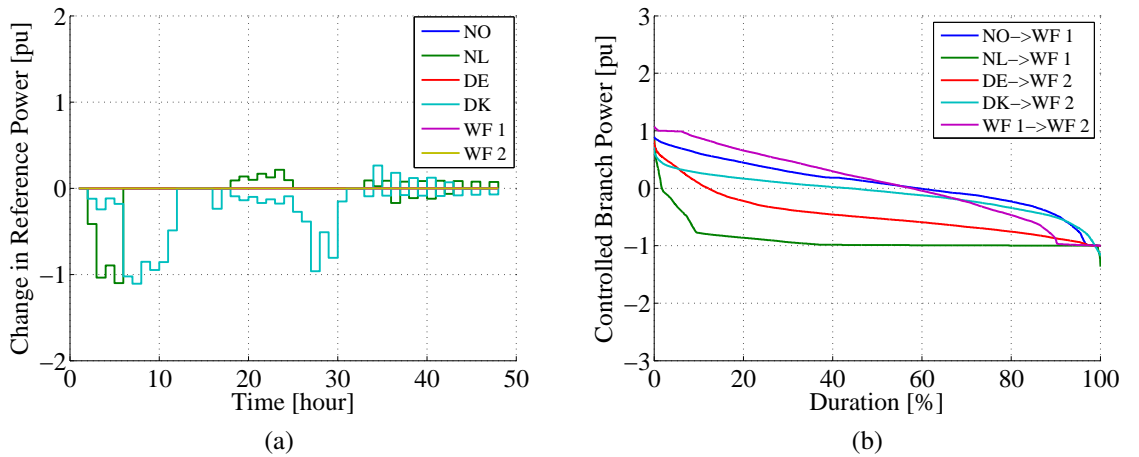


Figure 5.9: Simulation results of the system controlled by the primary followed by secondary control (a) needed change in reference power (b) annual duration curves of controlled branch power flows

5.2.4 Supervisory controller model for the system in Case 4

Recall that, there are four WPPs in Case 4, as described in Chapter 3. Recall also that the system can transport the base exchange powers without any violations. In order to investigate the impact of integration WPPs into this system, the WPP capacities presented in Table 2 are assumed.

Table 5.1: Case 4 WPP capacities

Wind Power Plant	Capacity(MW)
WF 1	1500
WF 2	2000
WF 3	1000
WF 4	1500

The system is simulated by using the base exchange powers and the power from the WPPs. Figure 5.10 shows the annual duration curves of uncontrolled and droop controlled branch power flow profiles resulting from the simulation. Figure 5.10(a) shows the annual duration curves of uncontrolled branch power flows in the system and Figure 5.10(b) shows the annual duration curves of primary controlled branch power flows in the system. From

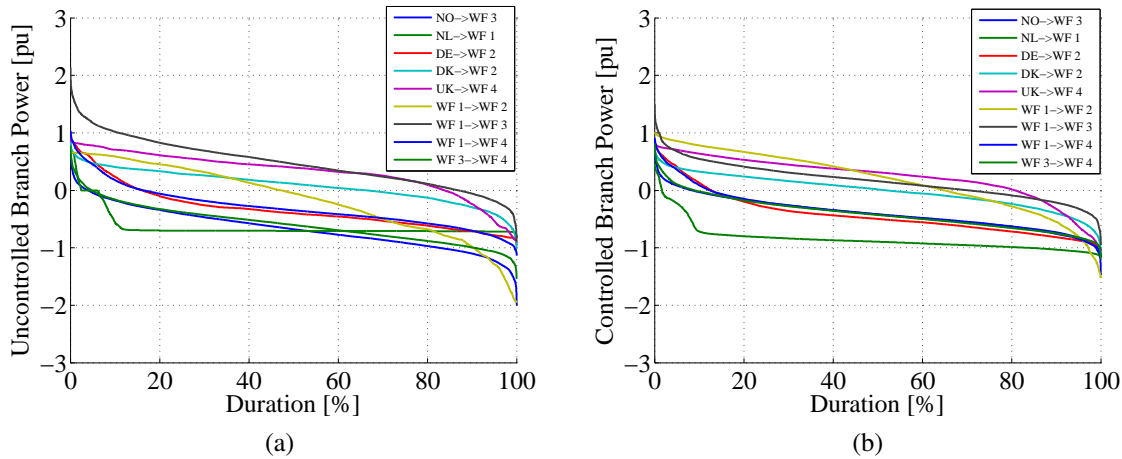


Figure 5.10: Case 4 simulation results: Annual duration curve of branch power flow (a) uncontrolled (b) droop controlled

Figure 5.10(b) one can see that the branch power flows in the system exceeds the limiting values for some time during the year, again indicating the fact that primary controllers alone cannot guarantee to keep the branch powers within the limiting values. Similar to Case 2 and Case 3, this problem can of course be reduced or avoided by using the supervisory control. Using (5.4) as a basis, the equation relating the change in branch powers and the change in bus voltages in Case 4 can be formulated as

$$\begin{bmatrix} \Delta P_{(1,8)} \\ \Delta P_{(2,6)} \\ \Delta P_{(3,7)} \\ \Delta P_{(4,7)} \\ \Delta P_{(5,9)} \\ \Delta P_{(6,7)} \\ \Delta P_{(6,8)} \\ \Delta P_{(6,9)} \\ \Delta P_{(8,9)} \end{bmatrix} = [M] \begin{bmatrix} \Delta U_2 \\ \Delta U_3 \\ \Delta U_4 \\ \Delta U_5 \\ \Delta U_6 \\ \Delta U_7 \\ \Delta U_8 \\ \Delta U_9 \end{bmatrix} \quad (5.18)$$

where

$$M = \begin{bmatrix} 0 & 0 & 0 & 0 & 0 & 0 & -U_1 G_{(1,8)} & 0 \\ U_2 G_{(2,6)} & 0 & 0 & 0 & -U_2 G_{(2,6)} & 0 & 0 & 0 \\ 0 & U_3 G_{(3,7)} & 0 & 0 & 0 & -U_3 G_{(3,7)} & 0 & 0 \\ 0 & 0 & U_4 G_{(4,7)} & 0 & 0 & -U_4 G_{(4,7)} & 0 & 0 \\ 0 & 0 & 0 & U_5 G_{(5,9)} & 0 & 0 & 0 & -U_5 G_{(5,9)} \\ 0 & 0 & 0 & 0 & U_6 G_{(6,7)} & -U_6 G_{(6,7)} & 0 & 0 \\ 0 & 0 & 0 & 0 & U_6 G_{(6,8)} & 0 & -U_6 G_{(6,8)} & 0 \\ 0 & 0 & 0 & 0 & U_6 G_{(6,8)} & 0 & -U_6 G_{(6,8)} & 0 \\ 0 & 0 & 0 & 0 & 0 & 0 & U_8 G_{(8,9)} & -U_8 G_{(8,9)} \end{bmatrix}$$

where index 1 stands for bus *NO*, 2 for bus *NL*, 3 for bus *DE*, 4 for bus *DK*, 5 for bus *UK*, 6 for bus *WF1*, 7 for bus *WF2*, 8 for bus *WF3* and 9 for bus *WF4*.

Similarly, the change in bus voltages and the change in bus power in the system defined in Case 4 can be formulated as

$$\begin{bmatrix} \Delta U_2 \\ \Delta U_3 \\ \Delta U_4 \\ \Delta U_5 \\ \Delta U_6 \\ \Delta U_7 \\ \Delta U_8 \\ \Delta U_9 \end{bmatrix} = \begin{bmatrix} m_{22} & m_{23} & m_{24} & m_{25} & m_{26} & m_{27} & m_{28} & m_{29} \\ m_{32} & m_{33} & m_{34} & m_{35} & m_{36} & m_{37} & m_{38} & m_{39} \\ m_{42} & m_{43} & m_{44} & m_{45} & m_{46} & m_{47} & m_{48} & m_{49} \\ m_{52} & m_{53} & m_{54} & m_{55} & m_{56} & m_{57} & m_{58} & m_{59} \\ m_{62} & m_{63} & m_{64} & m_{65} & m_{66} & m_{67} & m_{68} & m_{69} \\ m_{72} & m_{73} & m_{74} & m_{75} & m_{76} & m_{77} & m_{78} & m_{79} \\ m_{82} & m_{83} & m_{84} & m_{85} & m_{86} & m_{87} & m_{88} & m_{89} \\ m_{92} & m_{93} & m_{94} & m_{95} & m_{96} & m_{97} & m_{98} & m_{99} \end{bmatrix} \begin{bmatrix} \Delta P_2 \\ \Delta P_3 \\ \Delta P_4 \\ \Delta P_5 \\ \Delta P_6 \\ \Delta P_7 \\ \Delta P_8 \\ \Delta P_9 \end{bmatrix} \quad (5.19)$$

The equation that relates the change in branch powers and the change in bus powers of the system can be obtained by combining (5.18) and (5.19) which is formulated as

$$\begin{bmatrix} \Delta P_{(1,8)} \\ \Delta P_{(2,6)} \\ \Delta P_{(3,7)} \\ \Delta P_{(4,7)} \\ \Delta P_{(5,9)} \\ \Delta P_{(6,7)} \\ \Delta P_{(6,8)} \\ \Delta P_{(6,9)} \\ \Delta P_{(8,9)} \end{bmatrix} = \begin{bmatrix} M_{11} & M_{12} & M_{13} & M_{14} & M_{15} & M_{16} & M_{17} & M_{18} \\ M_{21} & M_{22} & M_{23} & M_{24} & M_{25} & M_{26} & M_{27} & M_{28} \\ M_{31} & M_{32} & M_{33} & M_{34} & M_{35} & M_{36} & M_{37} & M_{38} \\ M_{41} & M_{42} & M_{43} & M_{44} & M_{45} & M_{46} & M_{47} & M_{48} \\ M_{51} & M_{52} & M_{53} & M_{54} & M_{55} & M_{56} & M_{57} & M_{58} \\ M_{61} & M_{62} & M_{63} & M_{64} & M_{65} & M_{66} & M_{67} & M_{68} \\ M_{71} & M_{72} & M_{73} & M_{74} & M_{75} & M_{76} & M_{77} & M_{78} \\ M_{81} & M_{82} & M_{83} & M_{84} & M_{85} & M_{86} & M_{87} & M_{88} \end{bmatrix} \begin{bmatrix} \Delta P_2 \\ \Delta P_3 \\ \Delta P_4 \\ \Delta P_5 \\ \Delta P_6 \\ \Delta P_7 \\ \Delta P_8 \\ \Delta P_9 \end{bmatrix} \quad (5.20)$$

Equation (5.20) forms the basis of the supervisory control in Case 4. Note that the topology of the grid in Case 4 has one loop. Hence, out of three branches forming the loop, only two of the branches can be controlled. Similarly, there are four WPPs that cannot be controlled and hence $\Delta P_6 = 0$, $\Delta P_7 = 0$, $\Delta P_8 = 0$ and $\Delta P_9 = 0$. Taking these into account, (5.20) is reduced into

$$\begin{bmatrix} \Delta P_{(1,8)} \\ \Delta P_{(2,6)} \\ \Delta P_{(3,7)} \\ \Delta P_{(4,7)} \\ \Delta P_{(5,9)} \\ \Delta P_{(6,7)} \\ \Delta P_{(6,8)} \\ \Delta P_{(6,9)} \\ \Delta P_{(8,9)} \end{bmatrix} = \begin{bmatrix} M_{11} & M_{12} & M_{13} & M_{14} \\ M_{21} & M_{22} & M_{23} & M_{24} \\ M_{31} & M_{32} & M_{33} & M_{34} \\ M_{41} & M_{42} & M_{43} & M_{44} \\ M_{51} & M_{52} & M_{53} & M_{54} \\ M_{61} & M_{62} & M_{63} & M_{64} \\ M_{71} & M_{72} & M_{73} & M_{74} \\ M_{81} & M_{82} & M_{83} & M_{84} \end{bmatrix} \begin{bmatrix} \Delta P_2 \\ \Delta P \\ \Delta P_4 \\ \Delta P_5 \end{bmatrix} \quad (5.21)$$

From (5.21) one can see that there are nine known (left) and four unknown (right) variables. This implies that the power flows on only four out of nine branches can be controlled at a time. Similar to the other cases, Case 2 and 3, the control strategy selects four branches with the highest required change in branch power for control.

Figure 5.11 shows some of the results when the proposed control strategy is applied on the system defined in Case 4 to control the disturbance in the system resulting from the integration WPPs into the system. Figure 5.11(a) shows the change in reference power that has to be made to fix the branch power flow violations in the system. The change in the reference power is made by the secondary controller only when necessary, which is used by the primary controllers. Observe that, for every change in reference powers in the system, there are corresponding changes in reference voltage of the system which is also used to update the reference voltages of the primary controllers. Figure 5.11b shows the annual duration curves of the controlled branch power flows in the system. Note that the branch power flows are controlled to the limiting values all the time during the year.

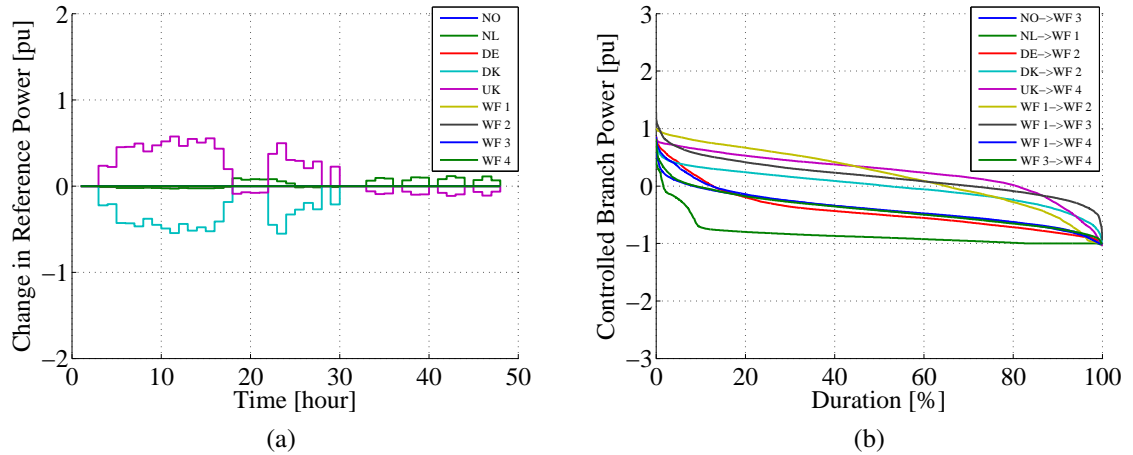


Figure 5.11: Case 4 simulation results: (a) change in reference power (b) annual duration curves of controlled branch power flows

5.3 Limit of controllability in the HVDC grids

As expected and was discussed in the preceding cases, not all the branch power flows in the system can be controlled at a time. For example, Case 2 has two branches and one controllable bus located at the Netherlands. Hence only one branch power can be controlled at a time. Case 3 has five branches and three controllable buses located at the Netherlands, Germany and Denmark. Hence, only three of the branches in the system can be controlled at a time. Similarly, Case 4 has nine branches and four controllable buses located at the Netherlands, Germany, Denmark and UK. Hence, only four branches in the system can be controlled at a time. From this, one can conclude that the number of controllable branch power flows in a given system at a given time is equal to the number of controllable bus powers in the system. As the number of controllable buses increase, so does the number of controllable branches and vice versa.

Since the number of controllable branch power flows in a system is equal to the number of controllable bus powers; in an HVDC grid with one or more loops and uncontrollable WPP buses; there is/are always branch power flows in the system that can not be controlled all the time. Hence, keeping the branch power flows in the system within the limiting values at the whole time require a careful choice of the WPP capacities in the system. In other words, the controllability of the grid at all times depends on the penetration level of the WPPs in the system. Table 5.2 shows the estimated maximum capacities of the WPPs that can be connected to the different cases defined in Chapter 3. Observe that these limiting WPP capacities are the values used to simulate all the three cases presented above.

Table 5.2: Estimated maximum WPP capacities that can be integrated into the system from controllability point of view

Estimated Maximum WPP capacities (MW)					
Cases	WF1	WF2	WF3	WF4	Total
Case 2	1700				1700
Case 3	1700	2700			4400
Case 4	1500	2000	1000	1500	6000

5.4 Voltage control in an HVDC grid

The need to control DC link voltage in an HVDC transmission grid is discussed in many literatures. The steady state analysis results made in this study shows that there might be no need to control the DC voltage in an HVDC grid to keep the voltage within the allowable range, say to $\pm 5\%$. In all the case studies presented above, the results show that the system voltages are way below the limiting values. Figure 5.12 shows the duration curve of the system bus voltage profiles when Case 4 is simulated with the WPPs. It can be seen from the figure that the system voltage varies close to the nominal value, 1 pu.

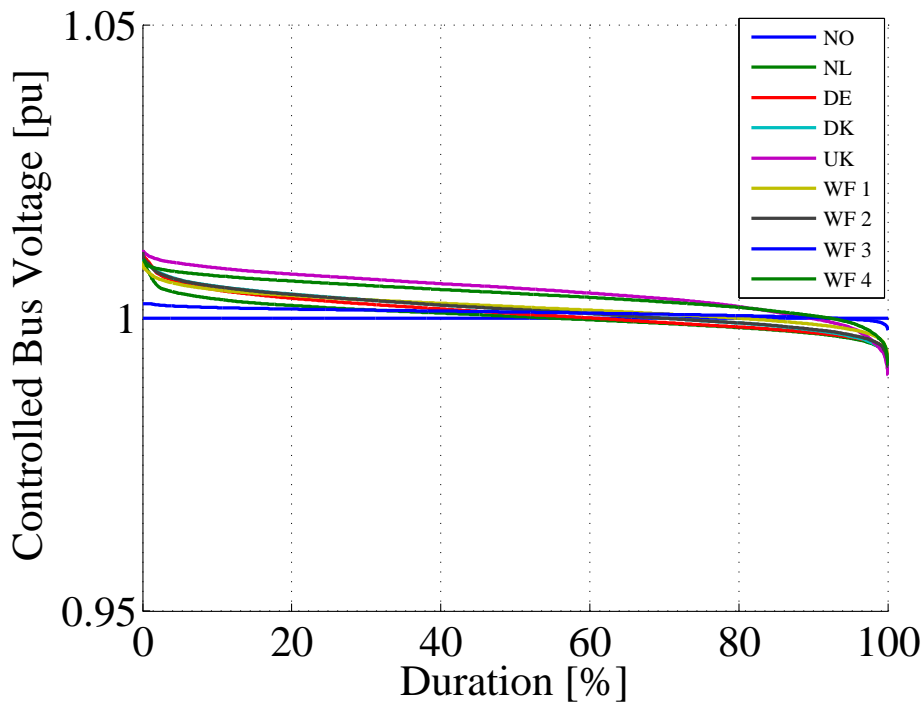


Figure 5.12: Annual duration curves of bus voltage profiles in an HVDC grid

Chapter 6

Economic analysis of HVDC grid in the North Sea

In this section, economic analysis of different scenarios of the HVDC grids in the North sea region, defined in Chapter 3, are presented. The main focus of the analysis is on the additional system costs associated with the integration of WPPs into the systems designed for power exchange. It is obvious that the integration of WPPs into the system alters the scheduled exchange power and hence results in additional costs to the system. On the other hand, the integration of WPPs into the system can be another source of revenue to the system which is generated by the transmission fee paid by the WPP operators and the savings that can be made by the reduced power loss in the system. By considering all main costs involved due to the integration WPPs into the system, the net added costs on the systems are studied. The results in all the studied cases showed that at lower WPP capacities, the system can gain from the integration of WPPs. As the penetration level of the WPPs increase, the added cost on the system increases steady. At higher WPP capacities, it is found out when reinforcing the system can reduce the added cost on the systems.

To get to the conclusions made above, certain procedures are followed. To calculate the investment cost of a system, the procedure described in Section 2.1.4 is utilized where the investment cost of a system is composed of cost of transmission cables, installation cost and cost of VSCs. Additionally, to calculate the cost of energy and transmission fee of the system, the data presented in Section 2.2.2 are used. In Section 2.2.2, it is stated that the average transmission fee (transmission tariff) in the North Sea region is about 10 € per MWh and the average cost of energy in the area is about 50 € per MWh.

By using these cost data, it is assumed that the system (this could be a TSO (Transmission System Operator) who owns the transmission system) pays for the change in the scheduled exchange power at a rate of 10 € per MWh. In addition, the system operator charges the WPP operators a transmission fee of 10 €. Furthermore, the system also gain the benefit obtained from the reduction in power loss due to the integration of WPPs in many cases where the cost in power loss is calculated at a rate of 50 € per MWh. Observe that the net added cost on the system, resulting from the integration of WPPs, is the sum of the three costs stated.

In order to make a proper investment decisions based on the costs stated above, NPV calculation, presented in Section 2.2.2, is used. In all NPV calculation in this chapter, an interest rate of 5% and an investment period of 30 years are assumed. The added cost on the system can be reduced by reinforcing the system. Reinforcing the system could be feasible if the added cost of the system after reinforcement is less than the added cost of the system before reinforcement.

6.1 Case 1

6.1.1 Investment cost

Recall that the system defined in Case 1 does not have WPPs. It is assumed to be used for power exchange between two regions in Norway and the Netherlands. In order to use it as a basis for the following cases, estimated investment cost of this system and cost of power loss in the system are presented in this section. Table 6.1 shows the total investment cost of the system and different cost elements making up the total investment cost, which is calculated based on the procedure presented in Section 2.1.4.. Observe that the cost of the cable is the dominant cost of the system which accounts for about 45% of the total cost. Similarly, the installation cost is comes second with about 30% of the total cost. The cost of the VSC accounts for the remaining 25% of the total system cost.

Table 6.1: Investment cost of the system in Case 1

	Cable	Installation	VSC	Total
Cost (M €)	494	350	279	1123

In order to make a rough check on the reliability of the procedure used to calculate investment costs in this study, a small analysis is made using the real investment cost of the NorNed project [41]. Observe that the system defined in Case 1 is similar to the NorNed HVDC transmission system, for instance regarding the length of the cable. According to [41], the NorNed HVDC link is built based on CSC technology [41]. It is ± 450 kV, 700 MW and 580 km long HVDC link and its cost is 600 M€ [21] where as the voltage and the power ratings of the system in Case 1 are ± 320 kV and 943 MW respectively. If the NorNed system were built using VSC HVDC technology, the estimated cost of the system would be as shown in Table 6.2.

Table 6.2: Estimated investment cost of NorNed if it were built using VSC HVDC

	Cable	Installation	VSC	Total
Cost (M €)	400	350	172	922

Observe that the total cost of the system in Table 6.2 is higher than the real cost of the NorNed project which is 600 M€. One of the reasons for the difference could be the technology used. According to [66], the investment cost of VSC HVDC transmission system is about 1.5 times higher than the cost of CSC HVDC. If this factor is taken into

account and the real cost of NorNed is multiplied by a factor 1.5 to compensate for the change in technology, the cost of the equivalent VSC HVDC transmission system is about 900 M€ which is close to the estimated total system cost using the procedure above. The other reasons for the difference could be inflation, the change in the cost of materials and similar costs related factors. Hence, taking this into account, the procedure adapted in this study to calculate the investment cost of the system is considered sufficient.

6.1.2 Transmitted power and power loss

The annual power loss of the system in Case 1 is about 0.05 TWh, which is about 0.8% of the annual transmitted power (6 TWh). The annual cost of power loss in this system is about 2.3 M€, which is about 3.8% of annual revenue from the transmission tariff. The NPV of the cost of power loss over the investment period is about 34 M€ which can be compared with the NPV of the revenue from power transmission tariff which is about 921 M€.

Observe that the NPV of the revenue generated from power transmission (921 M€) is less than the total investment cost of the system shown in Table 6.1 (1122.5 M€). This means that the investment cannot be recovered in 30 years if 10 € per MWh is used as a transmission fee. In order to recover the investment during 30 years from the revenue obtained from power transmission, the transmission fee has to be at least 13 € per MWh. If this transmission fee is used, the NPV of the revenue generated from power transmission will be about 1197 M€ which is enough to recover the investment cost of the system. In this case, the cost of power loss becomes about 3% of the transmission fee.

Note that the economic benefit is not the only driver for the construction of the NorNed HVDC link, for example. The need to have security of power supply between the countries is another driver. Hence, it can be assumed that there is a benefit that can be converted into economic terms as a result of an increased security of supply that this system provides. Taking this into account, 10 € per MWh is considered as a transmission fee for all of the following case studies and the investment cost which is not covered by the revenue from the transmission fee is assumed to be covered by the system stakeholders.

6.2 Case 2

6.2.1 Investment cost, base case

The system in Case 2 is the system in Case 1 with a WPP. If the cost of integrating the WPP into the system is excluded, the investment cost of the system in Case 2 is the same as the investment cost of the system in Case 1.

6.2.2 Effect of the WPP on the scheduled exchange power

As stated before, the system is designed to transport the scheduled exchange power between two locations in Norway and the Netherlands. When the WPP with non-zero capacity is integrated into this system, it causes change in the scheduled exchange power. Recall that the maximum WPP capacity that can be integrated into this system is 1700 MW. In this section, the impact of the integration of the WPP with 20%, 40%, 60%, 80% and 100% of the maximum WPP capacity on the change of the scheduled exchange power is presented.

Figure 6.1 shows the change in the scheduled exchange power and the NPV of the change in the scheduled exchange during 30 years. Figure 6.1(a) shows the annual change in the scheduled exchange power and Figure 6.1(b) shows the NPV of the change in the scheduled exchange power. Obviously, the change in scheduled exchange power and the resulting NPV of the change in scheduled exchange power increase as the capacity of the WPP increases. Note that the total annual exchange power of the system is about 12 TWh.

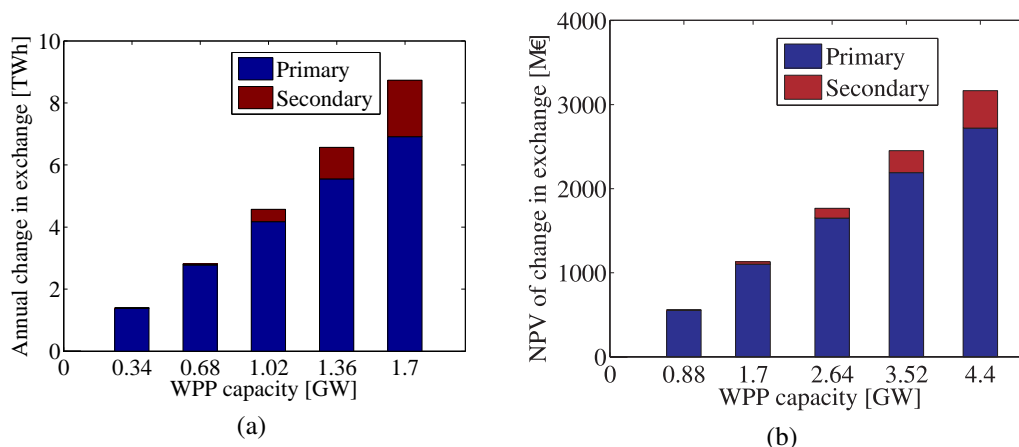


Figure 6.1: Effect of WPP connection on (a) the change in the scheduled exchange power (b) the NPV of change in scheduled exchange power for a unit cost of 10 €/MWh, during 30 years and 5% discount rate

Recall that the change in the scheduled exchange power can be due to the action of the local primary controller and the central secondary controller. The local droop controller acts to share the power from the added WPP and the central controller acts when there is a violation of branch power flows in the system due to the added WPP. Note from Figure 6.1 that it is the primary controller that results in much of the change in the scheduled exchange power and hence the associated cost of change in the schedule. The change in schedule resulting from the action of the secondary controller and hence the cost is smaller and it happens only when the WPP capacity is 60%, 80% and 100% of the maximum WPP capacity.

As demonstrated in Figure 6.1, a large percentage of the change in the scheduled exchange power results from the action of the primary controller. Recall that the cost of change in the scheduled exchange power is paid by the system operator. The NPV of this cost varies from about 214 M€ when the WPP capacity is 20% to about 1342 M€ when

the WPP capacity is 100%. Recall also that the WPP operator pays a transmission fee of 10 €/MWh to the system operator. Figure 6.2 shows the variation of the WPP energy injected into the system and the corresponding NPV of the transmission fee paid for the system operator. Note that the transmission fee varies from about 213 M€ when the WPP capacity is 20% to about 1060 M€ when the WPP capacity is 100%. Observe that the majority of the costs resulting from the change in the scheduled exchange power can be compensated for by the transmission fee paid by the WPP operator. This can also be seen in Figure 6.1(b) and Figure 6.2(b).

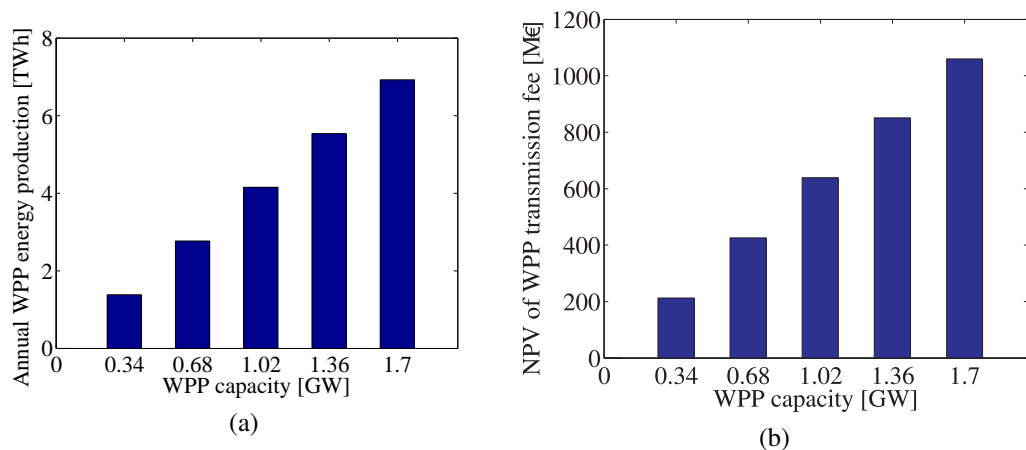


Figure 6.2: (a) Annual WPP energy production (b) NPV of WPP transmission tariff for a unit transmission tariff of 10 €/MWh, during 30 years and 5% discount rate

6.2.3 Effect of the WPP on power loss

The integration of WPP into the system in this case can reduce the power loss in the system. Figure 6.3 shows the annual system power loss and the NPV of the system power loss as a function of WPP capacities. Figure 6.3(a) shows the variation of the annual system power loss as a function of WPP capacities and Figure 6.3(b) shows the variation of the NPV of the system power loss as a function of WPP capacities. Observe from Figure 6.3 that the annual system power loss and the NPV of the system power loss decreases as the WPP capacity increases and reaches minimum values when the WPP is at 1.02 GW which is close to the rated capacity of the transmission cable. When the capacity of the WPP exceeds this value, the loss in the system start to increase. This is because the power has to flow a longer distance as the capacity of the added WPP increases beyond this value. Although the annual system power loss and the NPV of the system power loss has a tendency to increase after this value of WPP capacity, the annual system power loss and the NPV of the system power loss at the maximum WPP capacity is still less than the base case values, when the WPP capacity is zero. From this, it can be concluded that having any level of WPP in this system always decreases the system power loss and the system power loss is minimum when the capacity of the WPP is close to the rating of the transmission cable. Note also that the power loss in the system, seen from Figure 6.3(a), at zero WPP capacity is the same as the power loss observed in Case 1.

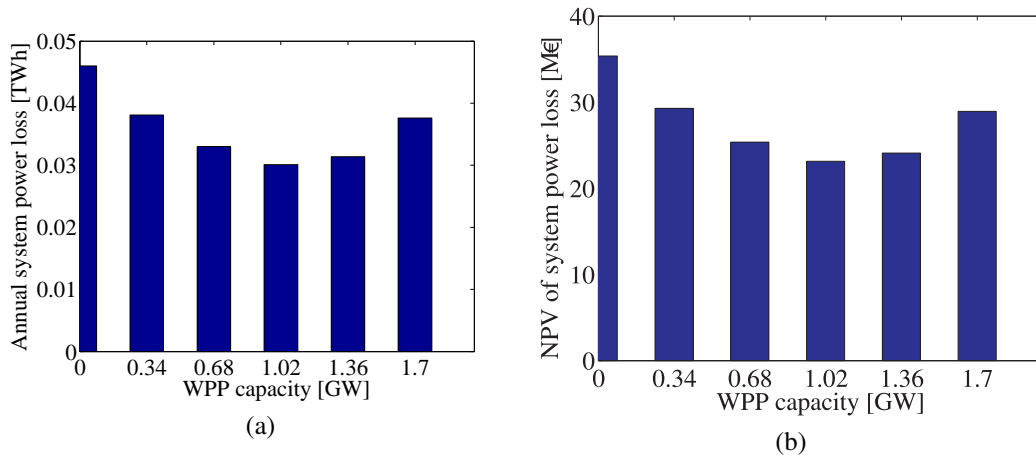


Figure 6.3: Effect of WPP connection on (a) annual system power loss (b) NPV of system power loss for a unit cost of 50€/MWh, during 30 years and 5% discount rate

6.2.4 Effect of the WPP on added cost

As can be seen in Figure 6.1(b), Figure 6.2(b) and Figure 6.3(b), the integration of the WPP into the system causes variation of operation costs. The system operator has to pay the cost of altering the scheduled exchange power due the integration of the WPP. On the other hand, the revenue generated by the reduced cost of loss and the transmission tariff paid by the WPP operator can be considered as an income to the system operator. In order to know the net additional cost that has to be paid by the system operator, all the costs have to be combined. Based on the net added cost, which from now on is referred to as added cost, an investment decision can be made on whether to reinforce the system or not. The added cost on the system can be calculated as

$$Added_Cost = C_1 + C_2 - C_3 \quad (6.1)$$

where $Added_Cost$ is the net added operation cost of the system, C_1 is the cost of change in the scheduled exchange power, C_2 is the change in cost of power loss which is calculated by subtracting the cost before from the cost after the integration of WPP and C_3 is the transmission tariff paid by the WPP operator.

Figure 6.4(a) shows the variation of the NPV of the system added cost when the transmission fee paid by the WPP operator is 10€ per MWh. The results in the figure show that the added costs on the system are negative for the WPP capacities of 0.34 GW (about -5 M€) and 0.68 GW (about -3.2 M€). This means that, at those WPP capacities, the system operator can gain by having the WPP in the system. As the capacity of the WPP increases above 0.68 GW, the added cost becomes positive and increases steadily. Observe that the result in Figure 6.4(a) depends on the assumed transmission fee paid by the WPP (10 €/MWh) and the cost of altering or changing the scheduled exchange power (10 €/MWh). If the costs are different and the transmission fee as well as the cost of changing the scheduled exchange are kept the same, then the results in Figure 6.4(a) are not affected. But, if the cost of changing the scheduled exchange is fixed to 10 €/MWh and the trans-

mission fee paid by the WPP is increased, which is the most likely case, then the results in Figure 6.4(a) change completely. Figure 6.4(b) shows the added costs on the system for different transmission tariff ([10, 13, 18] €/MWh) paid by the WPP operators while the cost of altering the scheduled exchange power is fixed to 10 €/MWh. Recall that, to recover the investment cost of this system, the minimum transmission tariff should be at least 13 €/MWh. Hence, in this case, if WPP operators are asked to pay this amount, the system operator can benefit at all levels of WPP integration in the system, since the added cost on the system is negative all the time, as can be seen from Figure 6.4b. Figure 6.4b also shows that as the transmission tariff paid by the WPP is increased to 18 € per MWh, the gain by the system operator increases more, getting up to 600 M€, which is about 53% of the total investment cost of the system.

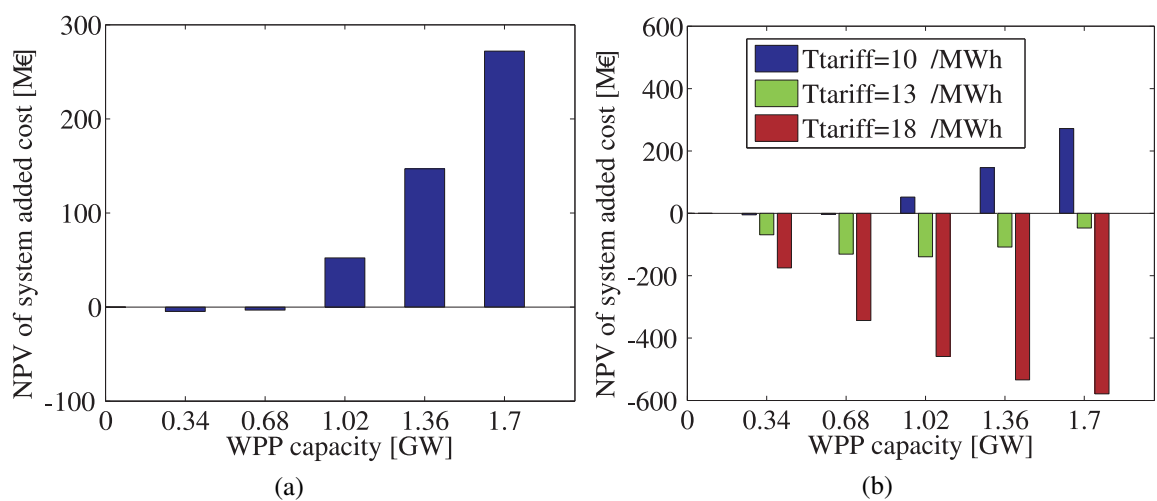


Figure 6.4: NPV of added cost of the system when (a) cost of change in exchange power and transmission tariff are the same (10 €/MWh) (b) cost of change in exchange power is 10 €/MWh and transmission tariffs are [10, 13, 18] €/MWh, during 30 years and 5% discount rate

6.2.5 Analysis of system reinforcement

As shown in Figure 6.4(a), the added cost on the system increases as the capacity of the WPP increases. This added cost gets up to about 272 M€ when the WPP capacity is 1.7 GW, which is a substantial cost. An interesting question here is if the added cost can be reduced by reinforcing the system which is the main point of this sub-section. An important step to reinforce the system is to choose the appropriate branch to reinforce. By looking at the change in branch power flows in the system, the appropriate branch to be reinforced can be chosen. Figure 6.5 shows the change in branch power flows in the system as a function of WPP capacities. The figure shows that the annual change in branch power on branch $NL \rightarrow WF1$ is the highest and can be considered as a first choice for reinforcement. Reinforcing branch $NO \rightarrow WF1$ may not be considered as an option at all levels of WPP capacities.

Figure 6.6 shows the added cost on the system when either of the branches ($NO \rightarrow WF1$ or $NL \rightarrow WF1$) is reinforced by using a cable with a rating of 216 MW (which is

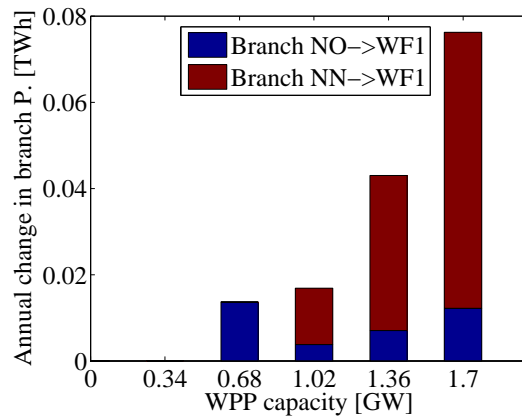


Figure 6.5: Effect of WPP connection on annual change in branch power flows

the smallest cable in Table 2.4). Recall that the rating of the cable in the base case is 943 MW and when reinforced, the rating of the cables become 1159 MW.

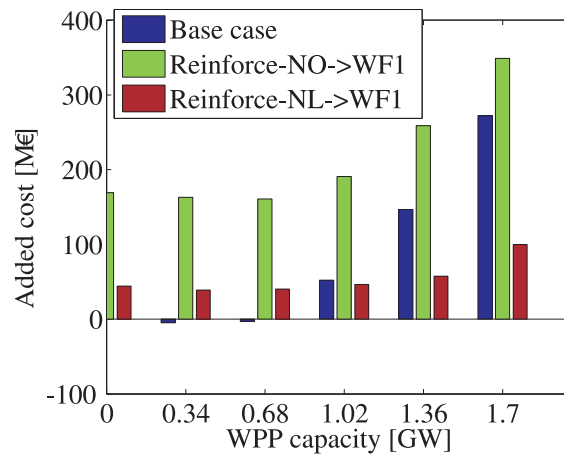


Figure 6.6: Effect of cable reinforcement on the NPV of system added cost, when the cost of change exchange power and WPP transmission tariff are the same (10 €/MWh), during 30 years and 5% discount rate. The reinforcement is made using a cable with a rating of 216 MW.

As it is evident from Figure 6.6, reinforcing branch $NO - WF1$ results in an increased added cost on the system for all WPP capacities, as can be seen from Figure 6.6. This supports the claim made before that reinforcing branch $NO - > WF1$ is not an economical option. On the other hand, reinforcing branch $NL - > WF1$ could be an option for some WPP capacities. For example, when the WPP capacities are 0.34 GW and 0.68 GW, reinforcing the branch results in higher added cost than the base case and accordingly does not reduce the system added cost. When the WPP capacity is 1.02 GW, the reinforced system results in almost the same added cost compared with the base case. Accordingly, for non-economic benefits what the integration of the WPP can provide, an appropriate decision can be made. When the WPP capacities are 1.36 GW and 1.7 GW, reinforcing branch $NL - > WF1$ results in much lower added cost compared with the base case system. Observe that the analysis on reinforcement is made by using a transmission tariff of 10 € per MWh. If a higher fee is paid by the WPP operator, the advantage for the system operator will be higher at these WPP capacities.

At this point, it has become clear that by reinforcing branch $NL \rightarrow WF1$, the added cost on the system can be reduced by up to 71% (250 M€ reduction) when the WPP capacity is 1.7 GW. This is achieved by reinforcing the base transmission system by using a cable with a rating of 216 MW. An interesting question at this point is to ask if the added cost can be further reduced by using a cable with an even higher rating for reinforcement. Figure 6.7 shows that reinforcing branch $NL \rightarrow WF1$ with higher cable rating can indeed reduce the added cost on the system further. For example, observe that using a cable with a rating of 317 MW produces a better result than using a cable with a rating of 216 MW. However, as the cable rating is increased from 317 MW to 490 MW, the advantage reduces as can be seen from the figure.

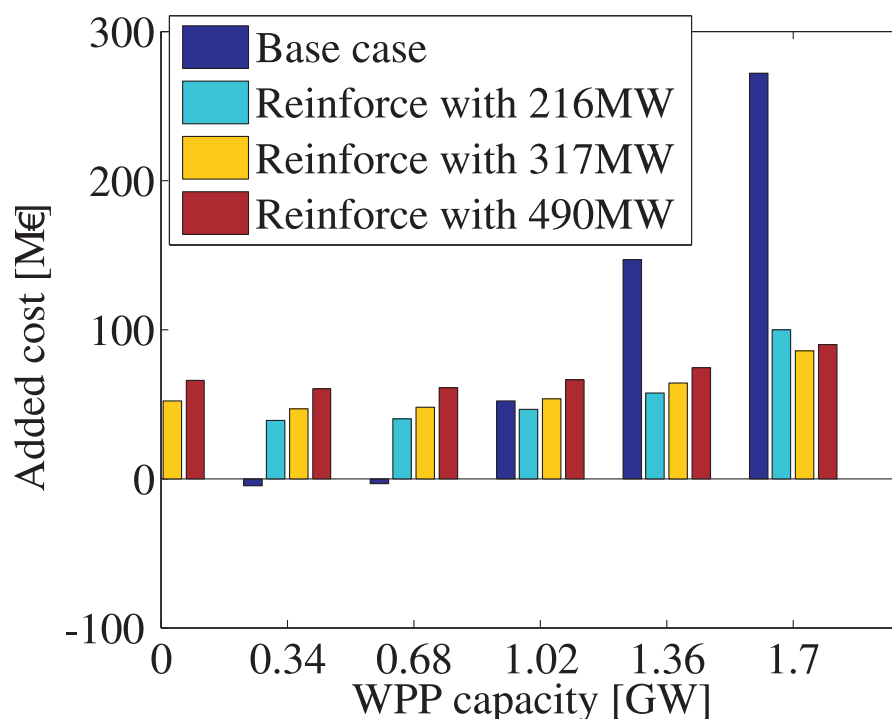


Figure 6.7: Effect of reinforcing branch $NL \rightarrow WF1$ with different cables on the NPV of system added cost, when the cost of change exchange power and WPP transmission tariff are the same (10 €/MWh), during 30 years and 5% discount rate

6.3 Case 3

As defined in Chapter 3, the system in this case is a six bus system that interconnects Norway, the Netherlands, Germany, Denmark and two offshore WPPs, WF 1 and WF 2. The WPPs have maximum WPP capacities of 1700 MW and 2700 MW respectively. In the following analysis, different percentages of the maximum WPP capacities are used to represent different scenarios.

6.3.1 Investment cost of the base system

Similar to Case 1 and 2, the investment cost of the system in Case 3 is composed of the cost of cables, installation cost and the cost of the VSCs. Table 6.3 shows the total investment cost and different elements of the total cost. As can be seen from the table, the cost of the cable is about 52% of the total cost, installation cost is about 20% of the total cost and the cost of the VSCs is about 28% of the total cost.

Table 6.3: Estimated investment cost of the system in Case 3

	Cable	Installation	VSC	Total
Cost (M €)	1321	501	734	2556

Observe in Table 6.3 that the installation cost in this case is 20% of the total cost while it is 30% of the total cost in Case 1 and 2. Recall from Section 2.1.4 that one of the reasons for the wide variation of installation cost is the number of cables in a branch. Since an average unit installation cost of 604 € per meter is assumed in this study, the same value is used irrespective of the rating or the configuration of the cables. This explains why the installation cost is 20% of the total investment cost in this case while it is 30% of the total cost in Case 1 and 2.

6.3.2 Effect of the WPPs on the scheduled exchange power

Similar to the system in Case 2, the system in Case 3 is also built for power exchange. Recall also that the system in this case has two WPPs, *WF1* and *WF2*. As discussed in Chapter 3, each WPPs can have maximum capacities of 1700 MW and 2700 MW respectively with a total capacity of 4400 MW. When the capacities of the WPPs in the system are non-zero, the scheduled exchange powers in the system has to change to accommodate the power from the added WPPs. As discussed before, the change in the scheduled exchange power can occur at two stages. The first stage is carried out by the local primary controllers. The change at this stage happens all the time as long as the WPP capacity in the system is non-zero. This stage makes sure that the added power from the WPPs are shared by the external grids connected to the system. The second stage is carried out by the central secondary controller. This action is activated only when branch power flows in the system exceed limiting values of the branch cables.

To investigate the impact of the added WPPs on the scheduled exchange power, different percentages (0%, 20%, 40%, 60%, 80% and 100%) of the maximum total WPP capacities are considered for simulation. Figure 6.8 shows the variation of the scheduled exchange power and the NPV of the cost of the change in the scheduled exchange power as a function of the WPP capacities. Figure 6.8(a) shows the variation of the annual change in the scheduled exchange power as a function of the WPP capacities. Figure 6.8(b) shows the variation of the NPV of the cost of the change in the scheduled exchange power as a function of the WPP capacities. Observe from Figure 6.8 that, similar to the result in Case 2, the action of the primary controller is far greater than the action of the secondary controller. It can also be seen that the secondary controller acts only when required.

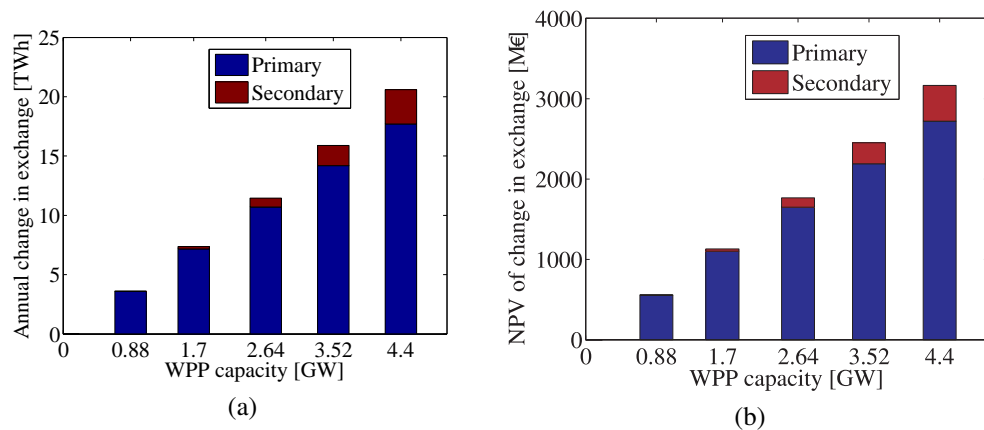


Figure 6.8: Effect of WPP connection on (a) the change in the scheduled exchange power (b) the NPV of change in scheduled exchange power for a unit cost of 10 €/MWh, during 30 years and 5% discount rate

To have an idea of how big the change in the scheduled exchange is, compared to the base scheduled exchange, a calculation is made and it is observed that when the WPP capacity is 20% of the of the maximum WPP capacity, the change in the scheduled exchange power is about 12% of the scheduled exchange power. Similarly, when the WPP capacity is 40%, the change in the scheduled exchange is about 23% of the actual exchange; when the WPP capacity is 60%, the change in schedule is about 37% of the actual schedule; when the WPP capacity is 80%, the change in schedule is about 51% of the actual schedule and when the WPP capacity is 100%, the change in schedule is about 66%; for the case considered.

Observe from Figure 6.8(b) that the cost of change in the scheduled exchange power is substantial, which gets up to about 3 billion € in this case. The value of integrating the WPPs in to the system should be comparable with this cost. Recall that the WPPs pay a transmission fee for the system operator, which can cover a large percentage (about 87% when WPP capacities are 100% and 80%) of this cost. Figure 6.9 shows the variation of

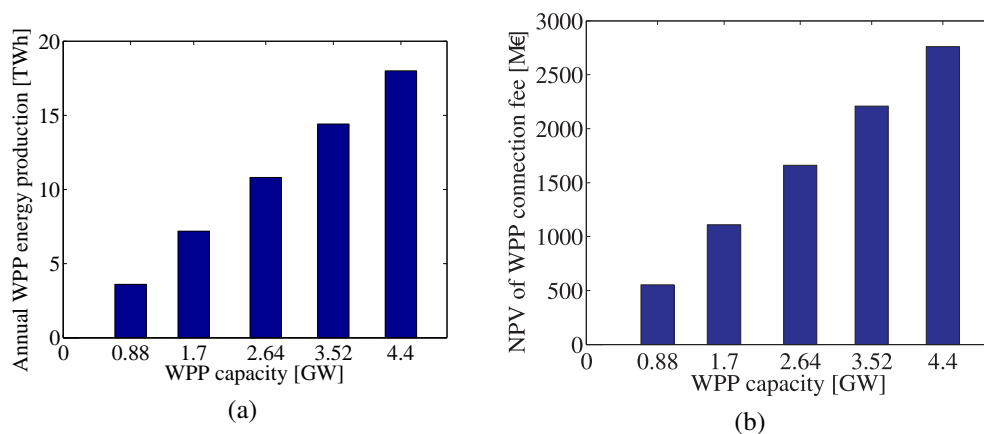


Figure 6.9: (a) Annual WPP energy production (b) NPV of WPP transmission tariff for a unit transmission tariff of 10 €/MWh, during 30 years and 5% discount rate

annual energy from the WPPs and the NPV of the transmission fee from the WPPs as a function of WPP capacity. Figure 6.9(a) shows the annual energy from the WPPs as a function of WPP capacities. Note that this result can be compared with the result from the action of the primary controller shown in Figure 6.8(a). Figure 6.9(b) shows the NPV of the transmission fee paid by the WPPs as a function of WPP capacity. Observe that the transmission fee can pay much of the cost resulting from the change in scheduled exchange power shown in Figure 6.8(b).

6.3.3 Effect of the WPPs on power loss

Figure 6.10 shows the variation of power loss and NPV of the cost of power loss in the system as a function of WPP capacity. Figure 6.10(a) shows the annual power loss in the system as a function of WPP capacity. Note that as the WPP capacity increases, the power loss in the system decreases getting to the minimum when the WPP capacity is maximum. Having the WPP at 100% capacity, for example, can reduce the system loss by about 39% in this case. Similar to the result in Case 2, the integration of WPP into this system decreases the power loss in the system. Figure 6.10(b) shows the variation of the NPV of the cost of power loss in the system. The result shows that as the WPP capacity increases, the NPV of the cost of power loss decreases which is an advantage for the system. The advantage gained by the reduced cost of power loss in the system can be used to pay some of the system cost resulting from the change in the scheduled exchange power.

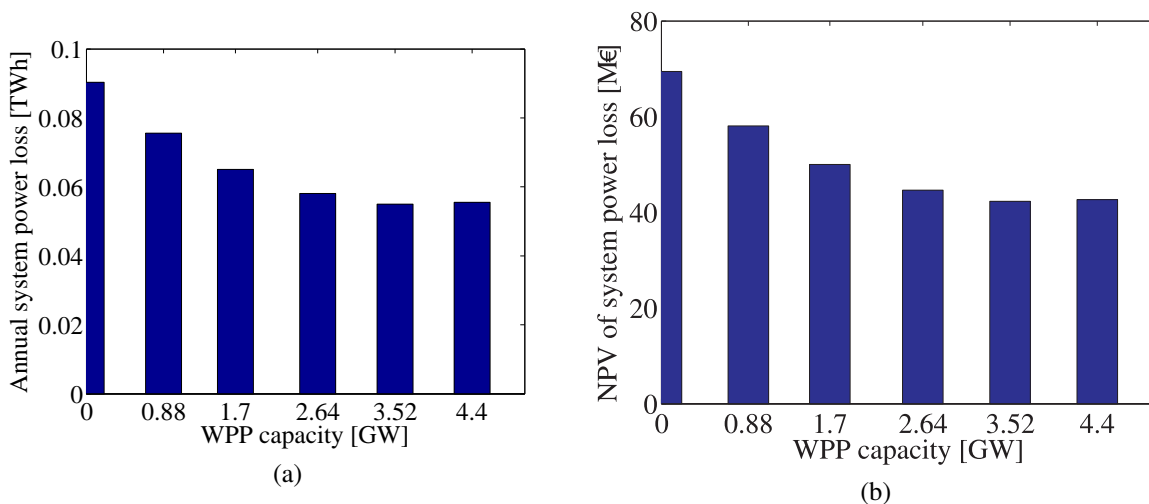


Figure 6.10: Effect of WPP connection on (a) annual system power loss (b) NPV of system power loss for a unit cost of 50 €/MWh, during 30 years and 5% discount rate

Observe that, in contrast to the results in Figure 6.3, the results in Figure 6.10 show that the power loss and hence the cost of power loss in the system has the tendency to remain constant when the total WPP capacity of the system is greater than 2.64 GW, which is 60% of the total maximum WPP capacity. This could be due to the topology of the system.

6.3.4 Effect of the WPPs added cost

As described above, while the cost of the change in the scheduled exchange power can be seen as an extra cost that has to be paid by the system operator; the transmission fee from the WPPs and the reduction in the cost of power loss due to the integration of the WPPs can be seen as an advantage and extra gain by the system operator.

Hence, in order to calculate the net added cost on the system due to the integration of the WPPs, the transmission fee and the reduction in the cost of loss has to be deducted from the cost of change in the scheduled exchange power, the formula of which is presented in (6.1). Figure 6.11 shows the net added cost on the system resulting from the integration of WPPs into the system. Note from the figure that when the total WPP capacity is 0.88 GW, the net added cost on the system is negative, about -8M€. This means that about 8 M€ can be gained by the system by just having the WPPs with this capacity in the system. As the capacity of the WPPs increases, the net added cost on the system increases steadily getting up to about 379 M€. Observe that this result when a transmission tariff of 10 €/MWh is considered for WPPs. If a higher transmission tariff is considered, the result would be different, more similar to the result in Figure 6.4(b).

Similar to the result in Case 2, by reinforcing some of the branches in this system, the net cost added on the system due to the integration of the WPPs can be reduced, which is addressed in the following section.

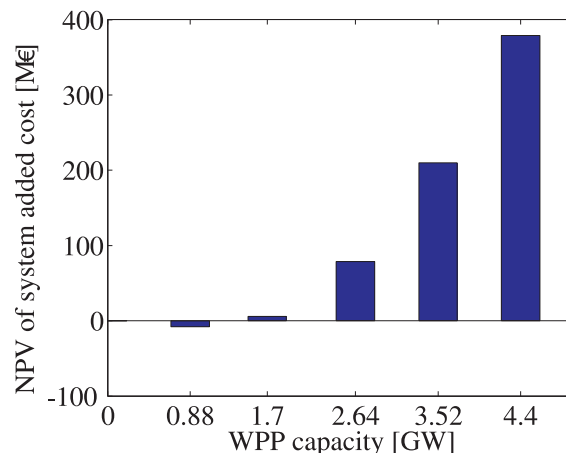


Figure 6.11: NPV of added cost on the system when a unit cost of change in exchange power and transmission tariff of the WPPs are the same (10 €/MWh), during 30 years and 5% discount rate

6.3.5 Analysis of system reinforcement

As discussed in Section 6.2.5, the first step to reinforce a system is to choose a branch to reinforce. It is indicated, for a proper choice of the branch to reinforce, a good information can be obtained by looking at how often the branch power flows in the system are limited. In addition, the result in the same section also showed that by reinforcing the branch with the highest branch power flow limitation, a good result can be achieved, which is as expected.

Figure 6.12 shows the branch power flow limitation in the system during a year. The result shows that branch power flow limitations are done quit often on three of the branches out of five branches in the system. From the result, it seems that the highest limitation is made on branch $NL \rightarrow WF1$, which is followed by the branch $WF1 \rightarrow WF2$ and then followed by the branch $NO \rightarrow WF1$. Hence, the impact of reinforcing these three branches on the net added cost of the system investigated.

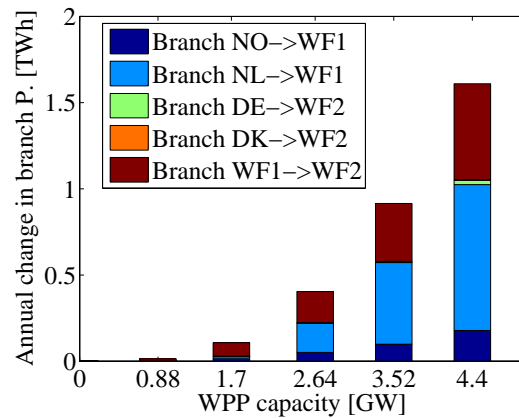


Figure 6.12: Effect of WPP connection on annual change in branch power flows

Figure 6.13 shows the impact of system reinforcement on the added cost of the system. The results represent when the three candidate branches ($NL \rightarrow WF1$, $WF1 \rightarrow WF2$ and $NO \rightarrow WF1$) are reinforced one at a time by using a cable with a rating of 216 MW, from Table 2.4. As indicated above and as discussed in Section 6.2.5, reinforcing branch $NL \rightarrow WF1$ results in the least net added cost on the system all the time, irrespective of WPP capacity. Then reinforcing $WF1 \rightarrow WF2$ comes next and reinforcing $NO \rightarrow WF1$ comes last. In addition, the results in Figure 6.13 also show that reinforcing the system when the total WPP capacity is less than or equal to 1.7 GW results in increased added cost compared to the base case. And hence, reinforcing the system for this WPP

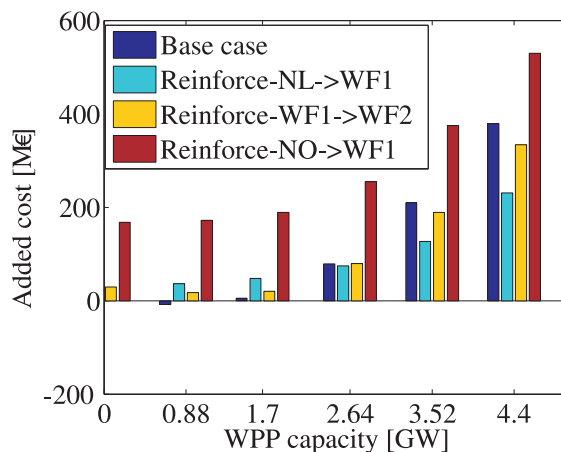


Figure 6.13: Effect of cable reinforcement on the NPV of system added cost, when the cost of change exchange power and WPP transmission tariff are the same (10 €/MWh), during 30 years and 5% discount rate. The reinforcement is made using a cable with a rating of 216 MW.

capacity does not have an economic advantage. However, when the total WPP capacity is

2.64 GW, reinforcing branch $NL- > WF1$ or $WF1- > WF2$ may have an economic advantage. The results obtained by reinforcing both branches are close to the base case value. For example, if branch $NL- > WF1$ is reinforced, a reduction of about 4 M€ in the net added cost of the system can be achieved. If branch $WF1- > WF2$ is reinforced at this WPP capacity, the added cost on the system increases by about 0.7 M€. Based on these results, appropriate decision can be taken for the given WPP capacity.

In addition, from Figure 6.13 it can be seen that, for a total WPP capacity of 3.52 GW and 4.4 GW, reinforcing either branch $NL- > WF1$ or branch $WF1- > WF2$ has an economic advantage for the system since it can reduce the net added cost on the system. Moreover, reinforcing branch $NL- > WF1$ produces the best result. Note that the analysis made in Figure 6.13 is by reinforcing either of the candidate branches with an additional cable having a rating of 216 MW. As discussed in Section 6.2.5 and presented in Figure 6.7, using a different cable rating for reinforcement can produce better results. Further analysis is left for future study.

6.4 Case 4

Similar to the systems in Case 2 and Case 3, the system in Case 4 is also built to transport scheduled power exchange. In this section, the estimate of the investment cost of this system is presented. The approach used to calculate the investment cost of the system is the same as that used in Case 1, 2 and 3. In addition, the impact of different levels of WPP capacities on different cost elements are also presented.

6.4.1 Investment cost of the system

Table 6.4 shows different elements of the investment costs of the system. From the table, it can be seen that the cost of the cables is about 61% of the total cost; the cost of installation is about 21% of the total cost and the remaining 18% of the total cost is the cost of VSCs. The composition of different investment cost elements in this case [61%, 21%, 18%] is comparable to the investment cost elements in Case 3 [52%, 20%, 18%]. The main difference is on the percentage of the cables and the VSC. The reason for this is that the system in Case 4 has more number of branches than the system in Case 3. That explains why the percentage of the share of the cable cost in Case 4 is higher than that in Case 3. The share of the installation cost in both cases is close to 20%.

Table 6.4: Investment cost of the system in Case 4

	Cable	Installation	VSC	Total
Cost (M€)	3083	1045	951	5079

6.4.2 Effect of the WPPs the scheduled exchange power

Similar to all the other cases discussed above, the integration of WPPs with non-zero WPP capacities results in a change of the scheduled exchange powers of the system. The action to change the scheduled exchange power is taken in two stages. The action at the first stage is taken by the local primary controllers. As discussed above, this action is taken all the time as long as there is a non-zero power from the WPPs. The action at the second stage is carried out by the central secondary controller. This action is taken only when the branch power flows in the system exceed the limiting values. Figure 6.14 shows the change of the scheduled exchange power and the NPV of the cost of change in the scheduled exchange power. Figure 6.14(a) shows the annual change in the scheduled

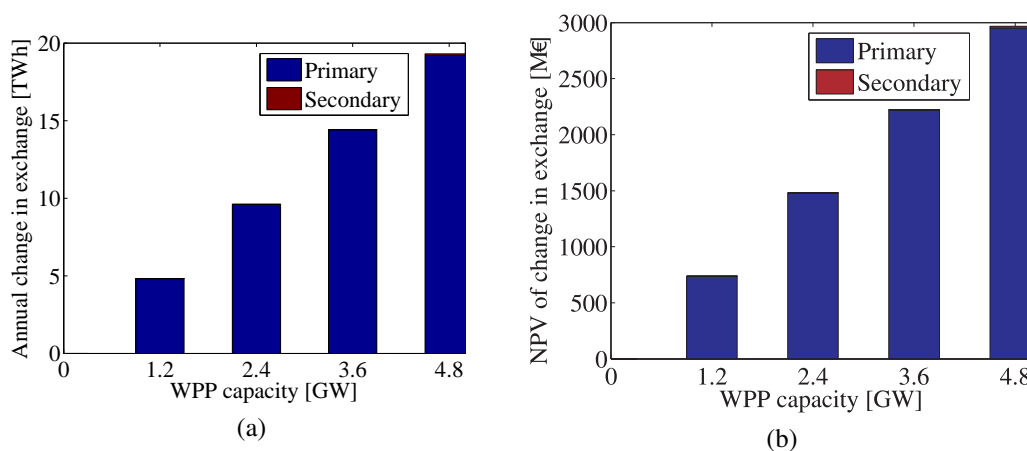


Figure 6.14: Effect of WPP connection on (a) the change in the scheduled exchange power (b) the NPV of change in scheduled exchange power for a unit cost of 10€/MWh, during 30 years and 5% discount rate

exchange power as a function of WPP capacity and Figure 6.14(b) shows the variation of the NPV of the change in the scheduled exchange power as a function of WPP capacity. As can be seen from the figures, as the total WPP capacity increases, the change in the scheduled exchange power and hence the cost of the change in the scheduled exchange power increases steadily. Similar to the results in Case 2 and 3, the results in Figure 6.14 show that the large percentage of the changes in the scheduled exchange power is made by the local primary controllers and only small percentage of the change is made by the central secondary controller only when needed.

As can be seen from Figure 6.14(b), the NPV of the cost of a change in the scheduled exchange power can get up to 3 billion € when the total WPP capacity is 6 GW. Large percentage of this cost can be covered by the connection fee paid by the WPP operator. Figure 6.15 shows the variation of power from the WPPs as a function of the total WPP capacity and the variation of the transmission fee paid by the WPPs as a function of the total WPP capacity. Figure 6.15(a) shows the annual variation of power from the WPPs and Figure 6.15(b) shows the variation of the NPV of the transmission fee paid by the WPP operator. Observe from Figure 6.15(b) that the transmission fee obtained from the WPPs can be used to pay the added system cost resulting from the cost of change in the scheduled

exchange power shown in Figure 6.14(b).

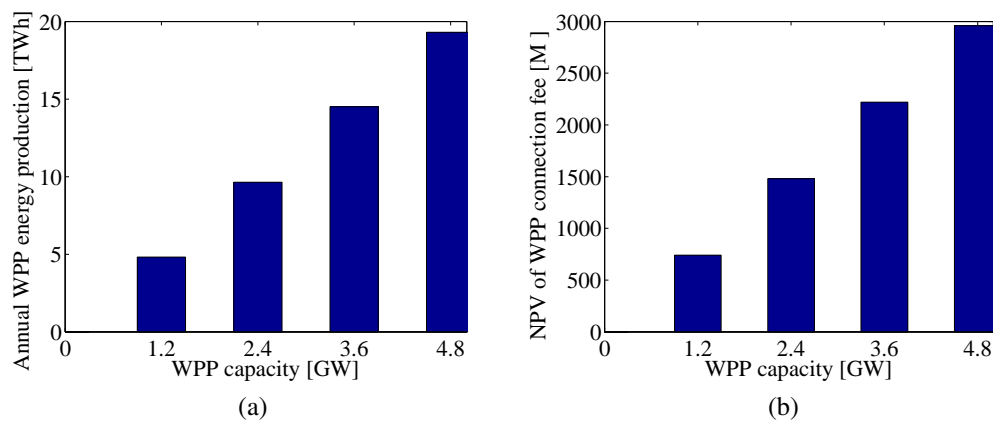


Figure 6.15: (a) Annual WPP energy production (b) NPV of WPP transmission tariff for a unit transmission tariff of 10 €/MWh, during 30 years and 5% discount rate

6.4.3 Effect of the WPPs power loss

Figure 6.16 shows the variation of power loss and the variation of the NPV of the power loss as a function of the total WPP capacity. Figure 6.16(a) shows the annual variation of system power loss and Figure 6.16(b) shows the variation of the NPV of the power loss as a function of total WPP capacity. Initially, as the total WPP capacity is increased from 0 to 1,2 GW, the power loss and hence the NPV of the power loss decreased. As the total WPP capacity is increased from 1.2 GW to a higher value, the system power loss and hence the NPV of the power loss increased steadily. The main reason for this is that the control system used in the simulation forces the power to flow longer distances so that the branch power flows are kept within the limits.

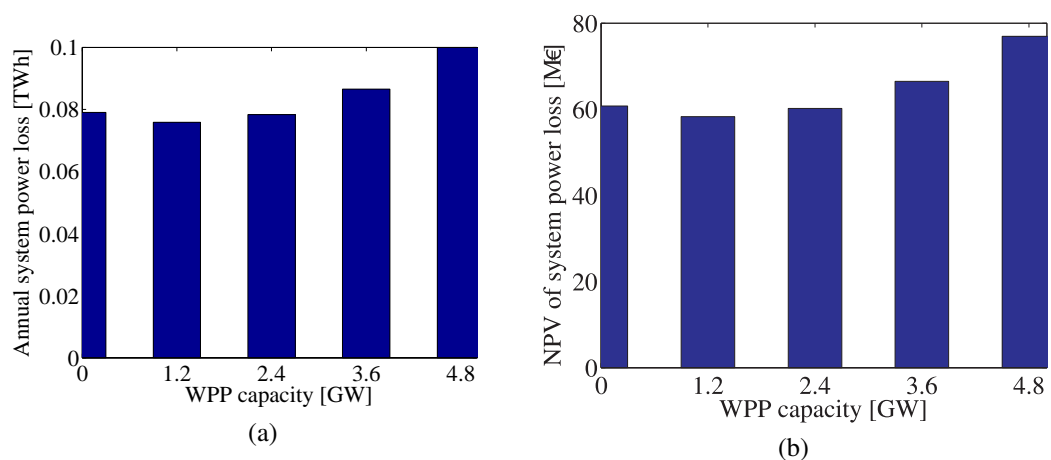


Figure 6.16: Effect of WPP connection on (a) annual system power loss (b) NPV of system power loss for a unit cost of 50 €/MWh, during 30 years and 5% discount rate

6.4.4 Effect of the WPPs added cost

Recall that the net added cost on the system depends on three main cost components. These are the cost of change in the scheduled exchange power, the transmission fee of WPPs and the cost of change in power loss. If the later two costs are deducted from the first cost, the net added cost on the system can be determined, as is also formulated in (6.1). Figure 6.17 shows the variation of the net added cost on the system as a function of total WPP capacity. Observe from the figure that when the total WPP capacities are 1.2 GW and 2.4 GW, the net added costs on the system are negative. This means that the system can benefit by having the WPPs. The benefit can get up to 4.2 M€. As the WPP capacity is increased from 2.4 GW onward, the net added cost becomes positive and increases steadily. The system can be reinforced to reduce the added cost on the system. The same procedure presented for Case 2 and 3 can be used to reinforce the system, the details of which is left for a future work.

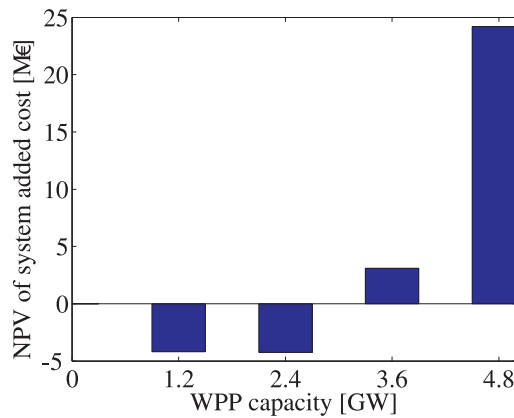


Figure 6.17: NPV of added cost on the system when a unit cost of change in exchange power and transmission tariff of the WPPs are the same (10 €/MWh), during 30 years and 5% discount rate

Chapter 7

Conclusions and Future Work

7.1 Conclusions

In this thesis, some of the technical and economical aspects of building or expanding HVDC grids in the North Sea are addressed. The expansion of the grids are made by integrating WPPs onto a system designed for power exchange. In all the studied cases, the systems are operated by using the proposed control strategy, which is local primary controllers followed by a central secondary controller. The primary controllers react to the added WPPs by changing the scheduled exchange power that they control according to their droop setting which in this thesis is assumed to be 3%. This is followed by the central supervisory controller only when there is a violation in branch power flow. When a branch power flow in the system exceeds the rating of the cable, the supervisory controller makes extra changes in the scheduled exchange power to keep the branch power flows within the cable ratings. From a technical point of view, it is demonstrated that the proposed control strategy can be used to enable the integration the WPPs onto a system designed for power exchange. However, the capacity of the WPP that can be connected to a system less than the theoretical maximum WPP capacity that can be connected to the system, which is a limitation of the proposed control strategy.

Moreover, from the performed economic analysis, it is observed that the system operator can gain from the integration of WPPs into a system designed for power exchange. The economic gain can vary depending upon the total capacity of the WPPs in the system, the transmission fee paid by the WPP operators and the cost paid for altering the scheduled exchange power due to the integration of WPPs. For instance, for the system studied in Case 2, it is observed that the economic gain varies from 5 M€ to 600 M€ which is about 0.5% to 53% of the total investment cost of the system. This is when the cost of altering the scheduled exchange is 10 €/MWh and the transmission tariff of the WPPs is 18 €/MWh. It is also observed that, for some of the cases considered, a significant economic gain can be achieved by reinforcing the system when the total WPP capacity in the system is higher than 60 % of the possible maximum WPP capacity that can be connected to the system. In

some cases, the economic gain was up to 20% of the total investment cost of the system.

Furthermore, an ARIMA based modelling procedure is used to simulate the power from the WPPs in the system. From the investigation made in the thesis, a modified ARIMA based modelling procedure is proposed which is based on decomposing a wind speed data into HF and LF components. In addition, for a 10 minute average wind speed data, the model structure ARIMA(6,0,0) can be used to model the HF component of the wind speed and LARIMA(0,1,6) can be used to model the LF component of the wind speed. In order to split the 10 minute average wind speed data into HF and LF frequency components, a cut off period of $T_{cutoff} = 4day$ can be used. Moreover, if measured wind speed data is not available and it is required to generate a 10 minute average wind speed data in the Baltic sea area with a given average wind speed, the model structure and the corresponding parameters given in Table 4.5 and 4.6 can be used to generate a wind speed time series data with a reasonable characteristics such as time correlation, probability distribution and periodic characteristics. The same model can also be applied to generate a similar wind speed data in the south east part of the North Sea areas with fairly good results. In order to model time and space correlated hourly average wind speed data in the North Sea area, the VARMA model structure, $VARMA(6, 0, 0)$ can be used. The appropriate transformation factor for the VARMA model lies between 0.5 to 1.5 and 0.9 can be considered as a first option while testing different transformation factors.

7.2 Future Work

Recall that the approach considered in the analysis based on the assumption that there is a transmission system built for power exchanges and WPPs are connected this system. In order to accommodate the added WPPs into the system, the system was operated by the proposed control strategy. This means that the direction of the power flows in the system are decided by the control strategy. However, this is just one way of looking at the problem. On the other hand, the integration the WPPs into a system could change the price of energy in the area and hence the scheduled exchange power in the system. Hence, it would be interesting to investigate the systems using a market model in the area which can dictate the direction of power flow in the system. Recall also that all the base case systems considered in this thesis are considered as if they were designed for power exchange only. The assumed expansion of the system was made by connecting the WPPs into the system. However, the expansion could also continue from a system which is used for both power exchange and WPPs. The other scenario is if the systems were designed from the beginning. By comparing the results from the different possibilities, a generalized recommendation for the design, operation and control of the system could be made; the task which can be considered in the future work.

In addition, the proposed control architecture in the thesis does not consider the optimization of the power flow in the system. Hence, it is interesting to develop the method further so that the optimum control of the system could be achieved. In addition, it is also interesting to compare the proposed control strategy with other control strategy, possibly inspired from an AC system (if any), which could all be considered in the future work.

Recall that, compared with the estimation of the cost of cables and the cost of VSCs, the estimation of the installation cost used to calculate the investment cost of the system is less reliable. This is due to the wide variation of the installation cost depending on many factors. Hence, considering a more reliable way of estimating the installation cost in the future work can add more value to the procedure used to calculate the investment cost of the system.

Finally, it is of great importance to investigate the dynamics of the systems discussed in this thesis from which grid codes of the system can be established. The result from the investigation can be used to design switch gear stations in the system, to set up grids for the dynamic operation of the system which all can contribute to build a reliable HVDC transmission grid.

Chapter 7. Conclusions and Future Work

References

- [1] L. Stankeviciute and P. Criqui, “Energy and climate policies to 2020: the impacts of the european 20/20/20 approach,” *International Journal of Energy Sector Management*, vol. 2, no. 2, pp. 252–273, Jun. 2008.
- [2] A. R. Henderson, C. Morgan, B. Smith, H. C. Sørensen, R. J. Barthelmie, and B. Boesmans, “Offshore wind energy in europe, a review of the state-of-the-art,” *Wind Energy*, vol. 6, no. 1, pp. 35–52, Jan. 2003.
- [3] G. Corbetta, A. Arapogianni, J. Moccia, and J. Wilkes, “The european offshore wind industry—key trends and statistics 2013,” *The European Wind Energy Association (EWEA)*, p. 6, 2014.
- [4] E. W. E. Association, *Pure Power - wind energy targets for 2020 and 2030*. EWEA, 2011.
- [5] M. H. Albadi and E. F. El-Saadany, “Overview of wind power intermittency impacts on power systems,” *Electric Power Systems Research*, vol. 80, no. 6, pp. 627–632, Jun. 2010.
- [6] P. S. Georgilakis, “Technical challenges associated with the integration of wind power into power systems,” *Renewable and Sustainable Energy Reviews*, vol. 12, no. 3, pp. 852–863, Apr. 2008.
- [7] CEPOS, “Wind energy: The case of denmark,” Tech. Rep., Sep. 2009.
- [8] A. Woyte, J. De Decker, and V. Van Thong, *A North Sea Electricity Grid [r] evolution: Electricity Output of Interconnected Offshore Wind Power: a Vision of Offshore Wind Power Integration*. Greenpeace, 2008.
- [9] H. Holttinen, P. Meibom, A. Orths, B. Lange, M. O’Malley, J. O. Tande, A. Estanqueiro, E. Gomez, L. Söder, G. Strbac, J. C. Smith, and F. van Hulle, “Impacts of large amounts of wind power on design and operation of power systems, results of IEA collaboration,” *Wind Energy*, vol. 14, no. 2, pp. 179–192, Mar. 2011.
- [10] E. W. E. Association *et al.*, *Large Scale Integration of Wind Energy in the European Power Supply: Analysis, Issues and Recommendations: a Report*. European Wind Energy Association, 2005.
- [11] S. Gordon, “Supergrid to the rescue,” *Power Engineer*, vol. 20, no. 5, pp. 30–33, Oct.

References

2006.

- [12] J. De Decker, P. Kreutzkamp, S. Cowdroy, L. Warland, J. Völker, J. Tambke *et al.*, “Offshore electricity grid infrastructure in europe,” *OffshoreGrid Final Report*, 2011.
- [13] I. M. de AlegrÃa, J. L. MartÃn, I. Kortabarria, J. Andreu, and P. I. Ereno, “Transmission alternatives for offshore electrical power,” *Renewable and Sustainable Energy Reviews*, vol. 13, no. 5, pp. 1027–1038, Jun. 2009.
- [14] N. Kirby, M. J. Lockett, L. Xu, and W. Siepman, “HVDC transmission for large offshore windfarms,” in *AC-DC Power Transmission, 2001. Seventh International Conference on (Conf. Publ. No. 485)*, Nov. 2001, pp. 162–168.
- [15] B. Van Eeckhout, D. Van Hertem, M. Reza, K. Srivastava, and R. Belmans, “Economic comparison of VSC HVDC and HVAC as transmission system for a 300 MW offshore wind farm,” *European Transactions on Electrical Power*, vol. 20, no. 5, pp. 661–671, Jul. 2010.
- [16] A. A. van der Meer, R. T. Pinto, M. Gibescu, P. Bauer, J. T. Pierik, F. D. Nieuwenhout, R. L. Hendriks, W. L. Kling, and G. A. van Kuik, “Offshore transnational grids in europe: the north sea transnational grid research project in relation to other research initiatives,” in *Proceedings of 9th International Workshop on Large-Scale Integration of Wind Power*, 2010, pp. 1–8.
- [17] N. S. C. G. Initiative, “Final report-grid configuration,” NSCOGI, Technical Report, November 2012.[Online]. Available: http://www.benelux.int/NSCOGI/NSCOGI_WG1_OffshoreGridReport.pdf, Tech. Rep., 2012.
- [18] J. Blau, “Europe plans a north sea grid,” *IEEE Spectrum*, vol. 47, no. 3, pp. 12–13, Mar. 2010.
- [19] T. Vrana, R. Torres-Olguin, B. Liu, and T. Haileselassie, “The north sea super grid - a technical perspective,” in *9th IET International Conference on AC and DC Power Transmission, 2010. ACDC*, Oct. 2010, pp. 1–5.
- [20] C. B.-. W. Group *et al.*, “Hvdc grid feasibility study,” Melbourne: International Council on Large Electric Systems, Tech. Rep., 2011.
- [21] Tannet, “The longest electricity cable in the world is operational,” <http://www.tennet.eu/nl/news/article/the-longest-electricity-cable-in-the-world-is-operational.html>, 2014.
- [22] T. K. Vrana and O. B. Fosso, “Technical aspects of the north sea super grid,” *CIGRE Electra*, November, 2011.
- [23] D. Van Hertem and M. Ghandhari, “Multi-terminal VSC HVDC for the european supergrid: Obstacles,” *Renewable and Sustainable Energy Reviews*, vol. 14, no. 9, pp. 3156–3163, Dec. 2010.
- [24] K. Rudion, A. Orths, P. Eriksen, and Z. Styczynski, “Toward a benchmark test system for the offshore grid in the north sea,” in *2010 IEEE Power and Energy Society*

- General Meeting*, Jul. 2010, pp. 1–8.
- [25] S. Henry, A. Denis, and P. Panciatici, “Feasibility study of off-shore HVDC grids,” in *2010 IEEE Power and Energy Society General Meeting*, Jul. 2010, pp. 1–5.
- [26] C. Stijn, “Steady-state and dynamic modelling of vsc hvdc systems for power system simulation,” Ph.D. dissertation, PhD dissertation, Katholieke University Leuven, Belgium, 2010.
- [27] R. Teixeira Pinto and J. A. Ferreira, “Multi-terminal DC networks: System integration, dynamics and control,” Ph.D. dissertation, CPI Koninklijke WÄhrmann, Mar. 2014.
- [28] T. M. Haileselassie, “Control, dynamics and operation of multi-terminal VSC-HVDC transmission systems,” dissertation, Norwegian University of Science and Technology, 2012.
- [29] W. Long and S. Nilsson, “HVDC transmission: yesterday and today,” *IEEE Power and Energy Magazine*, vol. 5, no. 2, pp. 22–31, Mar. 2007.
- [30] N. Flourentzou, V. Agelidis, and G. Demetriades, “VSC-Based HVDC power transmission systems: An overview,” *IEEE Transactions on Power Electronics*, vol. 24, no. 3, pp. 592–602, Mar. 2009.
- [31] S. Cole and R. Belmans, “Transmission of bulk power,” *IEEE Industrial Electronics Magazine*, vol. 3, no. 3, pp. 19–24, Sep. 2009.
- [32] P. Haugland, “It is time to connect: Technical description of hvdc light® technology,” *ABB Techincal Report*, 2008.
- [33] J. DESCLOUX, P. RAULT, S. NGUEFEU, J.-B. CURIS, X. GUILLAUD, F. COLAS, and B. RAISON, “HVDC meshed grid: Control and protection of a multi-terminal HVDC system,” in *CIGRE 2012*, France, 2012.
- [34] J. Beerten, D. Van Hertem, and R. Belmans, “VSC MTDC systems with a distributed DC voltage control - a power flow approach,” in *PowerTech, 2011 IEEE Trondheim*, Jun. 2011, pp. 1–6.
- [35] P. Kundur, N. J. Balu, and M. G. Lauby, *Power system stability and control*. McGraw-hill New York, 1994, vol. 7.
- [36] ENTSO-E, “Offshore transmission technology report - entso-e,” Tech. Rep., Nov. 2011.
- [37] A. LAbbate and G. Migliavacca, “Review of costs of transmission infrastructures, including cross border connections,” *REALISEGRID Deliverable D*, vol. 3, 2011.
- [38] G. Stamatiou, K. Srivastava, M. Reza, and P. Zanchetta, “Economics of dc wind collection grid as affected by cost of key components,” *Volume 15 Wind Energy Applications*, p. 4177, 2011.

References

- [39] S. Lundberg, "Performance comparison of wind park configurations," Chalmers University of Technology, Tech. Rep., 2003.
- [40] A. L. Abbate and G. Migliavacca, "Review of costs of transmission infrastructures, including cross border connections," *REALISEGRID Deliverable D*, vol. 3.
- [41] J.-E. Skog, K. Koreman, B. Pääjärvi, T. Worzyk, and T. Andersröd, "The norned hvdc cable link—a power transmission highway between norway and the netherlands," *Proceedings of Energex 2006*, 2006.
- [42] E. W. E. Association *et al.*, "Oceans of opportunity," *Harnessing Europes largest domestic energy resource. European Wind Energy Association*, 2009.
- [43] N. Pool, "Nord pool spot," *Nord Pool Spot*, 2012.
- [44] EUROPEAN COMMISSION, "Energy prices and costs report," Brussels, Tech. Rep. SWD(2014) 20 final/2, Mar. 2014.
- [45] ENTSO-E, "ENTSO-E overview of transmission tariffs in europe: Synthesis 2011," Tech. Rep., Jun. 2012.
- [46] J. Adams and L. Juleff, *Managerial economics for decision making*. Palgrave Macmillan, 2003.
- [47] R. Billinton, H. Chen, and R. Ghajar, "Time-series models for reliability evaluation of power systems including wind energy," *Microelectronics Reliability*, vol. 36, no. 9, pp. 1253–1261, Sep. 1996.
- [48] R. Billinton and W. Wangdee, "Reliability-based transmission reinforcement planning associated with large-scale wind farms," *IEEE Transactions on Power Systems*, vol. 22, no. 1, pp. 34–41, 2007.
- [49] P. Chen, T. Pedersen, B. Bak-Jensen, and Z. Chen, "ARIMA-Based time series model of stochastic wind power generation," *IEEE Transactions on Power Systems*, vol. 25, no. 2, pp. 667–676, 2010.
- [50] J. McLean and G. Hassan, "Wp2. 6 equivalent wind power curves," *TradeWind Deliverable*, vol. 2, pp. 1–14, 2008.
- [51] A. Shamshad, M. A. Bawadi, W. M. A. Wan Hussin, T. A. Majid, and S. A. M. Sanusi, "First and second order markov chain models for synthetic generation of wind speed time series," *Energy*, vol. 30, no. 5, pp. 693–708, Apr. 2005.
- [52] F. Castro Sayas and R. Allan, "Generation availability assessment of wind farms," *Generation, Transmission and Distribution, IEE Proceedings-*, vol. 143, no. 5, pp. 507–518, Sep. 1996.
- [53] N. B. Negra, O. Holmström, B. Bak-Jensen, and P. Sørensen, "Model of a synthetic wind speed time series generator," *Wind Energy*, vol. 11, no. 2, pp. 193–209, Mar. 2008.

- [54] B. G. Brown, R. W. Katz, and A. H. Murphy, "Time series models to simulate and forecast wind speed and wind power," *Journal of Climate and Applied Meteorology*, vol. 23, pp. 1184–1195, Aug. 1984.
- [55] W. Wangdee and R. Billinton, "Considering load-carrying capability and wind speed correlation of WECS in generation adequacy assessment," *IEEE Transactions on Energy Conversion*, vol. 21, no. 3, pp. 734–741, Sep. 2006.
- [56] S. Soman, H. Zareipour, O. Malik, and P. Mandal, "A review of wind power and wind speed forecasting methods with different time horizons," in *North American Power Symposium (NAPS), 2010*, Sep. 2010, pp. 1–8.
- [57] M. Lei, L. Shiyan, J. Chuanwen, L. Hongling, and Z. Yan, "A review on the forecasting of wind speed and generated power," *Renewable and Sustainable Energy Reviews*, vol. 13, no. 4, pp. 915–920, May 2009.
- [58] I. Colak, S. Sagiroglu, and M. Yesilbudak, "Data mining and wind power prediction: A literature review," *Renewable Energy*, vol. 46, pp. 241–247, Oct. 2012.
- [59] G. E. P. Box, G. M. Jenkins, and G. C. Reinsel, *Time Series Analysis: Forecasting and Control*. John Wiley & Sons, May 2013.
- [60] A. Chuang, "Time series analysis: Univariate and multivariate methods," *Technometrics*, vol. 33, no. 1, pp. 108–109, Feb. 1991.
- [61] T. G. Barbounis and J. B. Theocharis, "A locally recurrent fuzzy neural network with application to the wind speed prediction using spatial correlation," *Neurocomputing*, vol. 70, no. 7, pp. 1525–1542, Mar. 2007.
- [62] I. Damousis, M. Alexiadis, J. Theocharis, and P. Dokopoulos, "A fuzzy model for wind speed prediction and power generation in wind parks using spatial correlation," *IEEE Transactions on Energy Conversion*, vol. 19, no. 2, pp. 352–361, Jun. 2004.
- [63] J. Torres, A. Garc a, M. De Blas, and A. De Francisco, "Forecast of hourly average wind speed with ARMA models in navarre (Spain)," *Solar Energy*, vol. 79, no. 1, pp. 65–77, Jul. 2005.
- [64] I. Van der Hoven, "POWER SPECTRUM OF HORIZONTAL WIND SPEED IN THE FREQUENCY RANGE FROM 0.0007 TO 900 CYCLES PER HOUR," *Journal of Meteorology*, vol. 14, no. 2, pp. 160–164, Apr. 1957.
- [65] NASA, "NASA (National aeronautics and space administration)," <http://disc.sci.gsfc.nasa.gov/daac-bin/FTPSubset.pl>, 2014.
- [66] D. Hur, "Economic considerations underlying the adoption of hvdc and hvac for the connection of an offshore wind farm in korea," *J. Electr. Eng. Technol*, vol. 7, no. 2, pp. 157–162, 2012.

Appendix

Appendix

Appendix A

DC power flow equation

A power flow model of an HVDC grid can be developed by using the same procedure as that for AC [35], [26]. In a study presented in [27], a DC power flow equation is developed but the procedure followed was less clear compare with the conventional procedures. In this section a step by step generic AC power flow equation is derived from which a DC power flow equation can be determined.

Consider Figure A.1 which shows a single line diagram of a power system. The buses in the system are numbered from 1 to 4, where each bus is connected to shunt element(s) and to one or more buses with transmission line(s). All branches are denoted with their admittance values $y_{i,j}$ for a branch connecting bus i to bus j and y_i for a shunt element at bus i . Current injection at a bus i is denoted by I_i . A current injection can be either positive (into the bus) or negative (out of the bus).

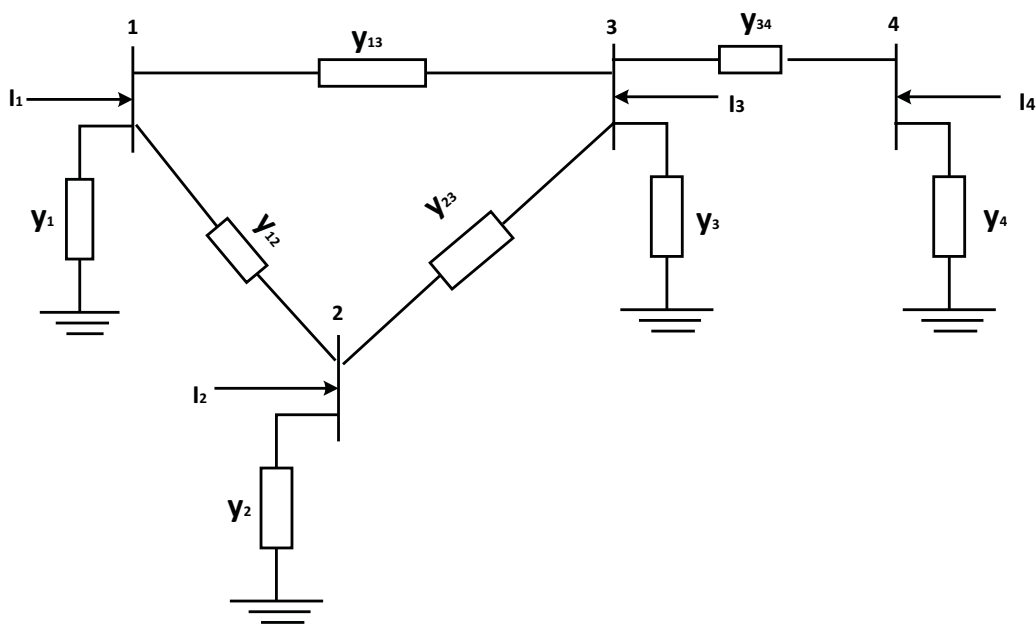


Figure A.1: Typical power system topology

Appendix A. DC power flow equation

Kirchoff's Current Law (KCL) states that current injection at a bus is equal to the sum of the currents flowing out of the bus. Combining this with Ohms law ($I = U/z = Vy$), the current injected into bus 1 can be written as

$$I_1 = (U_1 - U_2)y_{12} + (U_1 - U_3)y_{13} + (U_1 - U_4)y_{14} + U_1y_1 \quad (\text{A.1})$$

Note that the current contribution of the term containing y_{14} is zero since y_{14} is zero (no connection between bus 1 and 4). Re-arranging (A.1), the current injected at bus 1 can be expressed as

$$I_1 = U_1(y_1 + y_{12} + y_{13} + y_{14}) + U_2(-y_{12}) + U_3(-y_{13}) + U_4(-y_{14}) \quad (\text{A.2})$$

The current injections at bus 2, 3 and 4 can be represented in a similar way. The equation containing all the nodal quantities is expressed as

$$\begin{bmatrix} I_1 \\ I_2 \\ I_3 \\ I_4 \\ \dots \\ U_1 \\ U_2 \\ U_3 \\ U_4 \end{bmatrix} = \begin{bmatrix} y_1 + y_{12} + y_{13} + y_{14} & -y_{12} & -y_{13} & -y_{14} & \dots \\ -y_{21} & y_2 + y_{21} + y_{23} + y_{24} & -y_{23} & -y_{24} & \dots \\ -y_{31} & -y_{32} & y_3 + y_{31} + y_{32} + y_{34} & -y_{34} & \dots \\ -y_{41} & -y_{42} & -y_{43} & y_4 + y_{41} + y_{42} + y_{43} & \dots \end{bmatrix} \dots \quad (\text{A.3})$$

Note that the admittance from bus i to bus j is the same as the admittance from bus j to bus i . The matrix containing the network admittances in (A.3) is called the admittance matrix, also known as the Y-bus matrix, and is denoted as

$$[Y] = \begin{bmatrix} Y_{11} & Y_{12} & Y_{13} & Y_{14} \\ Y_{21} & Y_{22} & Y_{23} & Y_{24} \\ Y_{31} & Y_{32} & Y_{33} & Y_{34} \\ Y_{41} & Y_{42} & Y_{43} & Y_{44} \end{bmatrix} \quad (\text{A.4})$$

where Y_{ij} is an element of the admittance matrix in row i and column j , as can be seen in (A.3).

Combining (A.3) and (A.4), (A.3) can be re-written as

$$\begin{bmatrix} I_1 \\ I_2 \\ I_3 \\ I_4 \end{bmatrix} = \begin{bmatrix} Y_{11} & Y_{12} & Y_{13} & Y_{14} \\ Y_{21} & Y_{22} & Y_{23} & Y_{24} \\ Y_{31} & Y_{32} & Y_{33} & Y_{34} \\ Y_{41} & Y_{42} & Y_{43} & Y_{44} \end{bmatrix} \begin{bmatrix} U_1 \\ U_2 \\ U_3 \\ U_4 \end{bmatrix} \quad (\text{A.5})$$

Equation (A.5) can be applied to a system with any number of buses. The general relationship between the nodal quantities (voltage and current in this case) for any system with 'n' number of buses can be written as

$$\begin{bmatrix} I_1 \\ I_2 \\ \vdots \\ \vdots \\ I_n \end{bmatrix} = \begin{bmatrix} Y_{11} & Y_{12} & \cdot & \cdot & \cdot & Y_{1n} \\ Y_{21} & Y_{22} & \cdot & \cdot & \cdot & Y_{2n} \\ \cdot & \cdot & \cdot & \cdot & \cdot & \cdot \\ \cdot & \cdot & \cdot & \cdot & \cdot & \cdot \\ Y_{n1} & Y_{n2} & \cdot & \cdot & \cdot & Y_{nn} \end{bmatrix} \begin{bmatrix} U_1 \\ U_2 \\ \cdot \\ \cdot \\ U_n \end{bmatrix} \Rightarrow [I] = [Y][U] \quad (\text{A.6})$$

An important property of the admittance matrix is that it is symmetrical along the diagonal elements (i.e.; $Y_{ij}=Y_{ji}$); the diagonal element Y_{ii} is obtained as the sum of the admittances of all the branches connected to bus i , including the shunt element (i.e.; $Y_{ii} = y_i + \sum_{k=1, k \neq i}^N y_{ik}$); the off-diagonal elements are the negative sum of the admittances connecting bus i and j (i.e.; $Y_{ij} = -y_{ij}$).

In power flow problems, usually the power injected at the buses are given instead of the injected current. Hence, the fundamental apparent power (S_k) injected at bus k can be expressed as

$$S_k = P_k + jQ_k = U_k I_k^* \quad (\text{A.7})$$

where U_k and I_k are the nodal voltage and current at bus k respectively, S_k is the apparent power and P_k, Q_k active and fundamental reactive power respectively.

From (A.6), the current injected at bus k can be calculated as

$$I_k = \sum_{j=1}^N Y_{kj} V_j \quad (\text{A.8})$$

where N is the total number of buses in the system.

Combining (A.7) and (A.8), the power injected at a bus k can be calculated as

$$S_k = U_k \left(\sum_{j=1}^N Y_{kj} U_j \right)^* = U_k \sum_{j=1}^N Y_{kj}^* U_j^* \quad (\text{A.9})$$

where S_k, P_k, Q_k are the fundamental apparent, active and fundamental reactive power injected at bus k ; U_k is the voltage at bus k and Y_{kj} is the admittance of the line from bus k to bus j .

Observe that in the DC side of the system, the voltage at a bus U_k is a DC quantity, hence $U_k = |U_k| \angle 0 = |U_k|$. The admittance Y_{kj} is generally a complex quantity, and is defined in terms of the conductance G_{kj} and susceptance B_{kj} as a real and imaginary parts of the admittance matrix element Y_{kj} , respectively, so that $Y_{kj} = G_{kj} + jB_{kj}$. However, in a steady state DC system, the impact of on the susceptance B_{kj} can be neglected and hence the fundamental reactive power is zero. Hence, a model of DC power flow equation consists of only active power which can be formulated as

Appendix A. DC power flow equation

$$P_k = \sum_{j=1}^N |U_k| |U_j| G_{kj} \quad (\text{A.10})$$

Appendix B

Newton-Raphson method

Consider a function $f(U) = P$, where U is the unknown variable and let $U^{[0]}$ be the initial estimate of the roots of the function $f(U)$ and $\Delta U^{[0]}$ be a small deviation from the actual solution. The function $f(U)$ around the estimated root can be written as $f(U^{[0]} + \Delta U^{[0]}) = P$. This function can be expressed using the Taylor-series expansion as

$$f(U^{[0]} + \Delta U^{[0]}) = f(U^{[0]}) + \left(\frac{df}{dU}\right) \Delta U^{[0]} + \frac{1}{2!} \left(\frac{d^2 f}{dU^2}\right) (\Delta U^{[0]})^2 \dots = P \quad (\text{B.1})$$

For a small value of the deviation in the root, $\Delta U^{[0]}$, (B.1) can be approximated as

$$\begin{aligned} f(U^{[0]} + \Delta U^{[0]}) &\approx f(U^{[0]}) + \left(\frac{df}{dU}\right) \Delta U^{[0]} = P \\ \Rightarrow P - f(U^{[0]}) &= \Delta P^{[0]} = \left(\frac{df}{dU}\right) \Delta U^{[0]} \end{aligned} \quad (\text{B.2})$$

The deviation $\Delta U^{[0]}$ can be calculated from (B.2) and it is used to update the new approximation of the solution as

$$U^{[1]} = U^{[0]} + \Delta U^{[0]} \quad (\text{B.3})$$

The second and third approximation can be iterated and calculated in a similar way. Hence, (B.3) can be generalized to calculate the n^{th} approximation of the variable as

$$U^{[n+1]} = U^{[n]} + \Delta U^{[n]} \quad (\text{B.4})$$

This iteration continues until convergence condition is met, namely $\Delta U^{[n]} < \varepsilon$, where ε is the error in the solution which can be tolerated.

Appendix B. Newton-Raphson method

Equation (B.4) is used to solve a non-linear equation with one variable. A similar procedure can be used to solve non-linear equations involving a number of variables. The deviation of the variables in the system of non-linear equations involving N variables is calculated as

$$\begin{bmatrix} \Delta U_1 \\ \Delta U_2 \\ \cdot \\ \cdot \\ \cdot \\ \Delta U_N \end{bmatrix}^{[n]} = \begin{bmatrix} \frac{\partial f_1}{\partial U_1} & \frac{\partial f_1}{\partial U_2} & \cdot & \cdot & \cdot & \frac{\partial f_1}{\partial U_N} \\ \frac{\partial f_2}{\partial U_1} & \frac{\partial f_2}{\partial U_2} & \cdot & \cdot & \cdot & \frac{\partial f_2}{\partial U_N} \\ \cdot & \cdot & \cdot & \cdot & \cdot & \cdot \\ \cdot & \cdot & \cdot & \cdot & \cdot & \cdot \\ \cdot & \cdot & \cdot & \cdot & \cdot & \cdot \\ \frac{\partial f_N}{\partial U_1} & \frac{\partial f_N}{\partial U_2} & \cdot & \cdot & \cdot & \frac{\partial f_N}{\partial U_N} \end{bmatrix}^{-1} \begin{bmatrix} \Delta P_1 \\ \Delta P_2 \\ \cdot \\ \cdot \\ \cdot \\ \Delta P_N \end{bmatrix}^{[n]} \Rightarrow [\Delta U]^{[n]} = [J]^{-1} [\Delta P]^{[n]} \quad (\text{B.5})$$

where $\Delta U^{[n]}$ is the deviation in the solution of the variable U at the n^{th} iteration, J is the Jacobian matrix which is a function of the partial derivatives of the function f and $\Delta P^{[n]}$ which is defined as

$$[\Delta P]^{[n]} = [P]^{[n]} - [f(U^{[n]})] \quad (\text{B.6})$$

Using the deviation in the variable, $\Delta U^{[n]}$, the solution of the variable U can be updated using the relation

$$[U]^{[n+1]} = [U]^{[n]} + [\Delta U]^{[n]} \quad (\text{B.7})$$

Appendix C

Stochastic time series model

A stationary stochastic process is a process which remains at equilibrium at about constant mean level. A stationary process $Y(t_n)$ can be characterized by its mean μ and its auto-covariance coefficients, γ_k or equivalently by its mean, variance σ_y^2 and autocorrelation coefficients (ACC) ρ_k [59] - [60]. Hence, given these parameters, the process can be modelled by a class of a stochastic model called *stationary model*.

Let $y(t_1), y(t_2), \dots, y(t_N)$ be an observed time series generated from a statistical process, $Y(t_n)$, with a probability distribution of $p(Y(t_n))$. The process is said to be stationary if the probability distribution $p(Y(t_n))$ is the same at all time instants. Hence, the probability distribution of a stationary process at time t_n can be inferred or deduced by forming the histogram of the time series resulting from one realization made at different times. Similarly, the mean of the stationary process at time t_n can be estimated, according to [59] - [60], from the mean of the observed time series (one realization) as

$$\bar{y} = \frac{1}{N} \sum_{n=1}^N y(t_n) \quad (\text{C.1})$$

Similarly, the variance of the stationary process at time t_n can be estimated from the observed time series as

$$\hat{\sigma}_y^2 = \frac{1}{N} \sum_{n=1}^N (y(t_n) - \bar{y})^2 \quad (\text{C.2})$$

The stationarity assumption also implies that the joint probability distribution $p(Y(t_1), Y(t_2))$ is the same for all times t_1, t_2 , which are a constant interval apart [59] - [60]. The covariance between $Y(t_n)$ and $Y(t_{n+k})$, separated by k intervals of time is called *auto - covariance* at lag k and is defined

$$\gamma_k = \text{cov}[Y(t_n), Y(t_{n+k})] = E[(Y(t_n) - \mu)(Y(t_{n+k}) - \mu)] \quad (\text{C.3})$$

Appendix C. Stochastic time series model

Similarly, the autocorrelation coefficient (ACC) of a stationary process at lag k is calculated as

$$\rho_k = \frac{E[(Y(t_n) - \mu)(Y(t_{n+k}) - \mu)]}{\sqrt{E[(Y(t_n) - \mu)^2]E[(Y(t_{n+k}) - \mu)^2]}} = \frac{E[(Y(t_n) - \mu)(Y(t_{n+k}) - \mu)]}{\sigma_y^2} \quad (\text{C.4})$$

since, for a stationary process, the variance $\sigma_y^2 = \gamma_0$ is the same at time t_{n+k} as time t_n . Thus the ACC at lag k can be calculated as

$$\rho_k = \frac{\gamma_k}{\gamma_0} \quad (\text{C.5})$$

Equation (C.5) gives the theoretical auto-correlation values, where there is an infinite number of data from each processes at each time. However, in practice, the available data at each time is limited (often to one sample). For a stationary process, a good estimate of the ACC at lag k can obtained from the observed time series data. Hence, the estimated ACC at the k^{th} lag can be calculated as

$$\hat{\rho}_k = \frac{\hat{\gamma}_k}{\hat{\gamma}_0} \quad (\text{C.6})$$

where

$$\hat{\gamma}_k = \frac{1}{N} \sum_{n=1}^{N-k} (y(t_n) - \bar{y})(y(t_{n+k}) - \bar{y}) \quad (\text{C.7})$$

is the estimate of the auto-covariance γ_k and \bar{y} is the mean of the observed time series and $k = 0, 1, 2, \dots, K$. In practice, to obtain a useful estimate of the autocorrelation function, at least fifty observations are needed and the estimated autocorrelations $\hat{\rho}_k$ would be calculated for $k = 1, 2, \dots, K$ where K is not larger than $N/4$ [59].

The other important parameter in the analysis of a stationary process is the Partial Autocorrelation Coefficient (PACC), Φ_{kk} . The PACC describes the correlation between $y(t_n)$ and $y(t_{n+k})$ after the mutual linear dependency on the intervening variables $y(t_{n+1})$, $y(t_{n+2})$, ..., $y(t_{n+k-1})$ has been removed. Given the estimated sample ACC, $\hat{\rho}_k$, the estimated PACC of the time series data, $\hat{\Phi}_{kk}$, according to [60], can be estimated as

$$\hat{\Phi}_{k+1,k+1} = \frac{\hat{\rho}_{k+1} - \sum_{j=1}^k \hat{\Phi}_{kj} \hat{\rho}_{k+1-j}}{1 - \sum_{j=1}^k \hat{\Phi}_{kj} \hat{\rho}_j} \quad (\text{C.8})$$

and

$$\hat{\Phi}_{k+1,j} = \hat{\Phi}_{kj} - \hat{\Phi}_{k+1,j+1} \hat{\Phi}_{k,k+1-j} \quad (\text{C.9})$$

Appendix D

The Per Unit System

In power system analysis, it is usually easier to use per unit system to normalize system variables. Compared to the use of physical units (amperes, volts, ohms, henry, etc...), the per unit system offers computational simplicity by eliminating units and expressing system quantities as a dimensionless ratios. A well chosen per unit system can minimize computational effort, simplify evaluation, and facilitate understanding of system quantities [35].

The per unit system is defined as

$$\text{quantity is per unit} = \frac{\text{actual quantity}}{\text{base value of the quantity}} \quad (\text{D.1})$$

An important aspect of the per unit system is the base value of the quantity. Some base quantities may be chosen independently, while others follow the fundamental relationship between the system variables. Normally, the base values are often chosen so that the principal variables will be equal to one per unit under rated condition. If base voltage (U_{base}) and base power (S_{base}) are chosen, the other system quantities such as base current, base impedance are determined as

$$I_{base} = \frac{S_{base}}{U_{base}} \quad (\text{D.2})$$

$$Z_{base} = \frac{U_{base}^2}{S_{base}} \quad (\text{D.3})$$

Once the base quantities are determined, the corresponding per unit quantities can be calculated using (D.1).